



The
University
Of
Sheffield.

Experimental and Numerical Study on Deformable Structural Elements: FRP- Confined Rubberised Concrete

By:

Ruizhi Zuo

A thesis submitted in partial fulfilment of the requirements for the degree of
Doctor of Philosophy

The University of Sheffield
Faculty of Engineering
Department of Civil and Structural Engineering

24/Jun/2019

Abstract

Confined rubberised concrete (CRC) was found to be capable of sustaining much larger deformations compared to conventional concrete. Therefore, CRC is believed to have the potential to be used in deformable structural components. This thesis aims to investigate and model the mechanical behaviour of CRC.

The investigation initially examines conventional concrete and develops the methodology to address this issue. The true tri-axial apparatus Mac^{2T} is used to simulate passive confinement physically and investigates the concrete loading paths. The results show that the loading path of FRP-confined conventional concrete overlaps with its failure surface. With passive confinement, conventional concrete initially exhibits perfectly plastic up to a lateral strain of 0.008. A plasticity-based material model is proposed for FRP-confined concrete, based on the experimental observations.

The failure mechanism of passively confined rubberised concrete is shown to be similar to that of conventional concrete. The loading path of passively confined rubberised concrete moves along the failure surface when subjected to compressive loads, and it softens when the lateral expansion is larger than 0.008.

With less strength and stiffness, rubberised concrete is more deformable than conventional concrete. At the same level of compressive loading, the deformation in the loading direction of FRP-confined rubberised concrete can be ten times larger than that of the conventional concrete, which could open up opportunities for creating novel structural solutions. The material model, developed and implemented in the FEA package ABAQUS, can be used for numerical analysis of such solutions.

Acknowledgements

I want to express my gratitude to my supervisor, Prof Pilakoutas. Thank you for enrolling me into this research group. When I get confused, your advice has always been helpful.

Special thanks to Mihail. It is my great honour and pleasure to work with you. I cannot complete my thesis without your help. Thanks again for developing Mac^{2T}.

Special thanks to Maurizio and Glenn. Thank you for your support in the lab.

Last but not least. I thank my parents. Your unconditional love and support spoil me.

Content

1	Introduction	1
1.1	Research objectives	4
1.2	Layout of the thesis	4
2	Background Review	6
2.1	Rubberised concrete	7
2.2	FRP lateral confinement to concrete	8
2.3	Numerical simulation on FRP-confined concrete.....	10
2.3.1	Design-oriented material model	10
2.3.2	Research-oriented material model	13
3	Multiaxial tests on conventional concrete	16
3.1	Failure mechanism of FRP-confined concrete	16
3.2	Drawbacks in the FRP-confined concrete cylinder tests.....	21
3.2.1	Imperfect boundary condition	22
3.2.2	Indirect measurement	23
3.2.3	Difficulty of investigating less lateral confinement	24
3.3	Multiaxial tests using Mac ^{2T}	24
3.3.1	Experimental set up -- Mac ^{2T}	25
3.3.2	Testing scheme.....	36
3.4	Experimental test results.....	38
3.4.1	Test results of multiaxial tests with active confinement	38
3.4.2	Test results of multiaxial tests with passive confinement.....	45
3.5	Summary.....	55
4	Modelling of conventional concrete with passive confinement	57
4.1	Plasticity-based constitutive model for passively confined concrete.....	57

4.1.1	Yield surface	58
4.1.2	Hardening rule of passively confined concrete	61
4.1.3	Plastic flow potential.....	65
4.2	Analytical simulation through MATLAB.....	71
4.2.1	Incremental form of perfectly-plastic based constitutive model	71
4.2.2	Iterative stepwise algorithm for stress-strain generation.....	76
4.2.3	Numerical simulation through the MATLAB program	80
4.3	Numerical simulation through finite element software	83
4.3.1	Algorithm in non-linear finite element analysis	83
4.3.2	Material model of passively confined concrete in FEA.....	87
4.3.3	Numerical simulation through ABAQUS	92
4.4	Summary.....	97
5	Multiaxial tests on rubberised concrete.....	98
5.1	Specimens preparation	98
5.1.1	Mix design	99
5.1.2	Recycled rubber products	100
5.1.3	Production of rubberised concrete specimen	101
5.2	Testing scheme.....	103
5.2.1	Multiaxial tests on rubberised concrete with active confinement....	104
5.2.2	Multiaxial tests on rubberised concrete with passive confinement .	104
5.3	Multiaxial testing results of rubberised concrete	105
5.3.1	Active confinement	105
5.3.2	Passive confinement	110
5.4	Summary.....	118
6	Modelling of rubberised concrete with passive confinement	120

6.1	Plasticity-based material model of passively confined rubberised concrete	120
6.1.1	Yield surface function.....	121
6.1.2	Hardening rule.....	121
6.1.3	Plastic flow rule	125
6.2	Implementation of the proposed model in ABAQUS	128
6.3	Validation of the material modelling through ABAQUS.....	131
6.4	Summary.....	134
7	Conclusions and Recommendations for future work.....	136
7.1	Main conclusion	136
7.2	Recommendations for the future work	138
	Reference	139

List of Figures

Figure 1.1 Stress-Strain relationship of rubberised concrete varying with the rubber content (Raffoul, 2014)	2
Figure 1.2 Experimental test results of RC with three layers of CFRP confinement (Garcia, 2014)	3
Figure 2.1 Stress equilibrium in FRP confinement	11
Figure 2.2 Material model for FRP confined concrete (Papastergiou, 2010)	13
Figure 3.1 Additional confinement applied to the specimen (Papastergiou, 2010)..	17
Figure 3.2 Stress-Strain relationship of a typical cylinder specimen	18
Figure 3.3 Stress equilibrium in FRP confinement	19
Figure 3.4 Stress path of concrete cylinder with FRP confinement under uniaxial load.....	20
Figure 3.5 Axial stress and confining pressure applied to the concrete cylinder in the test by Papastergiou (2010)	21
Figure 3.6 Specimen preparation of experimental tests (Papastergiou, 2010).....	22
Figure 3.7 Layout of lateral strain gauges	23
Figure 3.8 Design of Mac ^{2t} (Petkovski et al., 2006).....	26
Figure 3.9 The stress state and crack formation of concrete cylinders.....	27
Figure 3.10 Dependence of concrete strength on different loading application systems (Gerstle et al, 1980).....	28
Figure 3.11 Schematic diagram of laser interferometer system	31
Figure 3.12 Loading path of multiaxial test with active confinement	32
Figure 3.13 Constrains in the lateral direction.....	33
Figure 3.14 Flow chart of the control loop	35
Figure 3.15 Stress-strain relation of concrete with active confinement	39
Figure 3.16 The trend line of test results in p-q coordinate	41
Figure 3.17 Tangent modulus history	43
Figure 3.18 Poisson's ratio history	44
Figure 3.19 Evaluation of the control program for passive confinement.....	46
Figure 3.20 Stress-strain relations of the specimens with passive confinement	49
Figure 3.21 Loading path of the specimens with passive confinement	50

Figure 3.22 Trend lines of the stress state at same level of lateral strain	51
Figure 3.23 Effect of confining stiffness on dilation parameter v history	54
Figure 3.24 A typical tested specimen with passive confinement.....	55
Figure 4.1 The compressive and the tensile meridian of the yield surface	60
Figure 4.2 Loading path of a passively confined concrete under load	61
Figure 4.3 Relation between hardening parameter σ_c and hardening variable ε_{cpl}	63
Figure 4.4 Trend lines of the stress state at the same level of lateral strain.....	64
Figure 4.5 Relation between the parameter d and the hardening variable ε_l	65
Figure 4.6 The curve of function $\varphi (-d\varepsilon_{2p}/d\varepsilon_{1p})$	67
Figure 4.7 The history of plastic strain increment ratio $(-d\varepsilon_{2p}/d\varepsilon_{1p})$ of P1.....	69
Figure 4.8 History of dilation angle of multiaxial tests	70
Figure 4.9 Initial dilation angle φ_1 at different levels of confining stiffness	70
Figure 4.10 Flow chart of the verification program	79
Figure 4.11 Numerical simulation results of the experimental test P1	81
Figure 4.12 Comparison between the numerical and the experimental test results	82
Figure 4.13 Linear interpolation between data points for hardening rule.....	91
Figure 4.14 Diagram of spring defined in ABAQUS.....	93
Figure 4.15 Loading path of concrete in the experimental and the numerical test..	94
Figure 4.16 Comparison between the defined yielding surface and data points from experimental test P1	95
Figure 4.17 Stress-strain curves from the numerical and the experimental tests	96
Figure 5.1 Grading curves of the fine and the coarse rubber particles	101
Figure 5.2 Profile of the mould with rubberised concrete and cement mortar top	103
Figure 5.3 Rubberised concrete specimen with top surface polished.....	103
Figure 5.4 Stress-strain of rubberised concrete with constant confining pressure	106
Figure 5.5 Trend line of test results in p-q coordinate	108
Figure 5.6 Tangent module history of rubberised concrete with constant confinement.....	109
Figure 5.7 History of dilation parameter v_t	110
Figure 5.8 Evaluation of the control program for passive confinement.....	111
Figure 5.9 Stress-strain of rubberised concrete with passive confinement	113
Figure 5.10 Loading path of rubberised concrete with passive confinement	114

Figure 5.11 Loading path of rubberised concrete with passive confinement	116
Figure 6.1 Typical loading path of passively confined concrete	122
Figure 6.2 The relation between σ_c and ε_{cpl}	123
Figure 6.3 The relation between σ_c and ε_l	123
Figure 6.4 Relation between ε_{cpl} and σ_c from experimental tests.....	125
Figure 6.5 Relation between ε_l and σ_c from experimental tests	125
Figure 6.6 The history of dilation angle φ plotted against confining pressure σ_l ..	127
Figure 6.7 Comparison between data points and function $\varphi(\sigma_l)$	130
Figure 6.8 Mesh of the rubberised concrete specimen.....	131
Figure 6.9 Loading path of RuC in the experimental and the numerical test.....	133
Figure 6.10 Stress-strain from the experimental and the numerical tests.....	134

List of Tables

Table 2.1 Comparison between original mix design & optimised mix design	8
Table 3.1 Concrete mix design	29
Table 3.2 The process of specimen preparation.....	29
Table 3.3 Confining pressure at the end of step 2.....	37
Table 3.4 Confining stiffness for multiaxial tests with passive confinement	37
Table 3.5 Stress state when the load reaches the peak	40
Table 3.6 The predefined and the actual confining stiffness.....	47
Table 4.1 Input parameters for the MATLAB program	80
Table 4.2 Material-properties-dependent field variables.....	89
Table 4.3 Parameters for the shape of the yield surface.....	90
Table 4.4 Data points imported into ABAQUS for hardening rule.....	90
Table 4.5 Data points imported into ABAQUS for plastic flow rule.....	92
Table 4.6 Spring property in ABAQUS model.....	93
Table 5.1 Optimised concrete mix	99
Table 5.2 Relative proportion of rubber particles for fine aggregates replacement	100
Table 5.3 Relative portion of rubber particles for fine aggregates replacement	101
Table 5.4 Constant confining pressure	104
Table 5.5 Confining stiffness	105
Table 5.6 Stress state of rubberised concrete at peak compressive load	107
Table 5.7 The specified and the actual confining stiffness	112
Table 5.8 Density of rubberised concrete specimen	115
Table 6.1 Material-properties-dependent field variables.....	128
Table 6.2 Parameters for the shape of the yield surface.....	129
Table 6.3 Data points imported into ABAQUS for hardening rule identification	129
Table 6.4 Confining stiffness defined in numerical model	132

List of Symbols

σ_{oct}	Octahedral normal stress
ε_{oct}	Octahedral normal strain
τ_{oct}	Octahedral shear stress
γ_{oct}	Octahedral shear strain
K_t	Tangent bulk module
G_t	Tangent shear module
σ_1	First principal stress
σ_2	Second principal stress
σ_3	Third principal stress
ε_1	First principal strain
ε_2	Second principal strain
ε_3	Third principal strain
ε_v	Volumetric strain
E_{FRP}	Young's modulus of FRP
ε_{FRP}	Strain of FRP in the hoop direction
f_c	Concrete compressive strength
σ_l	Confining pressure of FRP to concrete
k_l	Confining stiffness of FRP to concrete
ε_l	Concrete lateral expansion
p	Equivalent pressure stress
q	Mises equivalent stress
E_t	Tangent modulus
E	Young's modulus of concrete
ν	Poisson's ratio of concrete

1 Introduction

Reinforced concrete (RC) bridges are important components of the road infrastructure. Many of these bridges deteriorate over time due to traffic load, natural movement because of temperature and environmental attack. In particular, the deterioration of movement joints and associated bearing elements might lead to damage and even structural failures. To prevent failures, such elements require inspection and structural rehabilitation. Moreover, bearings (usually made of steel and/or neoprene) need to be replaced at regular intervals (Zhao and Tonia, 2012). These activities not only require significant investment from highway authorities, but can also lead to long traffic interruptions and discomfort for road users. In recent years, the construction of integral/semi-integral bridges without joints and bearings is used to minimise maintenance costs and enhance long-term durability of bridges (Burke, 2009). However, large secondary forces induced by creep, shrinkage and thermal movement affect the behaviour of integral/semi-integral bridges, and these need to be considered in the analysis and design of these structures. Hence, there is a need for a flexible and deformable bearing material that does not require regular replacement and can accommodate structural movement.

The concrete research group at the University of Sheffield recently completed the EU funded project Anagennisi, which focused on the innovative reuse of the tyre components in concrete. Rubberised concrete, made up with one of the reused tyre components, rubber, was found to be capable of sustaining large axial and lateral deformations. A pilot study has shown that confined rubberised concrete (CRC) can enable much larger axial deformations compared to conventional concrete (up to 20 times more); therefore, CRC structural components are believed to have the potential to be used as bearing elements in the substructures of bridges or produce integral bridges, and reduce lateral stiffness. Hence, the large restraining forces induced by deck movement can be reduced. To enable the engineering use of CRC components, it is essential to not only understand the material properties of this novel material, but also to develop material models which can facilitate structural analysis and design.

The concrete research group in the University of Sheffield studied the material properties of rubberised concrete (RuC) (Garcia, 2014; Raffoul, 2014; Raffoul et al., 2016; Raffoul et al., 2017). Previous research mainly addressed the fresh properties of RuC (Raffoul, 2014; Raffoul et al., 2016). Due to the difference in the frictional properties of rubber and conventional aggregates, the fresh properties of concrete change. Specifically, in direct replacement of aggregates both slump reduction and the segregation is observed. However, it is found that the optimal mix with acceptable fresh properties can be achieved by partly replacing cement with PFA and SF while maintaining the water-cement ratio, and by using superplasticizer (Raffoul, 2014).

Since the problem regarding the fresh properties of rubberised concrete has been addressed, the challenge left is the identification and modelling of the hardened properties. The loss of axial strength with increasing rubber content is well known. Figure 1.1 shows uniaxial tests on rubberised concrete cylinders with increasing rubber content. As illustrated, both the ultimate strength and corresponding strain decrease with increasing rubber content, while the lateral strain at peak load increases. Despite the axial capacity reduction, rubberised concrete is more deformable than conventional concrete, and it has a promising lateral expansion capacity.

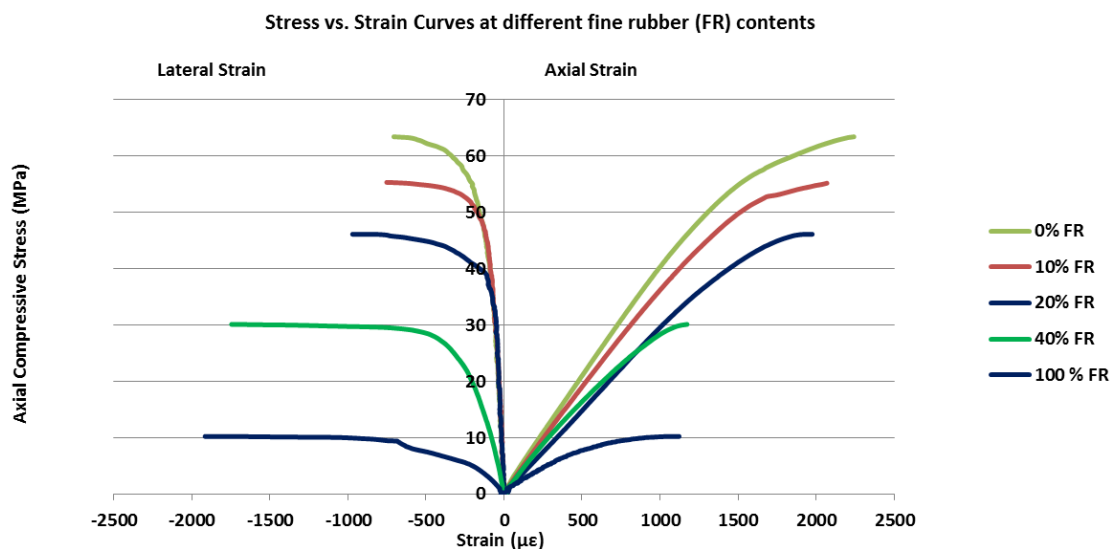


Figure 1.1 Stress-Strain relationship of rubberised concrete varying with the rubber content (Raffoul, 2014)

According to the fracture process observed in the multiaxial tests of conventional concrete, unstable propagation of cracking is immediately followed by concrete crushing (Kotsovos & Newman, 1977). The cracks, due to tensile strains, are oriented in the direction of the principal compressive stress, i.e. vertically for cylinder specimens under uniaxial load. As a result, the strengthening of the concrete can be achieved by lateral confinement, since the unstable crack development can be arrested. FRP lateral confinement has been widely used for this purpose. With adequate FRP lateral confinement, the compressive failure of concrete can be prevented.

It has been shown that the strength loss of rubberised concrete can be recovered by lateral confinement (Garcia, 2014). As is illustrated in Figure 1.2, a rubberised concrete cylinder with 40% rubber content exhibited an ultimate axial strain more than 2%. With higher rubber contents and appropriate FRP confinement, the composite is believed to sustain even higher deformations, and possibly up to 10%.

Even through the behaviour of heavily confined conventional concrete has been examined experimentally (through active and passive confinement), the behaviour of rubberised concrete under active and passive confinement is not known.

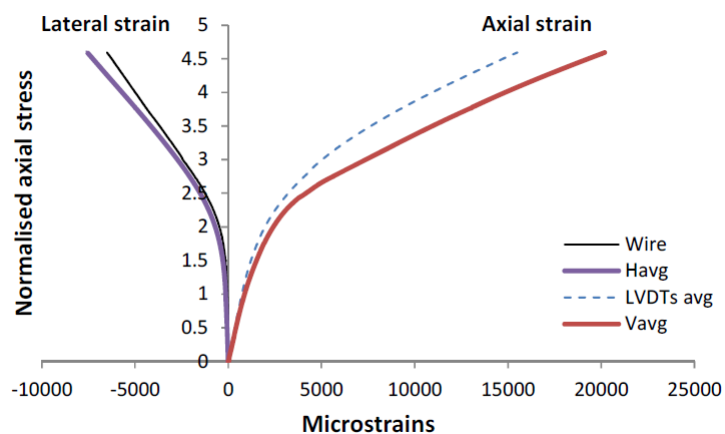


Figure 1.2 Experimental test results of RC with three layers of CFRP confinement (Garcia, 2014)

This research aims to investigate the mechanical behaviour of rubberised concrete under lateral confinement. Although extensive research has been conducted on the

mechanical behaviour of concrete with FRP lateral confinement in the last 30 years, the nature of failure mechanism is still not well known.

This thesis begin with an investigation on conventional concrete, since research on conventional concrete is abundant and comparison can be made. A hypothesis regarding the failure mechanism of FRP-confined conventional concrete is proposed, according to analysis on previous experimental tests. In order to verify the proposed hypothesis and provide firm evidence, multiaxial tests using apparatus Mac^{2T} (Petkovski et al., 2006) are designed.

Following the experiments, a material model for FRP-confined concrete is proposed to represent the failure mechanism. The proposed material model can be used for both design-oriented and research-oriented analysis.

1.1 Research objectives

The research aim, investigation of mechanical behaviour of CRC, is achieved by the following objectives:

- Analyse previous tests that investigate concrete multiaxial behaviour
- Propose a hypothesis regarding the failure mechanism of FRP-confined concrete
- Design and execute multi-axial tests on concrete specimen to confirm the hypothesis
- Model the mechanical behaviour of FRP-confined concrete based on its failure mechanism
- Adopt an appropriate approach for rubberised concrete and develop a material model.

1.2 Layout of the thesis

Chapter 2 provides the background review that supports the range of the work required for this thesis. The chapter begins by describing the adverse effects of rubber contents on the fresh and the hardened properties of concrete. The chapter goes on to review previous research on passive confinement for concrete, which confirms FRP confinement is capable of strengthening concrete components. Finally,

extensive research on numerical modelling of passively confined concrete is reviewed.

In Chapter 3, results of experimental tests on FRP-confined concrete cylinders, in terms of loading path in the stress space, are compared and presented against concrete failure surface. It is observed that in the stress space passively confined concrete under compressive load moves along the failure surface; therefore, a hypothesis can be proposed that concrete confined by FRP behaves as a perfect plastic material when subjected to compressive loads.

In order to verify the hypothesis and provide firm evidence, the Mac^{2t} testing facility originally designed for true tri-axial tests is used. Mac^{2t} is used to physically simulate passive confinement so as to determine the loading path of passively confined concrete. It is worth emphasising that the compressive pressure in the lateral directions, which represents the confining pressure, is not predefined. Instead, its value is dramatically updated according to concrete lateral expansion, such that the scenario of passive confinement is realised. The loading path is compared to the failure surface of concrete, which is determined by Mac^{2T} either. The hypothesis would be confirmed if the loading path overlaps with the failure surface.

According to the results from multiaxial tests, the behaviour of passively confined concrete is modelled using the framework of plasticity theory in Chapter 4. For a design-oriented analysis of passively confined concrete, a stress-strain curve is of interest. Therefore, the proposed material model is simplified and expressed in the incremental form. Consequently, the stress-strain curve of passively confined concrete under compressive load can be generated through a MATLAB program. Alternatively, the proposed material model can be introduced into nonlinear finite element software, such as ABAQUS, so as to analyse passively confined concrete structural components with complicated boundary conditions.

The approach in Chapter 3 and Chapter 4 constitute the methodology for the experimental and numerical study on CRC. Chapter 5 focuses on multiaxial tests of rubberised concrete, the results of which are used for modelling the mechanical behaviour of CRC in Chapter 6.

2 Background Review

In the developed world, one tyre is discarded per person per year, and the developing economy (e.g. China) is catching up very quickly in terms of both consumption and disposal. End of life tyres are mainly disposed by incineration (20%), mechanical shredding (30%) and landfill. Under high temperature and low humidity, landfilled tyres are prone to catching fire.

To address the environmental problems of dealing with the end of life tyres, it is proposed to reuse rubber in concrete. End of life tyres become small pieces in a process of cutting and shredding. After the steel and fabric components being separated, rubber crumb/chips with the size range from 25mm to 460mm can be obtained (Presti, 2013). By partly replacing the aggregates of conventional concrete, a novel construction material rubberised concrete is derived. However, rubber contents have adverse effects on the fresh and the hardened properties of concrete. The impaired fresh property of rubberised concrete and corresponding solution is reviewed firstly.

With increasing rubber content, rubberised concrete exhibits decrease in the ultimate strength and corresponding strain decrease. Meanwhile, the lateral strain at peak load increases. Despite the axial capacity reduction, rubberised concrete is more deformable than conventional concrete, and it has a promising lateral expansion capacity (Garcia, 2014).

The use of FRP confinement in the lateral direction has been shown to mitigate the strength loss and successfully exploit the enhanced deformability of rubberised concrete (Garcia, 2014). A preliminary study has shown that confined rubberised concrete (CRC) could enable much larger deformations compared to conventional concrete (up to 20 times more), which could lead to novel structural uses, for example in bridge bearings, base isolation and plastic hinges (Garcia, 2014). To enable this, it is essential to not only understand the properties of this new material but also develop a reliable constitutive model that facilitates numerical analysis.

2.1 Rubberised concrete

Although rubberised concrete has promising environmental benefits, the additional rubber has adverse effects on both the fresh and the hardened properties of concrete. Rubberised concrete might exhibit poor workability and lower strength (Raffoul, 2014; Raffoul et al., 2016). Therefore, the author's research group conduct a group of experimental tests, which aims to adjust concrete mix design and improve the fresh and hardened property of rubberised concrete.

Extensive research has confirmed the adverse effect of rubber content on the workability of rubberised concrete (Toutanji, 1996; Oikonomou and Mavridou, 2009). To the extreme, the fresh rubberised concrete could exhibit no slump when rubber particles replace more than 50% of the aggregates by volume (Khatib and Bayomy, 1999).

According to the observation that the entrapped air rises with the enhanced rubber content, the decrease in workability of rubberised concrete is believed to be attributed to the increasing air content in the fresh mix (Reda et al., 2008). The air content could be controlled by adding admixtures, e.g. plasticiser and superplasticiser, but a high content of such admixture could result in bleeding and segregation.

Bleeding and segregation of rubberised concrete, however, can be mitigated by the addition of silica fume (SF) and Portland fly ash (PFA). Their extra-fine particles results in a relatively dense packing and aid workability. (Wong & Kwan, 2008)

Raffoul et al. (2016) conducted a parametric study on the mix design of rubberised concrete, and examined the influence of water-cement ratio, admixture content and cement replacement material. The original concrete mix commonly used for the bridge construction is listed in Table 2.1 as a benchmark. The optimal mix was finally achieved by partly replacing 10% cement with PFA and SF while maintaining the water-cement ratio and the admixture content. The optimised mix exhibited similar slump and workability as the benchmark mix.

Table 2.1 Comparison between original mix design & optimised mix design

Material	Original mix	Optimised mix
CEM II – 52.5 MPa	425 kg/m ³	340 kg/m ³
Silica Fume (SF)		42.5 kg/m ³
Pulverised Fuel Ash (PFA)		42.5 kg/m ³
Aggregates 0/5mm	820 kg/m ³	820 kg/m ³
Aggregates 5/10mm	364 kg/m ³	364 kg/m ³
Aggregates 10/20mm	637 kg/m ³	637 kg/m ³
Water	180 l/m ³	149 l/m ³
Plasticiser (Sika Viscoflow 1000)	2.5 l/m ³	2.5 l/m ³
Superplasticiser (Sika Viscoflow 2000)	5.1 l/m ³	5.1 l/m ³

Bompa et al. (2017) investigated the mechanical behaviour of rubberised concrete, the specimens of which are prepared according to the optimal mixed design proposed by Raffoul et al. (2016). The effect of rubber content on the uniaxial behaviour of rubberised concrete is under investigation. With the increase of rubber content, both the peak compressive stress and the elastic module were found to decrease.

In order to enhance the performance of rubberised concrete and exploit its deformable potential, FRP confinement can be a promising solution.

2.2 FRP lateral confinement to concrete

Extensive research has shown that Fibre Reinforced Polymers (FRP) can be used to confine concrete and effectively increase its axial capacity. As one type of passive confinement, FRP is activated by the concrete expansion, and in turn, FRP applies lateral confining pressure to concrete, which enhances both strength and ductility.

Mirmiran and Shahawy (1997) performed tests on concrete cylinders cast into Glass FRP tubes. The specimen under increasing compressive load would not fail until the

rupture of the FRP confinement. The FRP-confined concrete specimens exhibited a significant increase in both strength and ductility when compared to those without FRP confinement.

Teng & Lam (2004) conducted similar tests on concrete cylinders (100mm diameter and 200mm height) wrapped by Carbon FRP (CFRP) sheets. With three layers of CFRP, the peak axial stress that concrete could sustain increased more than 2.5 times and the ultimate axial strain was greater than 2%.

Extensive research has been conducted on small-scale specimens, with different levels of concrete strength and different FRP lateral confining stiffness, and the results were used to calibrate material models (Spoelstra and Monti, 1999; Rousakis and Tepfers, 2001; Berthet et al., 2005; Li, 2006).

In addition to small-scale tests on concrete cylinders, many researchers examined the behaviour of relatively large-scale specimens in order to confirm the effectiveness of FRP confinement in strengthening the reinforced concrete structures. Garcia et al. (2010) investigated the behaviour of a one-bay two-storey frame, designed according to old standards, through shaking table tests. The original frame was designed to fail in the weak beam-column joints due to the poor stirrup confinement in the shear critical regions. When subjected to an earthquake with a PGA of 0.4 g, the frame under investigation exhibited a large drift ratio of 3.9%, and severe damage was observed at the joints. Subsequently, the damaged structure was strengthened with FRP sheets at the beam-column joints and critical shear regions. The strengthened frame was subjected to the same level of seismic input (PGA=0.4g) and a maximum drift ratio of only 1.3% was observed with limited or no visible damage.

The concrete research group at the University of Sheffield has shown that the strength loss of rubberised concrete can be recovered by lateral confinement (Garcia, 2014), and has carried out extensive work on confined rubberised concrete.

Raffoul et al. (2017) conducted small-scale tests on rubberised concrete cylinder specimens with 60% rubber content. With adequate lateral confinement, the

specimens exhibited the same level of compressive strength as unconfined conventional concrete, and ultimate strain up to 5%.

Elghazouli et al. (2018) carried out large-scale tests on rubberised concrete specimens, where circular cross-section rubberised concrete columns with FRP confinement were subjected to lateral cyclic displacements and predefined levels of axial loading. The specimens with 60% rubber content exhibited stable hysteretic behaviour and could sustain large lateral drift.

2.3 Numerical simulation on FRP-confined concrete

In order to analyse and design concrete structural components confined with FRP, extensive research has been conducted on modelling the mechanical behaviour of passively confined concrete. In general, the models proposed can be divided into two groups: design-oriented and analysis-oriented.

In the design-oriented models, only the stress-strain behaviour in the axial direction is of interest. Therefore, FRP-confined concrete structural elements are regarded as a composite.

In the research-oriented models, concrete and FRP are simulated separately. When subjected to a compressive load, concrete expands in the lateral direction. FRP confinement is then stretched and in turn applies confining pressure to concrete. In order to correctly simulate such interaction, the volumetric behaviour of concrete needs to be taken into account. Due to the complicated material model and boundary conditions, the numerical models need to be implemented in a finite element framework.

2.3.1 Design-oriented material model

Multi-axial tests are normally designed to investigate the behaviour of concrete stressed in the principal direction. Based on observations from multi-axial tests, not only strength criteria (Kotsovos and Newman, 1977) but also several constitutive models (Gerstle, 1981; Han and Chen, 1985; Ohtani and Chen, 1987) have been proposed for numerical analysis. As Concrete confined by FRP is also subjected to

multi-axial loading conditions, the main constitutive models based on results from multi-axial tests could be adopted for FRP-confined concrete.

The constitutive model proposed by Gerstle (1981) (Equation 2.1 and 2.2) was used by Becque et al. (2003) in a numerical approach to predict the stress-strain behaviour of FRP-confined concrete cylinders.

$$d\sigma_{oct} = K_t \cdot d\varepsilon_{oct} \quad (2.1)$$

$$d\tau_{oct} = G_t \cdot d\gamma_{oct} \quad (2.2)$$

where σ_{oct} and ε_{oct} represent the octahedral normal stress and strain; τ_{oct} and γ_{oct} represent the octahedral shear stress and strain. K_t and G_t are the tangent bulk and shear module respectively, which vary with respect to the stress state.

Figure 2.1 shows the force equilibrium in the FRP confinement.

$$\sigma_2 \cdot R = \sigma_{FRP} \cdot t \quad (2.3)$$

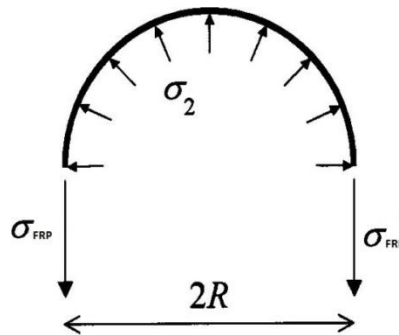


Figure 2.1 Stress equilibrium in FRP confinement

where t represents the thickness of FRP confinement. FRP material exhibits linear elastic behaviour when subjected to tensile load; therefore,

$$\sigma_2 = \frac{E_{FRP} \cdot \varepsilon_{FRP}}{R} \cdot t \quad (2.4)$$

where E_{FRP} is the Young's modulus of FRP and ε_{FRP} is the strain of FRP in the hoop direction. Due to deformation compatibility between concrete and FRP confinement, the concrete strain in the hoop direction is equal to that of the FRP. Since both the geometry and the load are axisymmetric, the shear components are

neglected and ε_{FRP} is equal to the concrete principal strains in the horizontal direction (along the radius and the hoop directions, respectively). Hence, Equation 2.4 becomes:

$$\sigma_2 = \frac{E_{FRP} \cdot \varepsilon_2}{R} \cdot t \quad (2.5)$$

Becque et al. (2003) regarded Equation 2.5 as the compliment condition. Then, the problem reduces to determining the stress-strain history of the uniaxial cylinder test, based on the following nonlinear equation system:

$$\left\{ \begin{array}{l} d\sigma_{oct} = K_t \cdot d\varepsilon_{oct} \\ \tau_{oct} = G_t \cdot d\gamma_{oct} \\ \sigma_2 = \frac{E_{FRP} \cdot \varepsilon_2}{R} \cdot t \end{array} \right. \quad (2.6)$$

Becque et al. (2003) developed an iterative procedure to solve this non-linear equation system and generate the stress-strain relation of FRP-confined concrete. Although the numerical results were shown to agree with experimental data available in the literature in terms of uniaxial stress strain, the volumetric response was not captured adequately. The inaccurate volumetric simulation may be due to the effect of load path. For instance, the concrete constitutive model proposed by Gerstle (1981) was calibrated using the experimental testing results (Gerstle et al. 1978; Gerstle et al. 1980), in which the hydrostatic load was applied first, followed by stress deviation in the deviatoric plane. In FRP confined cylinder, however, the lateral stress develops as a result of the dilation of concrete following the application of axial stress.

Imran and Pantazopoulou (1996) investigated the effect of different load paths on the mechanical behaviour of concrete cylinders under axisymmetric load. It was found that the uniaxial strength of concrete cylinder with lateral confining pressure is not affected by the load path; on the other hand, this was found not to be the case for the volumetric behaviour. Hence, a concrete model calibrated with conventional multi-axial tests can only be used to determine the strength of FRP-confined concrete, and not necessarily the corresponding volumetric behaviour.

An alternative approach, which links multi-axial tests and FRP-confined cylinder tests, is often used by many researchers (e.g. Spoelstra and Monti 1999; Binici 2005; Jiang and Teng 2007) to predict the uniaxial behaviour of FRP-confined concrete cylinder. Conventional multi-axial test results can be used to define a family of passively confined concrete models in the approach (Figure 2.2), while an empirical equation is used to predict the volumetric behaviour based on the results of FRP-confined cylinder tests. For instance, Papastergiou (2010) adopted this approach to predict the response of FRP-confined concrete cylinders under uniaxial load. Since the FRP is activated by the lateral expansion of concrete, the confining pressure applied to the concrete cylinder varies. By making use of confined concrete models for passive confinement (black curves in Figure 2.2), the stress in concrete confined by FRP can be determined stepwise. The confining pressure in every step is related to the lateral strain, determined by an empirical equation of volumetric response. The accuracy of this approach is sensitive to the model used for passively confined concrete.

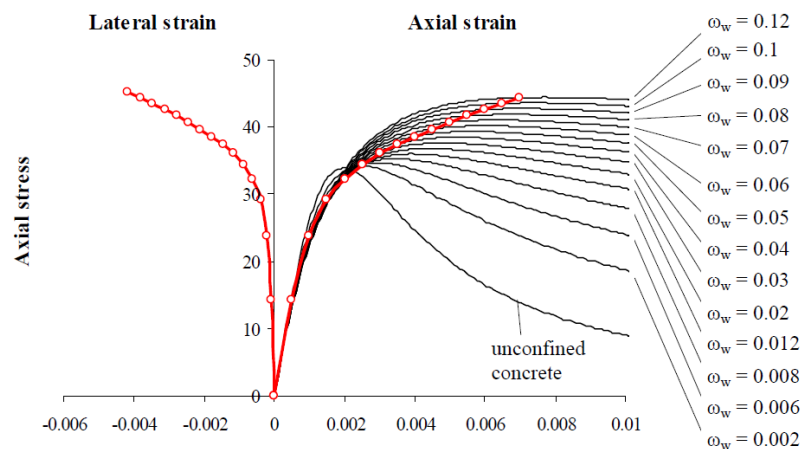


Figure 2.2 Material model for FRP confined concrete (Papastergiou, 2010)

Although the approach used by Papastergiou (2010) is capable of predicting the concrete behaviour with FRP confinement, it is not suitable for use in a finite element analysis program.

2.3.2 Research-oriented material model

Imran & Pantazopoulou (1996) investigated the triaxial behaviour of concrete by testing concrete cylinder with constant confining pressure subjected to a uniaxial

compressive load. The experimental results indicated that concrete with low confining pressure exhibits brittle failure. With confining pressures higher than 40% of the unconfined concrete strength, concrete specimen exhibited no strength reduction and behaved in a plastic manner.

When it comes to FRP-confined concrete, the confining pressure to concrete gradually increases, and eventually, the confining pressure is considerable compared to the concrete unconfined compressive strength. Therefore, it might be appropriate to simulate passively confined concrete through a plasticity-based material model. A plasticity-based material model consists of three elements: yield surface function, hardening rule and plastic potential function.

Rochette and Labossiere (1996) modelled concrete with FRP confinement as an elastic-perfectly-plastic material. The Drucker-Prager equation was used to describe the yield surface function and the plastic potential function. However, since the parameters in the yield surface function and the plastic potential function are constant and independent of lateral confinement, the material model cannot adequately represent the effect of lateral confining stiffness on the unusual concrete volumetric behaviour, either compaction or dilation.

Jiang and Wu (2011) modified the Drucker-Prager plasticity model by relating parameters to field variables. The slope of the yielding function, known as friction angle, is defined as a parametric function with respect to plastic strain in the loading direction. The parameter in the flow rule, known as dilation angle, is defined as a function with respect to plastic volumetric strain. Since there is only one hardening parameter in the hardening rule that relates the size of yield surface to concrete plastic deformation in the loading direction, the model of Jiang & Wu (2011) is only feasible for concrete subjected to compressive load and cannot be implemented for the analysis of elements subjected to more complex stress states.

Yu et al. (2010) developed a material model under the framework of Damaged Plasticity Model in ABAQUS. The yield surface consists of two hardening parameters, to facilitate the simulation concrete under both the compressive and tensile loads. Like the model proposed by Jiang and Wu (2011), Yu et al. (2010) used the Drucker-

Prager function as the flow rule. The parameter in the plastic potential function is defined as a function with respect to confining pressure and confining stiffness, in order to consider the effect of FRP confinement on volumetric behaviour.

Several other authors have implemented the use of FEA to study the confinement effect of FRP on concrete (Shahawy et al., 2000; Parvin and Wang, 2001; Doran et al., 2009; Yousf et al., 2014), generally achieving varying degree of reliability. Although all of the proposed methodologies have been shown to approximate well the experimental results, existing models are based on regression analysis of limited empirical data rather than on the representation of the actual physical phenomenon. A more robust approach that can take into account the true physical and mechanical aspect of the problem is therefore needed to assist further advancements in the field.

3 Multiaxial tests on conventional concrete

Current material models for FRP-confined concrete utilise results from passively confined cylinder tests. In addition, most are based on regression analysis and curve fitting rather than on the representation of actual physical phenomena. This chapter aims to identify the failure mechanism of FRP-confined concrete under compressive load. To achieve this, experimental tests on FRP-confined concrete cylinders by Papastergiou (2010) are reviewed, and the corresponding stress path is compared with the failure surface proposed by Chen (1994) which was calibrated on multiaxial testing results (Kupfer et al., 1969). It is observed that in the stress space, passively confined concrete under compressive load moves along the failure surface. On this basis, the following hypothesis is proposed: concrete confined by FRP should also behaves as a perfect plastic material when subjected to compressive load.

It should be noted that the proposed hypothesis is based on a comparison between two sets of experimental tests with different forms of concrete and different load path. Since concrete is a material with variability, these two sets of tests might not be directly comparable. Additionally, the experimental set-up of the tests on an FRP-confined concrete cylinder is not without deficiencies, as discussed are reviewed in the following section.

In order to verify the hypothesis and provide firmer evidence, the apparatus Mac^{2t} originally designed for true tri-axial tests is used for two groups of tests. Firstly to determine the failure surface of the concrete through the conventional multiaxial testing scheme, and secondly to physically simulate passive confinement. This latter set of tests was aimed at identifying the loading path of passively confined concrete under compressive load.

3.1 Failure mechanism of FRP-confined concrete

The tests on the FRP-confined concrete cylinders under investigation were conducted by Papastergiou (2010), results of which will be compared with conventional multiaxial tests. Concrete cylinder specimens of dimensions 100mm×200mm with a compressive strength f'_c of 42 MPa were confined by

several layers of Aramid FRP (AFRP) wrapping. Metal straps were fixed for extra confinement at the top and bottom of specimens to prevent premature failures, as illustrated in Figure 3.1. An Amsler Universal Testing machine of 2000kN capacity was used for testing the FRP-confined concrete specimen. The axial load was applied monotonically to failure. For full experimental details, refer to Papastergiou (2010).



Figure 3.1 Additional confinement applied to the specimen (Papastergiou, 2010)

The test results of a typical AFRP confined specimen in terms of stress-strain are shown in Figure 3.2. Compared with a concrete cylinder without confinement, the ultimate axial stress increased by 150% while the corresponding strain was more than 1.3%. Hence, with FRP confinement the ductility capacity of the reinforced concrete structural element was significantly enhanced. In addition to this, from the observation of the tests on FRP-confined concrete, it is clear that the failure of FRP-confined concrete cylinder is always initiated by AFRP rupture rather than concrete crushing.

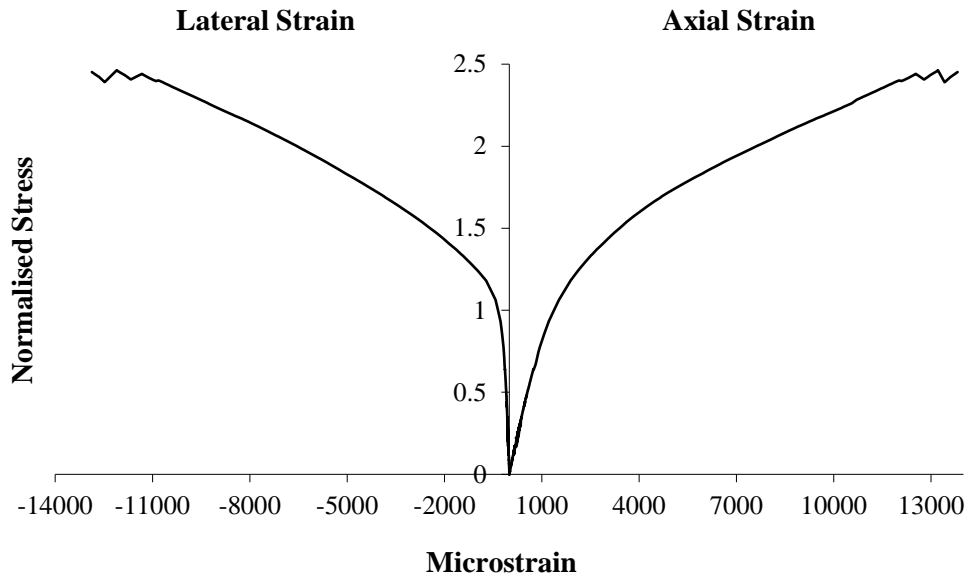


Figure 3.2 Stress-Strain relationship of a typical cylinder specimen

Multi-axial tests are normally designed to investigate the behaviour of concrete that is stressed in the principal directions. Based on such tests, strength criteria (i.e. the failure surface in the stress space) have been proposed and used to represent the performance of confined concrete. For instance, Mander (1983) predicted the maximum axial stress of stirrup confined concrete by making use of the failure surface. For concrete laterally confined, the compressive stress applied in one principal direction has been found to be larger than the stress applied in the other two (i.e. $\sigma_1 > \sigma_2 = \sigma_3$). As a result, the compressive meridian on the failure surface is of interest for the cylinder specimen with lateral confinement.

Previous research on concrete strength indicates that the compressive meridian can be expressed by a parabolic equation (Chen 1994), the coefficients of which can be determined based on multi-axial tests (Kupfer et al., 1969):

$$\frac{\sigma_{oct}}{f_c} = b_0 + b_1 \frac{\tau_{oct}}{f_c} + b_2 \left(\frac{\tau_{oct}}{f_c}\right)^2$$

where

σ_{oct} , Octahedral normal stress: $I_1/3$

τ_{oct} , Octahedral shear stress: $\sqrt{\frac{2}{3}J_2}$

FRP-confined concrete cylinders under uniaxial load are also subjected to multi-axial loading condition. In the cylinder tests, the axial stress in the concrete cylinder is provided by the Universal Testing machine, while the lateral confining pressure is applied to the concrete cylinder by the FRP jacket. The lateral confining pressure can be evaluated according to the equilibrium of the confining material ($\sigma_2 \cdot R = \sigma_{FRP} \cdot t$) shown in Figure 3.3. The stress in FRP can be determined based on the horizontal strain gauge readings and the FRP elastic properties. Therefore, both axial and lateral stress can be determined and thus the stress path of the confined concrete cylinder under uniaxial load can be plotted, as shown in figure 3.4.

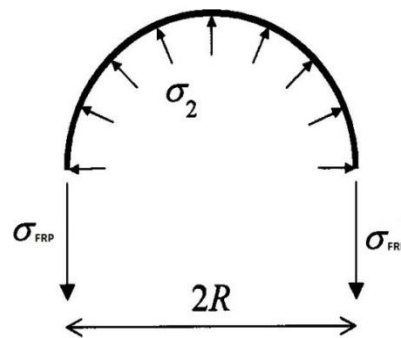


Figure 3.3 Stress equilibrium in FRP confinement

In Figure 3.4, the stress path of the FRP-confined concrete cylinder under uniaxial load is compared with the uniaxial load path and the compressive meridian. It is clear that FRP-confined concrete follows a uniaxial load path before it reaches the failure surface, and afterwards moves along the compressive meridian until the rupture of FRP.

The relationship between axial stress and lateral confining pressure provided by the FRP is illustrated in Figure 3.5. It is shown that the lateral confining pressure is less than 1 MPa when the axial stress applied is equal to its unconfined strength. That is, the initial confining effect of FRP is negligible and concrete can be regarded as unconfined as long as the concrete is within the failure surface on of the uniaxial load path. Once the uniaxial stress exceeds the unconfined concrete strength, FRP is mobilised to prevent concrete from failure.

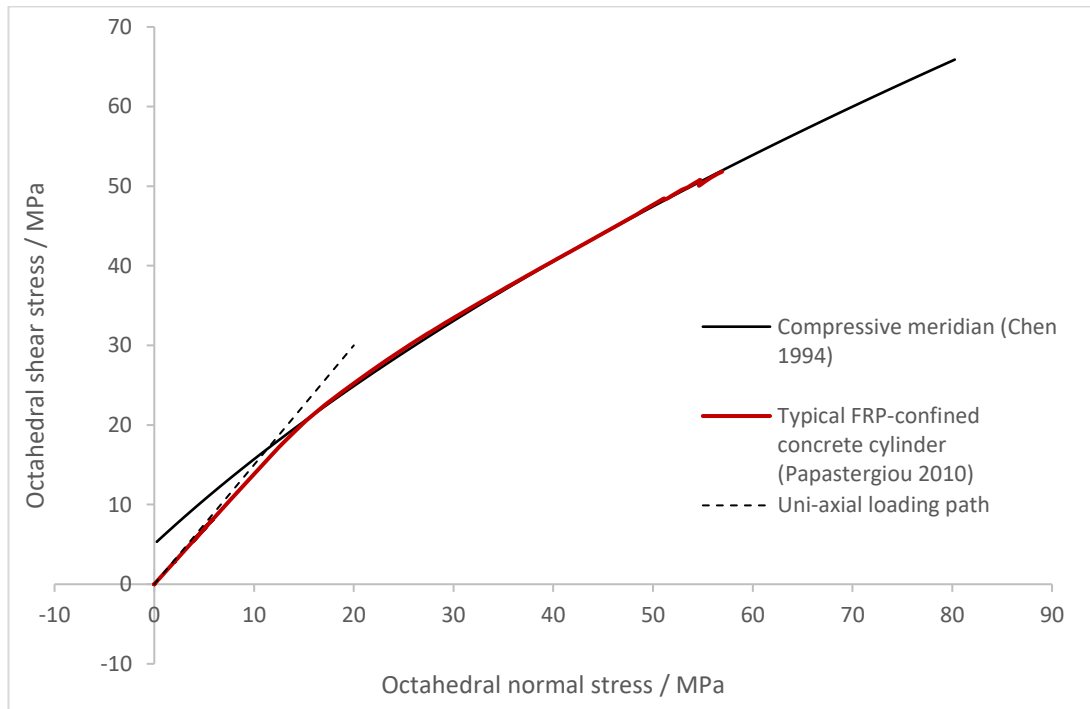


Figure 3.4 Stress path of concrete cylinder with FRP confinement under uniaxial load

Kotsovos & Newman (1977) investigated the crack propagation of concrete cylinders under axisymmetric loads. It was observed that the cracking propagation becomes unstable after a certain state of stress, which leads to a new envelope, the “onset of unstable cracking” envelope (or OUFP). However, within the OUFP envelope the crack propagation is stable. That is, provided the current stresses applied are maintained inside the OUFP envelope, the crack propagation stops, and the passive confinement (e.g. FRP) cannot be effectively activated. However, if the stress state is outside of the OUFP envelope, cracking propagation becomes unstable, and thus FRP will be stretched by the lateral expansion of concrete.

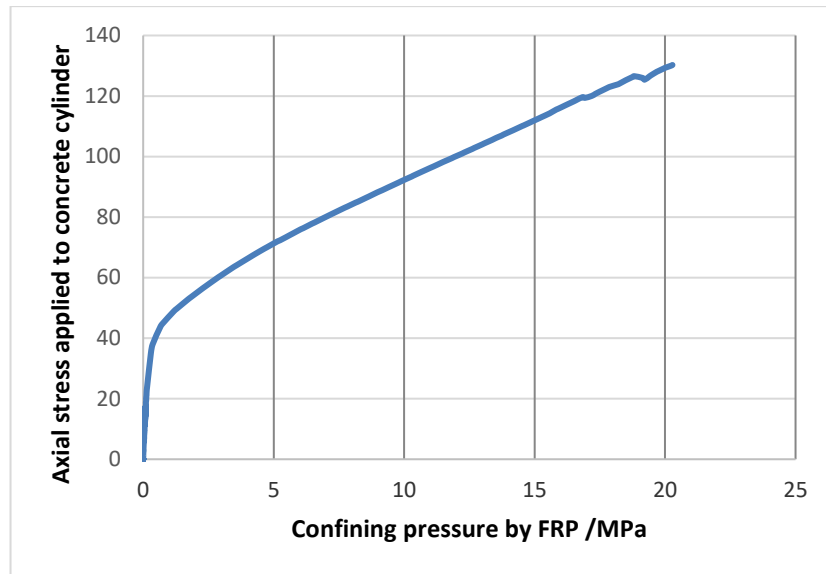


Figure 3.5 Axial stress and confining pressure applied to the concrete cylinder in the test by Papastergiou (2010)

The OUFP envelope has been found to be very close to the failure surface and indicates the onset of volumetric expansion (Kotsovos, 1979). Hence, in uniaxial tests on FRP-confined concrete, when the stress state is on the failure surface, unstable vertical crack occurs and the FRP is stretched. With the confining pressure provided by the FRP, the unstable cracking is stopped, and the concrete is maintained along its failure surface.

In summary, the load path of the uniaxial test of FRP-confined concrete can be roughly divided into two parts: the uniaxial load path ($d\sigma_1 \neq 0$; $d\sigma_2 = d\sigma_3 = 0$) and the path along the failure surface (Figure 3.4). The confining pressure can be neglected before the concrete reaches its unconfined strength, and once the uniaxial load exceeds the concrete unconfined strength ($\sigma_1 > f_c$), the FRP confinement is effectively activated to delay concrete failure. The concrete is then maintained on the compressive meridian. Therefore, this indicates that concrete confined by FRP behaves as a perfect plastic material when subjected to compressive load.

3.2 Drawbacks in the FRP-confined concrete cylinder tests

The hypothesis proposed in the previous section is based on compression tests of concrete cylinders wrapped by FRP lateral confinement. However, there are a

number of limitations in the experimental set-up, which may affect the reliability of the test results, and thus the hypothesis derived from such results. In this section, the details of the cylinder tests are reviewed.

3.2.1 Imperfect boundary condition

The concrete cylinder specimens in conventional tests are normally with the dimension of 100mm×200mm or 150mm×300mm. Having cured more than 28 days, concrete cylinders are wrapped with FRP by the wet lay-up process.



Figure 3.6 Specimen preparation of experimental tests (Papastergiou, 2010)

In the wet lay-up process, the fabric sheet is cut to a certain length and impregnated with wet resin using a brush, as shown in Figure 3.6. The wet sheet is then wrapped around the concrete cylinder. The fibres of the confining material are placed in the hoop direction, such that when the concrete cylinder is subjected to a vertical load, the evolution of vertical cracks is constrained. Strain gauges are attached to FRP to monitor the deformation of the specimen during loading. Hence, both the loading history and the deformation history can be monitored in the process of testing. To prevent the premature failure of the lateral confinement (e.g. slipping), the FRP is wrapped with an overlap as shown in Figure 3.7. However, such an overlap causes a non-uniform distribution of lateral strain in the hoop direction.

According to results from the tests conducted by Papastergiou (2010), the strain gauge reading (α_1) at the overlap region was much smaller than those of the other gauges (α_2, α_3), and the ultimate strain at the overlap region for one layer FRP was only half of that at the other region.

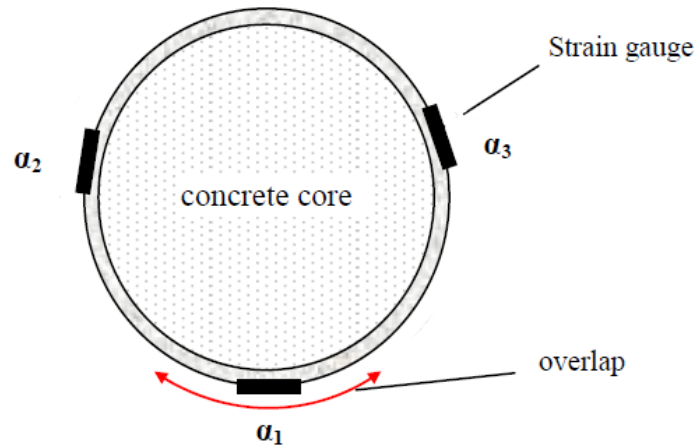


Figure 3.7 Layout of lateral strain gauges

All the strain gauges were placed at the mid-section of the specimen. To avoid failure at other places (e.g. the top or bottom of the cylinder), additional prestressed metallic straps were installed at the top and the bottom, as shown in Figure 3.1. That is, the confining stiffness was not constant along the vertical direction, and the expansion at mid height was larger than that at the ends. Therefore, a shear component may develop in both stress and strain tensors.

Hence, in the experimental tests, the ideal boundary condition was not strictly met, and thus uniformly distributed stress and strain could not be realised.

3.2.2 Indirect measurement

The strain gauges were attached to the FRP instead of directly onto the concrete cylinder. As a result, the strain of the concrete cylinder was obtained indirectly. Apart from the strain, the lateral confining pressure was also evaluated indirectly according to the force equilibrium in the lateral confinement, as illustrated in Figure 3.3.

According to the equilibrium, the relationship between the confining pressure (σ_l) and the tensile stress in the FRP (σ_{FRP}) can be expressed as follows:

$$\sigma_l = \frac{\sigma_{FRP} \cdot t}{R} \quad (3.1)$$

With the assumption that FRP sheet behaves as a linear-elastic material:

$$\sigma_l = \frac{E_{FRP} \cdot \varepsilon_{FRP} \cdot t}{R} \quad (3.2)$$

Therefore, the accuracy of the confining pressure evaluation depends on the precision of the lateral strain reading. As discussed in the previous section, the lateral strain reading can be heavily affected by the overlap. Errors in lateral strain measurement can lead to unreliable evaluation of the confining pressure on the concrete.

3.2.3 Difficulty of investigating less lateral confinement

According to Equation 3.2, the confining stiffness, which is the increment of confining pressure to the concrete at unit lateral expansion, can be expressed as:

$$k_l = \frac{E_{FRP} \cdot t}{R}$$

For a large structural element, a bridge pier for instance, the diameter can be up to 1000 mm. To ensure the same level of confining stiffness, the thickness of FRP to a testing cylinder specimen should be 10 times smaller than that of the bridge pier. Hence, it might be of interest to investigate the behaviour of concrete specimen with less lateral confinement, even less than 1 layer of FRP. However, this is impractical, since the minimum value of the fibre sheet thickness is constrained by the supplier.

3.3 Multiaxial tests using Mac^{2T}

The research group at the University of Sheffield attempted to make use of the apparatus Mac^{2t}, originally designed for true tri-axial tests, to physically simulate the scenario of concrete with passive confinement under loads; that is, applying the load on a concrete cubic specimen in one direction while independently updating the confining pressure in the other two directions according to its lateral expansion. Such a novel use of the true tri-axial testing apparatus allows the identification of the loading path of passively confined concrete under compressive load. It is worth emphasising that the compressive pressure in the lateral directions, which represents the confining pressure, was not predefined. Instead, its value was

continuously updated according to the lateral expansion of the concrete, such that the scenario of passive confinement was realised.

Such novel use of Mac^{2T} is believed by the author to overcome the deficiencies of previous tests on FRP-confined concrete cylinders. To be more specific, the stress and strain were uniformly distributed in the specimen tested by Mac^{2T}. The confining pressure was also directly measured. Additionally, there was flexibility for the application of any level of confining stiffness. The loading history was recorded and compared with the concrete failure surface and the test results were then used to facilitate the calibration of the material constitutive model.

It has been noted by Gerstle et al. (1980) when comparing the multiaxial test results from different resources, that the test results were significantly scattered in terms of the failure surface. This may be due to both material and testing method variability. In addition, when the failure surface function was calibrated for different multiaxial tests, the size and shape of the failure surface varied (Chen, 1994). To minimise this variability, multi-axial tests through Mac^{2t} with conventional loading paths were planned to investigate the failure surface of the concrete. The concrete specimens were firstly subjected to an increasing hydrostatic pressure up to a given level. Then, the compressive load was increased in one direction while maintaining the other two until the compressive load reached its peak value.

In the following section, the experimental set-up is detailed, including specimen preparation and the control system of Mac^{2t}. Following this, the details of the testing scheme are illustrated.

3.3.1 Experimental set up -- Mac^{2T}

The apparatus Mac^{2t} is equipped with three independent and orthogonal loading frames, as illustrated in Figure 3.8 (a). Therefore, it is capable of subjecting the concrete cubic specimen to a multi-axial stress state. In each frame, the compressive stress to the specimen is generated by an actuator with 4MN load capacity, as shown in Figure 3.8 (b).

The specimen is in contact with a rigid platen, and therefore the boundary of the specimen is loaded with uniform displacement. In true axial tests, a uniformly distributed stress in the specimen is vital. This requires avoiding any eccentricities in the specimen, eliminating friction on the specimen's boundary and precisely shaping the cubic specimen.

To avoid eccentricity, the specimen is placed in the centre of the forces at the onset of testing. The horizontal frame X and Y is supported on a low friction roller bearings and the horizontal position of the specimen is maintained during loading and unloading. An additional actuator (the 4th) was installed beneath the Z frame to adjust the level of Z frame interactively, such that the centre of the cubic specimen remains at the same height during the entire testing process. Measures taken to meet the other two requirements are explained in the following section.

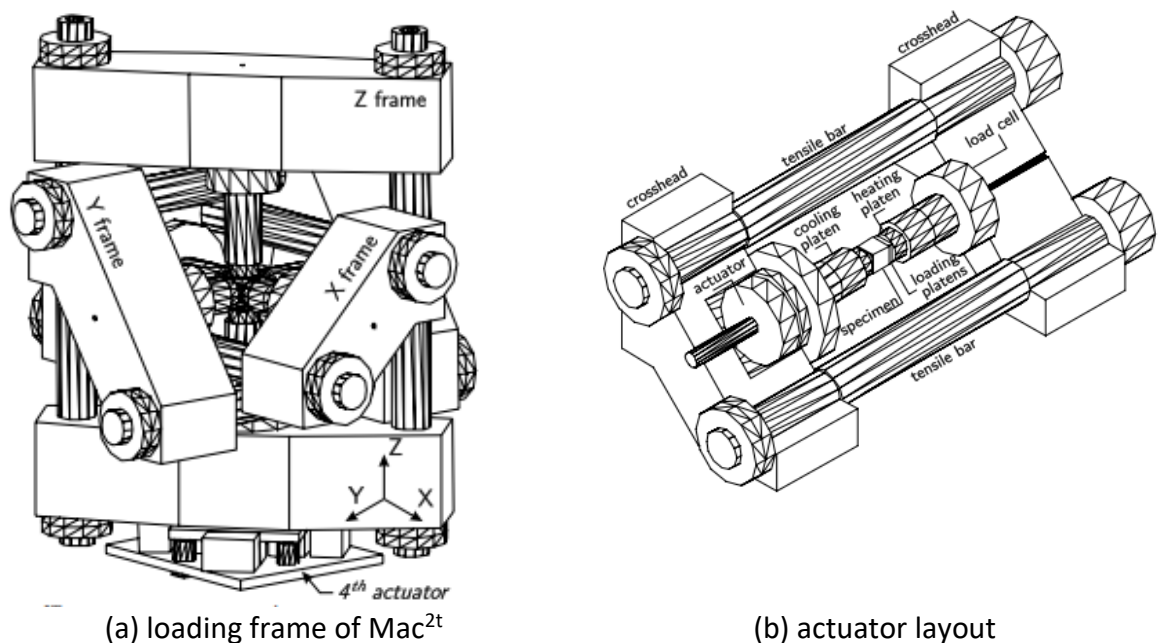


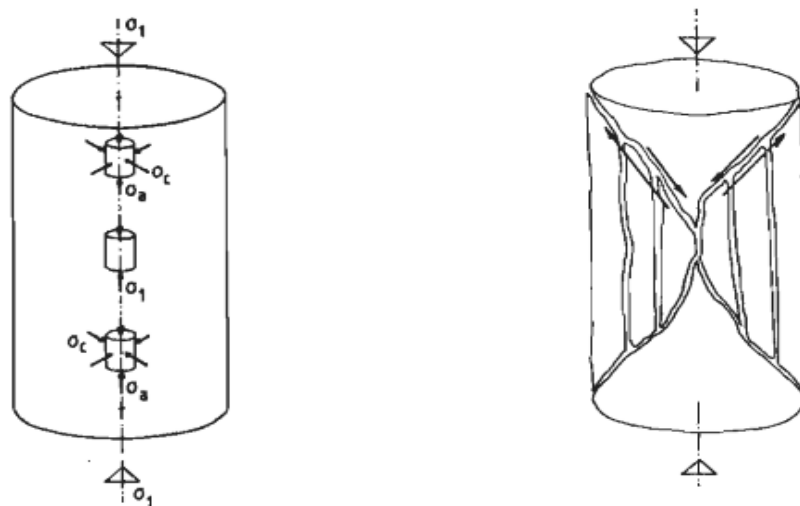
Figure 3.8 Design of Mac^{2t} (Petkovski et al., 2006)

3.3.1.1 Friction on the boundary of the specimen

In previous uniaxial compressive tests on the concrete cylinders, the test results were affected by the constraint between the specimen and the loading platen. This is because, as the compressive load increases, the cylinder specimen tends to expand laterally, and this activates friction on the specimen's boundary. Because of

the combination of the uniaxial load and the friction, the ends of the specimens are in a multiaxial stress state, as illustrated in Figure 3.9.a. The inclined cracks normally observed at the ends of the specimen are the result of the multiaxial stress state. The failure mode of the concrete cylinder under compressive load is illustrated in the Figure 3.9.b. Hence, the concrete compressive strength obtained from the cylinder tests may be overestimated due to the multiaxial compressive stress.

The effect of the friction on strength enhancement can be minimised by increasing the height of the specimen, since the friction at the specimen's ends has little effect on the middle of the specimen. A parametric study regarding specimen slenderness, represented by an index "height-diameter ratio" (h/d), was conducted by Van Mier (1984). With the increase of specimen height, it was found that the uniaxial compression test results became smaller. In addition, if h/d was larger than 2, vertical splits were observed in the middle. As a result, the uniaxial compressive test results of cylinders with h/d of 2 were deemed to represent unconfined concrete strength. This has become a benchmark for other types of concrete tests.



(a) stress state in the specimen (b) failure mode of the cylinder

Figure 3.9 The stress state and crack formation of concrete cylinders

(Van Mier 1984)

Similarly, in the true tri-axial tests friction at the specimen boundary can also develop due to the interface constrain. To minimise such interface friction, many attempts have been made, including: lubricated platens (Bertacchi & Bellotti, 1972),

brush bearing platens (Linse & Aschl, 1976), flexible platens (Schickert & Winkler, 1977) and fluid cushions (Ko & Sture, 1974). To evaluate the effect of these measurements, Gerstle et al. (1980) conducted a cooperative study where all laboratories with different multiaxial testing set ups used specimens of the same concrete. The test results are illustrated in Figure 3.10 and normalised by the concrete's uniaxial strength obtained from cylinder tests. The concrete cubic strength obtained from the tests with the frictionless measurements was reduced by approximately 20% compared to that of the test without friction reduction (dry platens).

Lubricated rigid platens exhibit relatively low restraint in the tests that have investigated concrete post-peak behaviour (Petkovski al., 2006). Therefore, lubricated rigid platens were used in Mac^{2t} in this research. A steel tile (1 mm thickness) coated with PTFE (0.25 mm thickness) was placed between the rigid platen and the cubic specimen as a measure of lubrication.

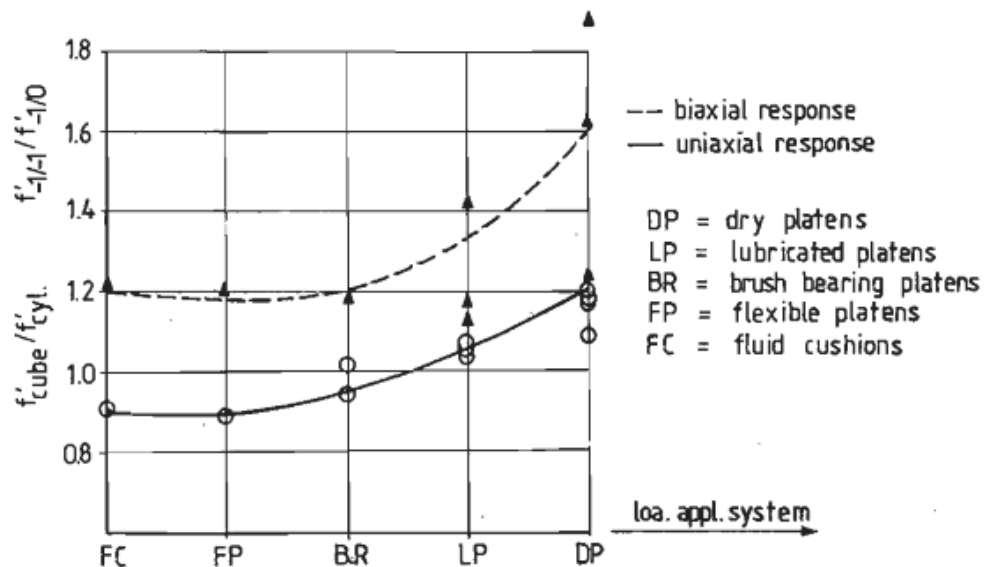


Figure 3.10 Dependence of concrete strength on different loading application systems (Gerstle et al, 1980)

3.3.1.2 Specimen preparation

As discussed previously, the specimen should be as precisely cubic as possible: any deviance disturbs the uniform distribution of stress. For this research a large block

of concrete was cast. After having cured for more than 28 days, the block was cut into cubes with a dimension of 105 mm. The cube was then ground and polished such that the length of the edges was shortened to $100 \pm 1\text{mm}$ and the difference between edges in one direction was less than 0.1mm .

Ready mix concrete was used and the specified mix design is shown in Table 3.1. The concrete was cast on 28/02/2018 and demoulded two days later. The concrete blocks were then placed in a curing room until June when the blocks were taken out, cut into cubes and ground. The Gantt chart shown in Table 3.2 illustrates the process of the specimen's preparation.

Table 3.1 Concrete mix design

Material	Type	Supplier	Source	kg/m ³
Cement	CEM I (Rugby cement)	Cemex	Rugby Works	150
Coarse aggregates	Graded gravel (4-20 mm)	Aggregate Industries	Newbold	1097
Fine aggregates	Sand MP Gravel (0-4mm)	Aggregate Industries	Woodhall	804
GGBS		Holcim	Bremen	150
Admix	Plasticiser	SIKA	10RM Sikaplast	2.25 (lt/m ³)
WCR				0.55

Table 3.2 The process of specimen preparation

	Feb	Mar	Apr	May	Jun	Jul	Aug	Sep
1. Casting	—							
2. Demoulding	—							
3. Curing		—	—	—				
4. Sawing					—			
5. Grinding					—	—	—	—

3.3.1.3 Control system of Mac^{2T}

The operation of Mac^{2T} is done using an in-house developed control system. A control loop is carried out at a fixed interval and consists of four steps: acquiring data from sensors, averaging data, calculating control variables and sending a signal to servo-valves of the actuators (Petkovski et al., 2006). Two computers are responsible for processing the data.

In the load control testing mode, the loading history is pre-defined. During the testing, the load is monitored using a full bridge sensor in the loading cell. The load rate is the control variable, which is calculated based on the difference between the current load and the predefined loading history. Following this, the load rate is sent back to the actuator and updated in every loop, so that the load actually applied on the specimen can tightly fluctuates around the predefined loading history. With an updating interval of 1-3 s, errors can be neglected.

The deformation of the cubic specimen under load is measured using a laser interferometer system, the schematic diagram of which is illustrated in Figure 3.11. Each facet of the cubic specimen is touched by a pin connected to a retro-reflector. The laser beam, generated from a laser head, is transmitted through a vacuum tube inside the actuator to detect any movement ($10^{-6} - 2.5 \cdot 10^{-3} m$) of the retro-reflector. The data regarding the facet translation is then passed to the computer, based on which the strain is calculated. For the cubic specimen of 100 mm edge length, the system was capable of detecting a minimum strain of 10^{-5} .

In displacement control testing mode, the deformation rate is the control variable. In the control loop, the transition of the specimen boundary is firstly measured using the laser interferometer system, based on which the deformation in terms of strain is calculated. The deformation rate is calculated according to the difference between the current deformation and predefined deformation, and then the command signal is sent to the actuator valve.

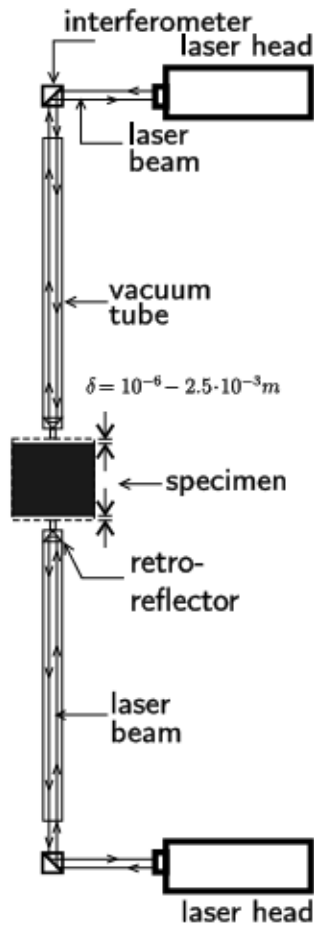


Figure 3.11 Schematic diagram of laser interferometer system

(Petkovski et al., 2006)

Both two loading modes require a predefined criterion. In other words, either loading history or displacement history needs to be defined in advance of the testing. For instance, in the concrete multiaxial test which aimed to determine the compressive meridian of the failure surface, the loading control mode was employed in all three frames to apply a hydrostatic pressure. Afterwards, the pressure in the x and y directions was maintained by the load control mode, while increasing the load in the z-direction up to failure in the displacement control mode. The loading path is illustrated in Figure 3.12.

However, in the tests of passive confinement simulation, the confining pressure applied to the specimen was with respect to its lateral expansion, and it was

impossible to employ either the load control mode or the displacement control mode in the x and the y loading frame. A control program was needed to realise this physical simulation.

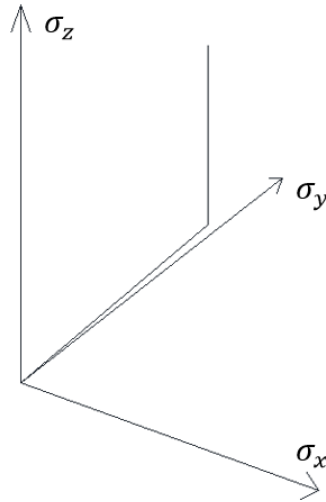


Figure 3.12 Loading path of multiaxial test with active confinement

3.3.1.3.1 Process variables in the simulation of passive confinement

In the control program for passive confinement simulation, the confining pressure σ_l and the lateral expansion ε_l became process variables. The relationship between these two variables is expressed by the following equation:

$$\sigma_l = k \cdot \varepsilon_l \quad (3.3)$$

where the parameter k is the confining stiffness. Since the multiaxial tests aimed to physically simulate the scenario of FRP-confined concrete cylinder under axial load, the parameter k was predefined to reflect the level of passive confinement.

The force equilibrium in FRP-confined concrete cylinder is illustrated in Figure 3.3. The corresponding equation is thus expressed as follows:

$$\sigma_2 = \frac{\sigma_{FRP} \cdot t}{R} = \frac{E_{FRP} \cdot \varepsilon_{FRP} \cdot t}{R} \quad (3.4)$$

where

E_{FRP} is the Young's modulus of FRP;

ε_{FRP} is FRP strain;

t is the thickness of FRP and

R is the radius of the concrete cylinder.

As the deformation in FRP was consistent with that in concrete, ε_{FRP} was equal to concrete strain in the loop direction. The concrete cylinder met the axisymmetric boundary condition; therefore, the strain in the loop direction was equal to that in the radial direction.

$$\varepsilon_{FRP} = \varepsilon_{loop} = \varepsilon_2 \quad (3.5)$$

Equation 3.4 can be expressed as follow:

$$\sigma_2 = \frac{E_{FRP} \cdot t \cdot \varepsilon_2}{R} \quad (3.6)$$

It should be noted that σ_2 and ε_2 are principal stress and principal strain, respectively. By comparing Equation 3.3 and Equation 3.6, the parameter k can be calculated as follows:

$$k = \frac{E_{FRP} \cdot t}{R} \quad (3.7)$$

To recreate the same stress state as in the FRP-confined concrete cylinder, the concrete cubes were loaded vertically while the lateral pressure was updated according to its lateral expansion. Figure 3.13 illustrates the lateral transition of the boundary of the specimen in the x-direction, as a result of the vertical load.

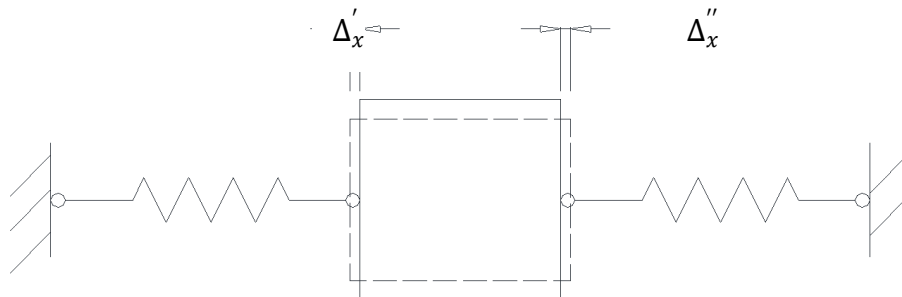


Figure 3.13 Constrains in the lateral direction

The elongation in the x-direction, Δ_x :

$$\Delta_x = \Delta'_x + \Delta''_x \quad (3.8)$$

It follows that the strain in the x-direction is:

$$\varepsilon_x = \frac{\Delta'_x + \Delta''_x}{l_x} \quad (3.9)$$

Similarly, the lateral strain in the y-direction is:

$$\varepsilon_y = \frac{\Delta'_y + \Delta''_y}{l_y} \quad (3.10)$$

There might have been a difference between deformation in the x and the y direction, so an average value was taken as the process variable ε_l :

$$\varepsilon_l = \frac{\varepsilon_x + \varepsilon_y}{2} \quad (3.11)$$

3.3.1.3.2 Program to simulate passive confinement

In the control loop, the input was the lateral transition of the cubic specimen ($\Delta'_x, \Delta''_x, \Delta'_y, \Delta''_y$) according to the reading from the laser interferometer system, while the output was the loading rate of the actuator (R) to be sent back to the actuator valve. The flow chart of a control loop is illustrated in Figure 3.14.

The strain in the x and the y direction ($\varepsilon_{x,i}$ and $\varepsilon_{y,i}$) was first calculated based on the inputs; the translation of the specimen boundaries. The current process variable lateral strain ($\varepsilon_{l,i}$) was then obtained according to Equation 3.11. Afterward, the strain increment ($\Delta\varepsilon$) was calculated. The need for confining pressure increment ($\Delta\sigma$) could then be evaluated based on the strain increment using Equation 3.3. Finally, $\Delta\sigma$ was transferred into loading rate R and the signal sent to the actuator valve.

Such a control loop was used at a fixed interval (t). It is worth mentioning that the load rate applied at the current loop was based on the deformation that occurred during the previous loop. That is, the lateral load applied was one step behind. To minimise the corresponding error, the interval of updating the load rate (t) should not be too large, and so was set at every 1.4 seconds. However, if sudden expansion of specimen occurs, this would trigger a huge load rate. To protect Mac^{2t} from over-

reaction, the load rate (R) was set with a lower and a higher boundary, -20 and 60 kN/s respectively.

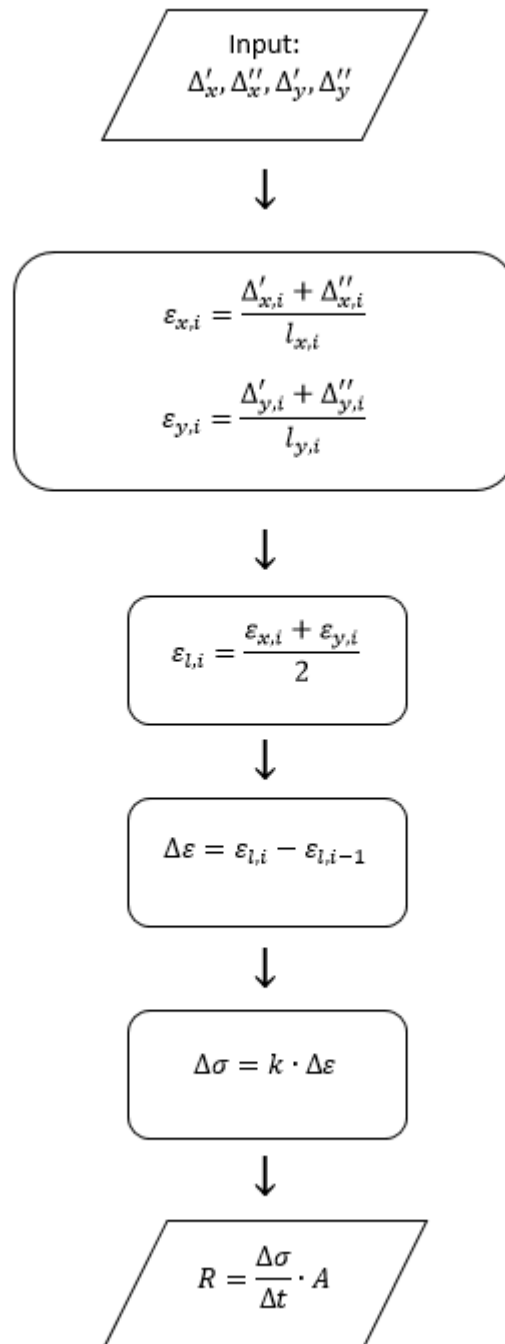


Figure 3.14 Flow chart of the control loop

3.3.2 Testing scheme

In general, there were two kinds of multiaxial tests conducted through Mac^{2T}, one with active confinement and the other with passive confinement. The former aimed to determine the concrete strength criterion, failure surface; while the latter was for physical simulation of an FRP-confined concrete cylinder under compressive loads.

To confirm the proposed hypothesis, the loading history of passive confinement simulation was compared with the failure surface. In the tests with passive confinement, the three principal stresses were in the following order (negative in compression):

$$0 > \sigma_1 = \sigma_2 > \sigma_3$$

where σ_1 and σ_2 represent confining pressure in the x and the y direction respectively, and σ_3 indicates the compressive load in the z direction. Hence, only the compressive meridian of failure surface was needed in the tests with active confinement.

3.3.2.1 *Multiaxial tests with active confinement*

In this group of tests, the loading path was predefined. Hydrostatic pressure was first applied. Then, the compressive pressure in the two directions was kept constant while load was applied in the other direction up to failure. The typical loading path is illustrated in Figure 3.12. Apart from the strength criterion, elastic mechanical constants (e.g. Young's modulus and Poisson's ratio) were also obtained.

The steps for multiaxial tests with active confinement were as follows:

1. Contact stress of 0.7 MPa was applied to the specimen in all three directions.
2. Hydrostatic pressure was then applied in the load control mode up to a given level.
3. Compressive pressure was maintained in the x and the y-direction while displacement in the z direction was increased in displacement control until the concrete crushed.

The level of hydrostatic pressure applied in the second step represents the level of active confinement. Several tests were conducted with different active confining pressure applied, shown in Table 3.3.

Table 3.3 Confining pressure at the end of step 2

Specimen No.	Confining pressure/MPa
R1	0.7
R2	5
R3	10
R4	20
R5	30

3.3.2.2 *Multiaxial tests with passive confinement*

The steps for multiaxial tests with passive confinement are as follows:

1. Cubic specimens were placed in the middle of Mac^{2T} and a contact stress of 0.5 MPa was applied to the specimen in all three directions.
2. The load in the z direction was increased in displacement control while confining pressure was updated according to the lateral expansion and confining stiffness.

The predefined parameter for the confining stiffness was determined from Equation 3.17. Assuming a concrete cylinder of diameter 102 mm was confined by CFRP. The Young's modulus (E_{FRP}) and the thickness of CFRP (t) were taken as 241000 MPa and 0.185 mm respectively. For the cylinder confined by n layers of CFRP, the parameter k is as follows:

$$k = \frac{E_{FRP} \cdot n \cdot t}{R} = \frac{241000 \cdot n \cdot 0.185}{51} = n \cdot 874 \text{ MPa}$$

Several multiaxial tests with a different level of passive confinement were conducted, the details of which are listed in Table 3.4.

Table 3.4 Confining stiffness for multiaxial tests with passive confinement

Specimen No.	Confining stiffness (k) MPa	Equivalent to the 102 mm cylinder confined by:

P1	2622	3 Layers of CFRP
P2	1748	2 Layers of CFRP
P3	1748	2 Layers of CFRP
P4	1748	2 Layers of CFRP
P5	874	1 Layers of CFRP
P6	874	1 Layers of CFRP
P7	437	0.5 Layers of CFRP
P8	174.8	0.2 Layers of CFRP

3.4 Experimental test results

3.4.1 Test results of multiaxial tests with active confinement

The section presents and discusses the experimental test results on concrete specimens with active confinement. The stress state of concrete under different levels of constant confining lateral pressure are also presented. Based on the stress state corresponding to the peak compressive load, the compressive meridian of failure surface is determined. Finally, the elastic modulus and Poisson's ratio are evaluated.

3.4.1.1 Stress-strain relations

The multiaxial test results of concrete with active confinement are illustrated in Figure 3.15 in the form of stress-strain relationships. With an increase of confining pressure σ_l , concrete specimens exhibit enhanced strength and deformation. The strength of concrete specimen R5 with a constant confining pressure of 30 MPa was enhanced by around three times, compared to that of R1 with little confinement. Apart from strength enhancement, concrete ductility was also improved by the confinement. The load capacity of R1 dropped by around 20% of its peak strength at a vertical strain of 0.003. In comparison, for R4 and R5 with lateral confinement of 19.7 and 30 MPa, respectively, there was little strength decrease that could be observed in the post peak region.

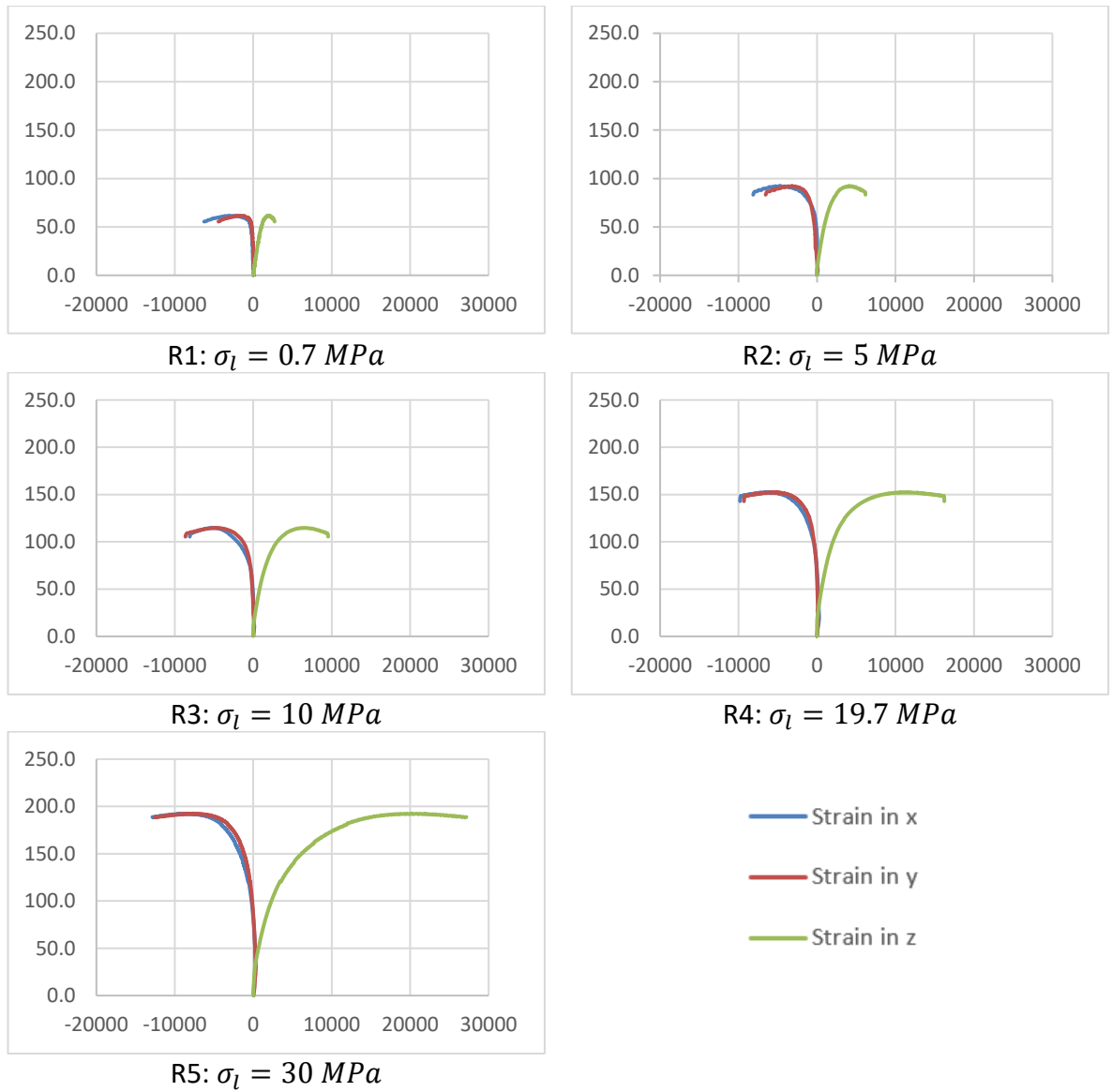


Figure 3.15 Stress-strain relation of concrete with active confinement

3.4.1.2 Compressive meridian of the failure surface

Table 3.5 shows the stress state of the specimen when the compressive load reached its peak, corresponding to a point on the failure surface of the concrete in the stress space. The failure surface is the boundary of all the possible stress states, and therefore represents the strength of the concrete. The compressive meridian is a curve on the failure surface where the principal stress meets the following condition (compressive stress is negative):

$$\{(\sigma_1, \sigma_2, \sigma_3) | 0 > \sigma_1 = \sigma_2 > \sigma_3\}$$

In the multiaxial tests with active confinement, the compressive stresses in the x and the y-direction which represent the lateral confinement were identical and smaller than the vertical stress. Therefore, it was only necessary to investigate the compressive meridian.

For mathematical convenience, the equation of the compressive meridian is always expressed in terms of the equivalent pressure stress (p) and the Mises equivalent stress (q), which can be converted by principal stresses as follows:

The equivalent pressure stress is:

$$p = -\frac{1}{3} \cdot (\sigma_1 + \sigma_2 + \sigma_3) \quad (3.12)$$

The Mises equivalent stress is:

$$q = \sqrt{\frac{1}{2} [(\sigma_1 - \sigma_2)^2 + (\sigma_2 - \sigma_3)^2 + (\sigma_3 - \sigma_1)^2]} \quad (3.13)$$

Table 3.5 Stress state when the load reaches the peak

Specimen No.	Confining pressure (σ_l) / MPa	Vertical load (f_c) / MPa	p / MPa	q / MPa
R1	-0.7	-61.6	21	60.9
R2	-5	-92.5	34.2	87.5
R3	-10	-114.8	44.9	104.8
R4	-19.7	-152.5	64	132.75
R5	-30.1	-192.6	84.3	162.5

Based on these five data points, a statistical analysis was conducted to estimate the compressive meridian and a trend line was obtained:

$$q = 1.67 \cdot p + 26.1 \quad (3.14)$$

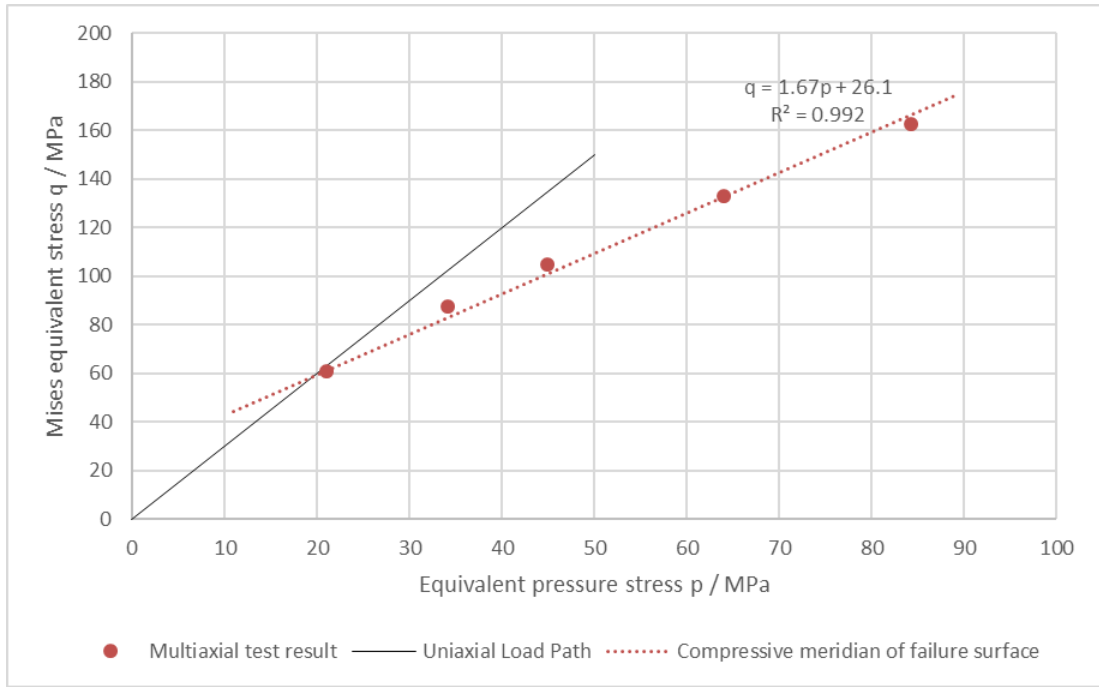


Figure 3.16 The trend line of test results in p-q coordinate

As illustrated in Figure 3.16, the trend line agrees well with the data points. Apart from the trend line, the uniaxial load path is also plotted in Figure 3.16, the equation of which can be expressed as:

$$\sigma_2 = \sigma_3 = 0 \quad (3.15)$$

Which is equivalent to in the p-q coordinate system:

$$q = 3 \cdot p \quad (3.16)$$

The intersection of these two lines represents the unconfined concrete strength. By substituting Equation 3.16 into 3.14, the unconfined concrete strength (f_c) was obtained, as 59 MPa.

3.4.1.3 Tangent modulus and Poisson's ratio

For the active confinement tests, after the application of hydrostatic pressure, a stress increment is applied in the z direction. In this case, the tangent modulus and the Poisson's ratio can be calculated as follows:

Tangent modulus E_t :

$$E_t = \frac{\Delta\sigma_z}{\Delta\varepsilon_z} \quad (3.17)$$

The Poisson's ratio may be calculated by either:

$$v = -\frac{\Delta\varepsilon_x}{\Delta\varepsilon_z} \quad (3.18.a)$$

Or:

$$v = -\frac{\Delta\varepsilon_y}{\Delta\varepsilon_z} \quad (3.18.b)$$

However, as it is possible for the strain in the x and the y direction to differ, the average value was taken from the above two equations as follows:

$$v = -\frac{\Delta\varepsilon_x + \Delta\varepsilon_y}{2 \cdot \Delta\varepsilon_z} \quad (3.19)$$

The history of E_t and v are shown plotted against the normalised vertical load, which is normalised using its peak value. As illustrated Figure 3.17, the tangent modulus E_t gradually decreases, eventually to zero, when the vertical load reaches the peak. For R1, with slight active confinement of 0.7 MPa, the tangent modulus remains above 45 GPa until the vertical load reaches 70% of its peak value (42/61 MPa). Compared to R1, the tangent modulus of the other four specimens reduces to less than 45 GPa much earlier. This is especially true of R5 where the tangent modulus dips below 45 GPa just after the beginning of step 3. That is, the uniaxial elastic stiffness reduces at higher levels of hydrostatic pressure. This agrees well with the observation from other multiaxial compression tests such as those of Kotsovos & Newman (1977). Hence, with more lateral active confinement, concrete exhibits a more flexible behaviour even if its strength and ductility are enhanced.

According to "Standard Test Method for Static Modulus of Elasticity and Poisson's Ratio of Concrete in Compression" (ASTM, 2002), the Young's modulus of concrete is evaluated based on experimental tests on concrete cylinders under uniaxial compressive loading, and the Young's modulus is the secant slope of the axial stress-strain curve at $0.4 \cdot f_c$. The test results of R1 were used to evaluate the secant module, which was found to be 57 GPa.

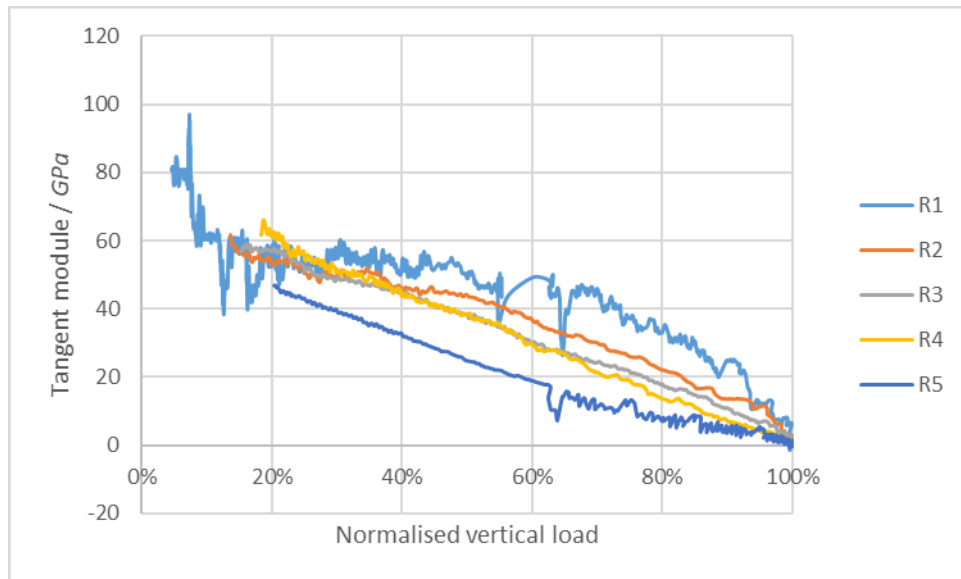


Figure 3.17 Tangent modulus history

As illustrated in Figure 3.18, the Poisson's ratio of all the specimens fluctuated around 0.22 when the vertical load was less than 40% of its maximum value. This is expected, as at this load level the concrete is expected to exhibit a linear elastic behaviour; as a result, Poisson's ratio remains constant.

When the vertical load exceeded 40% of its capacity, the rate of increase in the value of Poisson's ratio varies among the five tests. For R1 and R2 where the active confinement was low (0.7 and 5 MPa respectively), the Poisson's ratio dramatically increased, especially when the vertical load exceeds 90% of its peak value.

It has been observed by Kotsovos and Newman (1977) that unstable cracks form in the concrete as the load approaches its capacity. Therefore, unstable cracks formed and dominated the lateral deformation at the end of test R1 and R2. This means that small vertical strain increments can result in large lateral expansion. Pantazopoulou & Mills (1995) corresponded the concrete strength to its lateral expansion. That is, the concrete's strength is impaired by unstable cracks. As is illustrated in Figure 3.15, R1 and R2 exhibit an obvious decrease of strength in the post-peak region.

On the contrary, for high levels of lateral confinement (specimen R4 and R5), the Poisson's ratio only gradually rises after the initial elastic stage, reaching just above 0.5. This means that the ratio between the lateral and the vertical strain increment

is relatively stable, and that the unstable cracks are effectively controlled at high levels of lateral confinement. In the post-peak region of the R4 and the R5 stress-strain curves, the decrease of load capacity almost disappears.

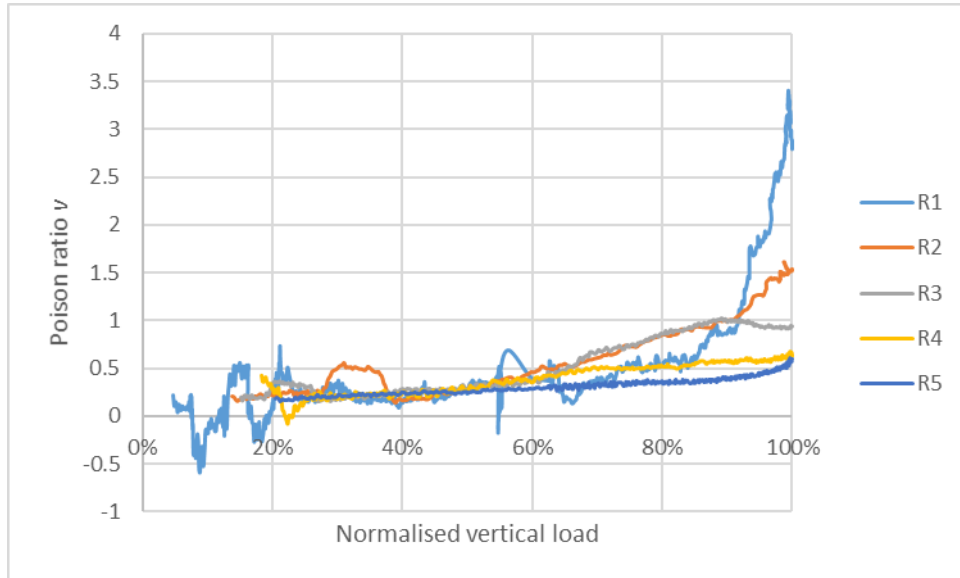


Figure 3.18 Poisson's ratio history

3.4.2 Test results of multiaxial tests with passive confinement

In this section, the effectiveness of the passive confinement of Mac^{2T} applied to concrete specimens is initially evaluated. The test results of passively confined concrete under compressive load are then illustrated in the form of stress-strain curves. Following this, the loading paths are plotted and compared to the compressive meridian of the failure surface, in order to assess the proposed hypothesis. Finally, the effect of confining stiffness on the deformation of concrete specimens is investigated

3.4.2.1 Evaluation of the effectiveness of the control program

To evaluate the effectiveness of the control program, linear regression analysis was conducted on all test results. The confining pressure applied to the specimen is plotted against lateral strain in Figure 3.19. The regression equation and the regression parameter (R^2) are also illustrated. The former is a trend line of the data points, the slope of which represents the actual confining stiffness. The latter, R^2 , indicates a correlation between the trend line and the data points (i.e. the fit of the regression equation to the data points). The closer R^2 is to 1, the better the regression equation fits the data points. Overall, the R^2 of all the regression analyses are close to 1, and therefore the linear equations can be accepted. It follows that the slope of the equations can be regarded as the actual confining stiffness to be compared with the predefined parameter K .

Table 3.6 shows the comparison between the predefined confining stiffness and the slope of the trend line of the tests results. These two values for each test are close with only a slight difference between each other. The loading rate given to the actuator valve in the current control loop is based on the lateral strain increment that occurred in the last loop. As a result, the lateral confining pressure is always one step behind. This explains why the confining stiffness obtained from regression analysis is around 2% lower than the predefined one.

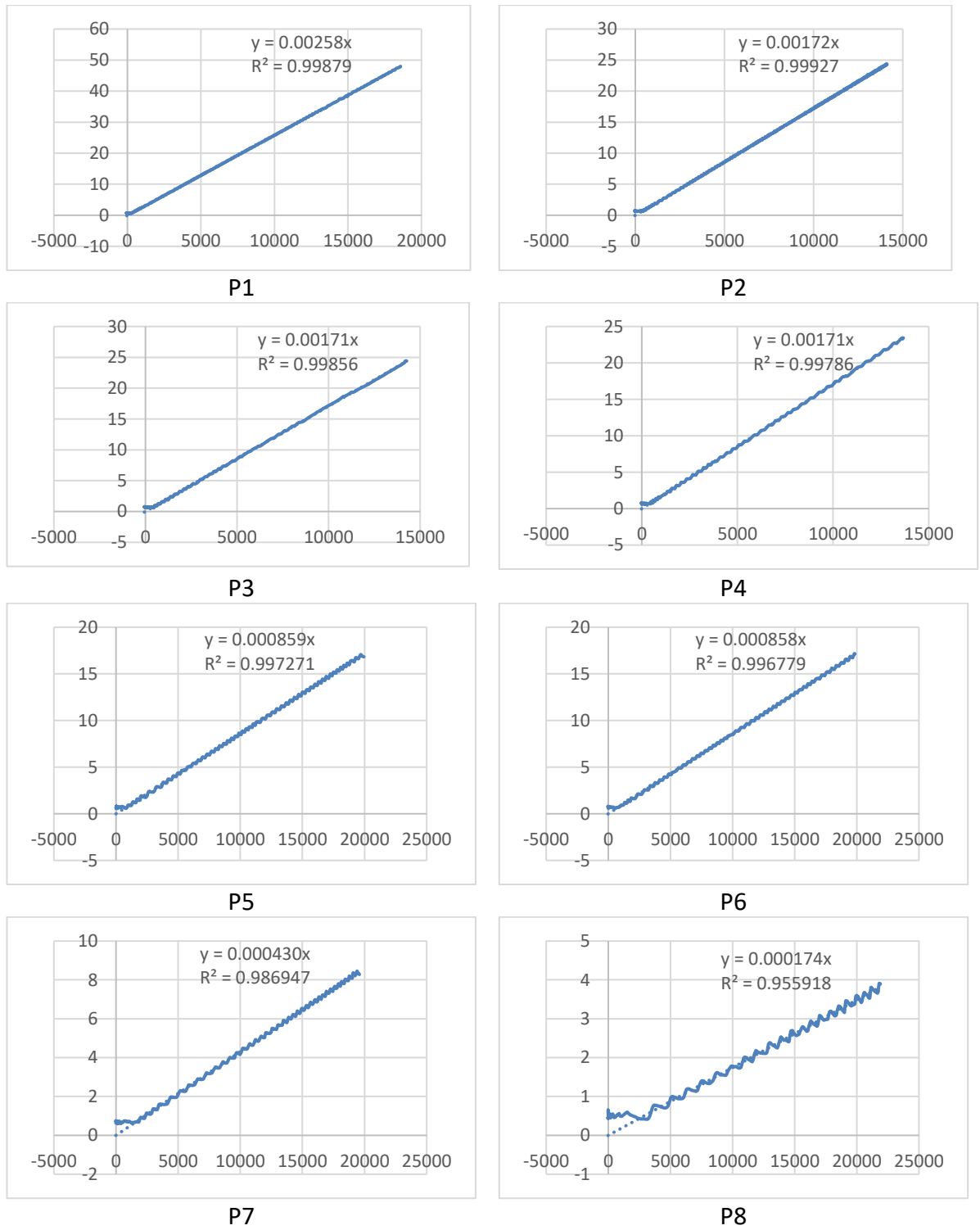


Figure 3.19 Evaluation of the control program for passive confinement

Hence, it can be concluded that the Mac^{2T} is capable of simulating passive confinement and that passive confinement was successfully applied to all the specimens (R1-R8) as expected.

Table 3.6 The predefined and the actual confining stiffness

Specimen number	Confining stiffness (k) <i>MPa/μϵ</i>	Confining stiffness from regression analysis of the testing results	Difference
P1	0.002622	0.00258	1.6%
P2	0.001748	0.00172	1.6%
P3	0.001748	0.00171	2.2%
P4	0.001748	0.00171	2.2%
P5	0.000874	0.000859	1.7%
P6	0.000874	0.000858	1.8%
P7	0.000437	0.000430	1.6%
P8	0.0001748	0.000174	0.5%

3.4.2.2 Stress-strain curves

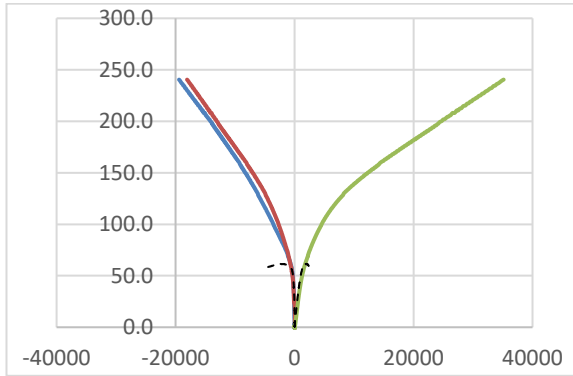
The test results in the form of stress-strain are plotted in Figure 3.20. The test results for R1 – the specimen subjected to the negligible active confinement of 0.7 MPa – are plotted in Figure 3.20 in dashed line as a benchmark. As expected, before the vertical stress (σ_z) exceeds the unconfined concrete strength, the stress-strain of all the specimens (P1-P8) almost coincides with that of R1.

As illustrated in the previous section, the scale of confining pressure is dependent on the lateral expansion. The lateral expansion is negligible until the vertical stress is close to the unconfined concrete strength when unstable cracking occurs. With small strains, passive confinement is not effectively activated. Therefore, the passive confinement can be ignored when the vertical load is small, which is the reason why the specimens (P1-P8) behaved as an unconfined specimen (R1) under vertical stress less than f_c .

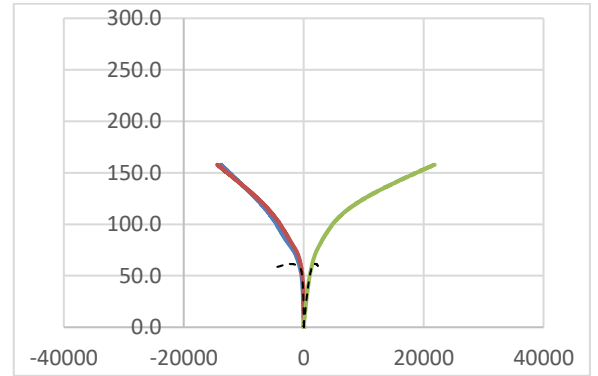
The passive confinement plays an important role after the uniaxial strength level is exceeded, and the strength reduction seen in R1 disappears in all the tests with passive confinement. The more confining stiffness the specimens were subjected to, the more confining pressure was activated at the same level of lateral expansion, and the more vertical load the specimen can withstand.

It worth highlighting that the peak strength of P8 (57 MPa) is slightly less than that of R1, possibly due to eccentricities and material variability. However, with

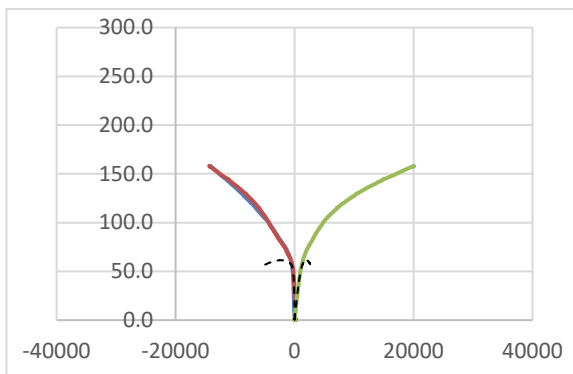
increasing lateral confinement as a result of increasing lateral expansion, vertical strength reduction can hardly be noticed in P8, even when the vertical strain was increased to more than 1%.



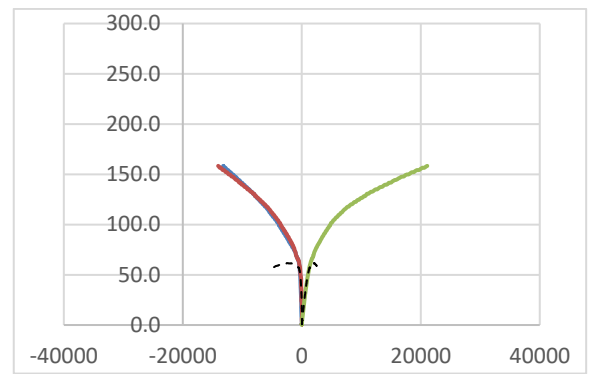
P1



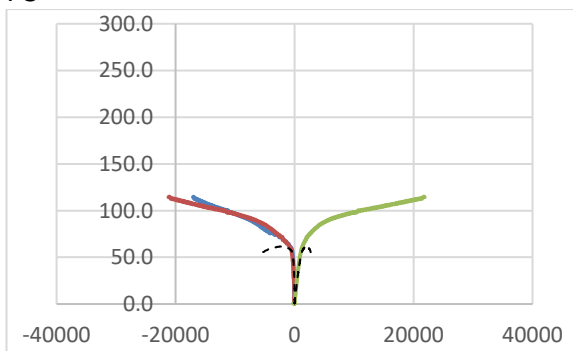
P2



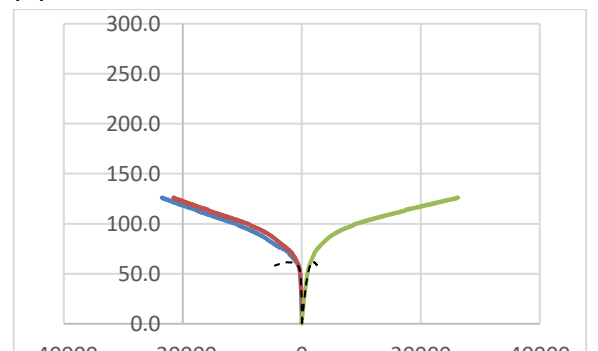
P3



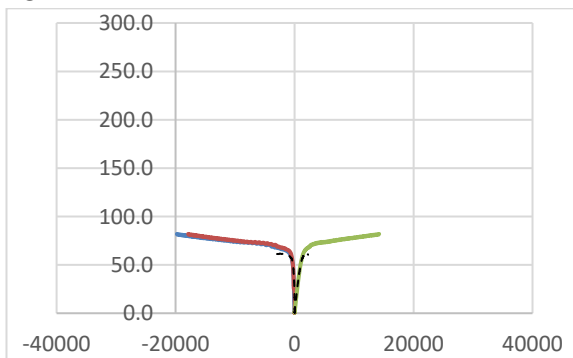
P4



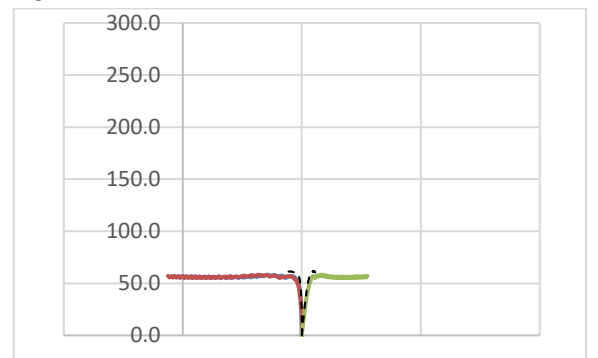
P5



P6



P7



P8



Figure 3.20 Stress-strain relations of the specimens with passive confinement

3.4.2.3 Loading path

This batch of multiaxial tests aimed to verify the hypothesis that concrete with passive confinement behaves as a perfectly plastic material under load. Therefore, the loading path of the specimen with passive confinement (P1-P8) is compared with the compressive meridian obtained from tests with active confinement in Figure 3.21.

As has been found in the previous section, passively confined specimens show similar performance as the unconfined concrete when the vertical load was no more than its unconfined strength. As a result, in the stress space specimens (P1-P8) followed the uniaxial loading path until reaching the compressive meridian.

Once the vertical stress approached the unconfined concrete strength and the stress state approached the compressive meridian, unstable cracks occurred. It follows that the passive confinement started to be activated by the significant lateral expansion due to the unstable cracks.

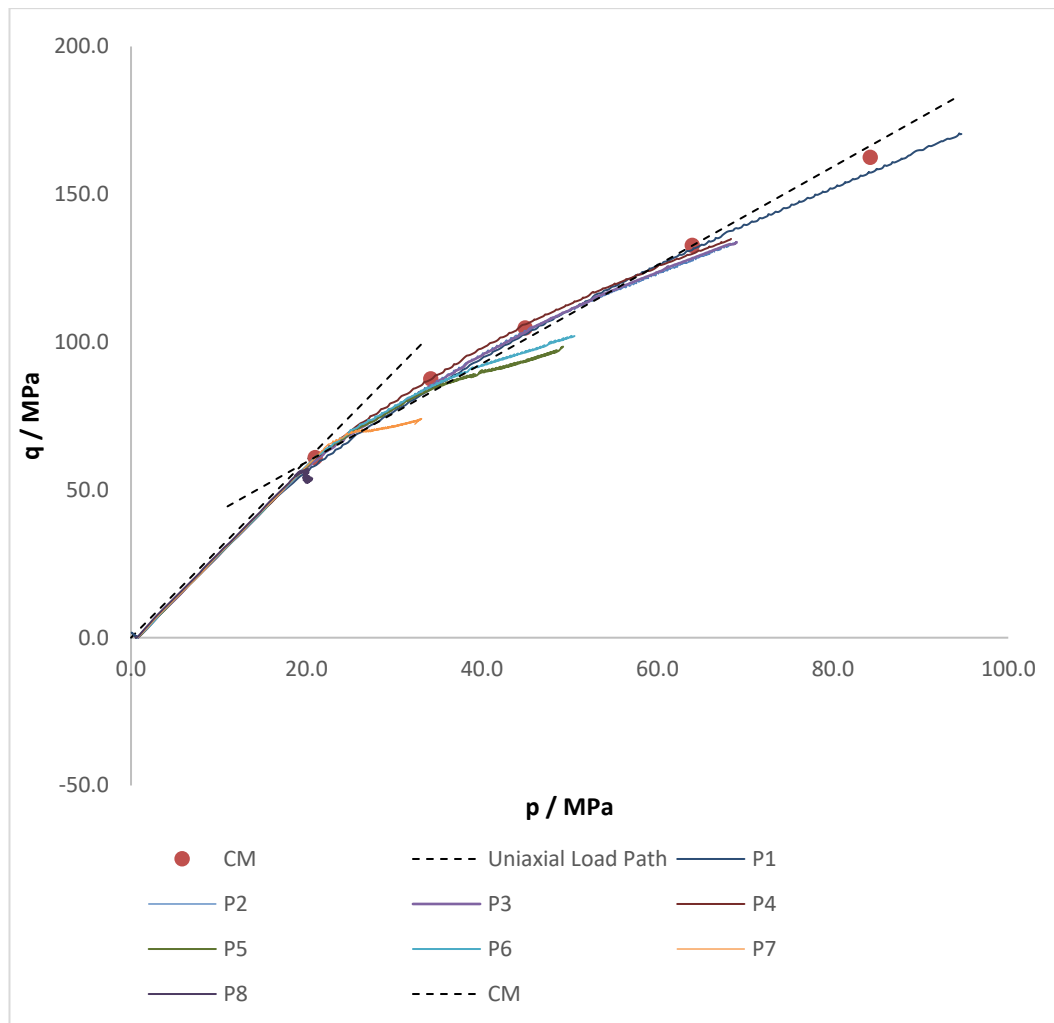


Figure 3.21 Loading path of the specimens with passive confinement

As illustrated in Figure 3.21, after having reached the compressive meridian, the stress state of all the specimens moves along the compressive meridian in the stress space. The increasing confining pressure keeps pace with the increment of the vertical load, such that the stress state stays on the failure surface. With the help of the passive confinement, the concrete simply behaves as a perfectly plastic material.

However, it seems likely that there is a limit of the perfect plasticity since the loading path deviates from the compressive meridian of the failure surface at some point. The compaction of the yielding surface indicates a reduction in concrete strength, also known as softening. Pantazopoulou & Mills (1995) proposed that the softening of concrete might be the result of lateral expansion.

An investigation was conducted to identify the effect of lateral expansion on the extent of softening. Four different levels of lateral strain were investigated: 0.8%, 1.0%, 1.2% and 1.4%, and the corresponding concrete stress states were plotted in the Figure 3.22. These stress states constitute the data points in Figure 3.22 which are grouped according to the lateral strain level. The trend line of each group is also plotted.

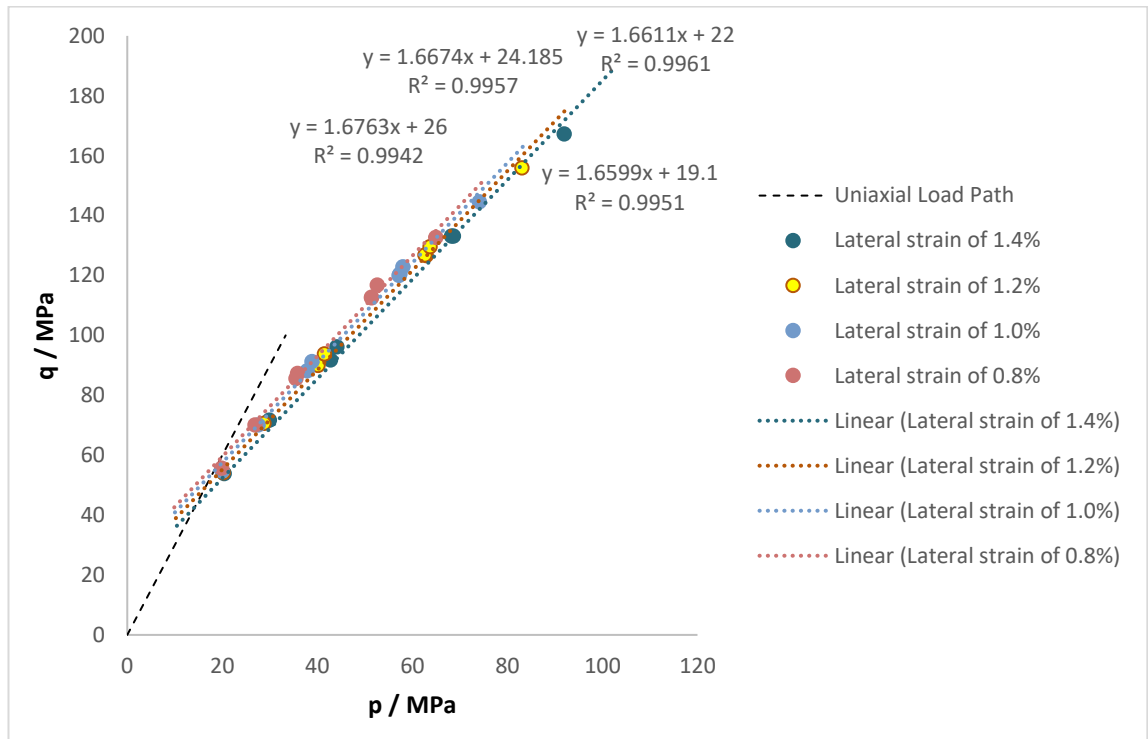


Figure 3.22 Trend lines of the stress state at same level of lateral strain

As illustrated in Figure 3.22, the trend lines fit well with the corresponding data since the parameter R-squared of each trend line is no less than 0.99. When the lateral strain is below 0.8%, the trend line of the stress states for all the specimens is almost the same as the compressive meridian of the failure surface. That is, the softening of passively confined concrete does not occur until lateral strain exceed 0.8%. The intersection of the trend line with the uniaxial loading path decrease with an increase in lateral expansion while the slope remains constant. It follows that strength reduction occurs at the sufficiently large lateral strains. In the process of softening, the compaction of the compressive meridian of the yield surface is witnessed as an isotropic pattern. This means, that the more the concrete specimens expand laterally the more their yield surface compacts.

3.4.2.4 Axial-lateral strain relationship

The dilation behaviour of passively confined concrete under load can be indicated by the ratio of the lateral and the axial strain increment, ν :

$$\nu = -\frac{\Delta\varepsilon_l}{\Delta\varepsilon_z} \quad (3.20.a)$$

As the lateral strain increments ($\Delta\varepsilon_l$) can be obtained by the average strain in the x and y directions, then

$$\nu = -\frac{\Delta\varepsilon_x + \Delta\varepsilon_y}{2 \cdot \Delta\varepsilon_z} \quad (3.20.b)$$

The parameter ν was calculated and plotted against the vertical load, as illustrated in Figure 3.23. The results of specimen R1 are also plotted as it can serve as a benchmark, the one without lateral confinement.

As can be seen, with increasing load, the dilation parameter ν of all the specimens (P1-P8) gradually increases initially. The passively confined concrete behaved as unconfined (R1) at low loads since the lateral confinement was not effectively activated. As the load approached the unconfined concrete strength (i.e. 59 MPa), unstable cracks formed, and as a result, a rapid expansion takes place sharply.

The Poisson's ratio reaches the peak when the vertical compressive stress is between 60 and 80 MPa. At this stage, the passive confinement was rapidly activated by the intensively increased lateral expansion, and controls the unstable cracking to some extent. It is worth mentioning that for those specimens with a higher level of confining stiffness, their peak dilation parameter ν is smaller.

As has been found in the previous section, the concrete behaved as a perfectly plastic material, and in stress space it moves along the failure surface once the load is larger than its unconfined strength. Mathematically, a stress state ($\sigma_1, \sigma_2, \sigma_3$) on the failure surface can be expressed as follows:

$$f(\sigma_1, \sigma_2, \sigma_3) = 0 \quad (3.21)$$

Total derivative of both sides of equation 3.21:

$$\frac{\partial f}{\partial \sigma_1} \cdot \Delta \sigma_1 + \frac{\partial f}{\partial \sigma_2} \cdot \Delta \sigma_2 + \frac{\partial f}{\partial \sigma_3} \cdot \Delta \sigma_3 = 0 \quad (3.22)$$

Where vector $(\frac{\partial f}{\partial \sigma_1}, \frac{\partial f}{\partial \sigma_2}, \frac{\partial f}{\partial \sigma_3})$ represents the normal direction of failure surface.

In this case, a cubic with passive lateral confinement under vertical load:

$$\begin{aligned} \sigma_1 &= \sigma_2 = \sigma_l \\ \sigma_3 &= \sigma_z \end{aligned} \quad (3.23)$$

Substitute Equation 3.23 into 3.22, and organise:

$$\Delta \sigma_l = \frac{-\frac{\partial f}{\partial \sigma_z}}{2 \cdot \frac{\partial f}{\partial \sigma_l}} \cdot \Delta \sigma_z \quad (3.24)$$

That is, for any increment of the vertical load $\Delta \sigma_z$, a lateral confining pressure increment ($\Delta \sigma_l$) is needed to keep the stress state on the failure surface. Substitute $\Delta \sigma_l = k \cdot \Delta \varepsilon_l$ into Equation 3.24:

$$\Delta \varepsilon_l = \frac{1}{k} \cdot \frac{-\frac{\partial f}{\partial \sigma_z}}{2 \cdot \frac{\partial f}{\partial \sigma_l}} \cdot \Delta \sigma_z \quad (3.25)$$

where k is confining stiffness.

Therefore, the lateral strain increment of a passively confined concrete depends on the confining stiffness, the shape of the failure surface and the load increment. For a specimen with a higher level of confining stiffness, the need for lateral expansion increment is lesser. This is the reason why a specimen with a higher level of confining stiffness has a smaller peak dilation parameter ν .

After having reached the peak, the dilation parameter ν gradually decreases. As has been observed in the stress space, concrete eventually exhibits softening behaviour. Therefore, at a given loading increment, the increment of vertical strain becomes relatively larger compared to the increment of lateral strain. It should be noted that the dilation parameter ν approaches 0.5 eventually.

The volumetric strain can be expressed as follows:

$$\Delta \varepsilon_v = \Delta \varepsilon_x + \Delta \varepsilon_y + \Delta \varepsilon_z \quad (3.26.a)$$

Substitute Equation 3.20 into 3.26.a, then

$$\Delta\varepsilon_v = (1 - 2\nu) \cdot \Delta\varepsilon_z \quad (3.26.b)$$

ν 's value of 0.5 indicates that the volume of the specimen remained constant. At the end of tests, the lateral confining pressure was large and thus the specimen appeared to be incompressible.

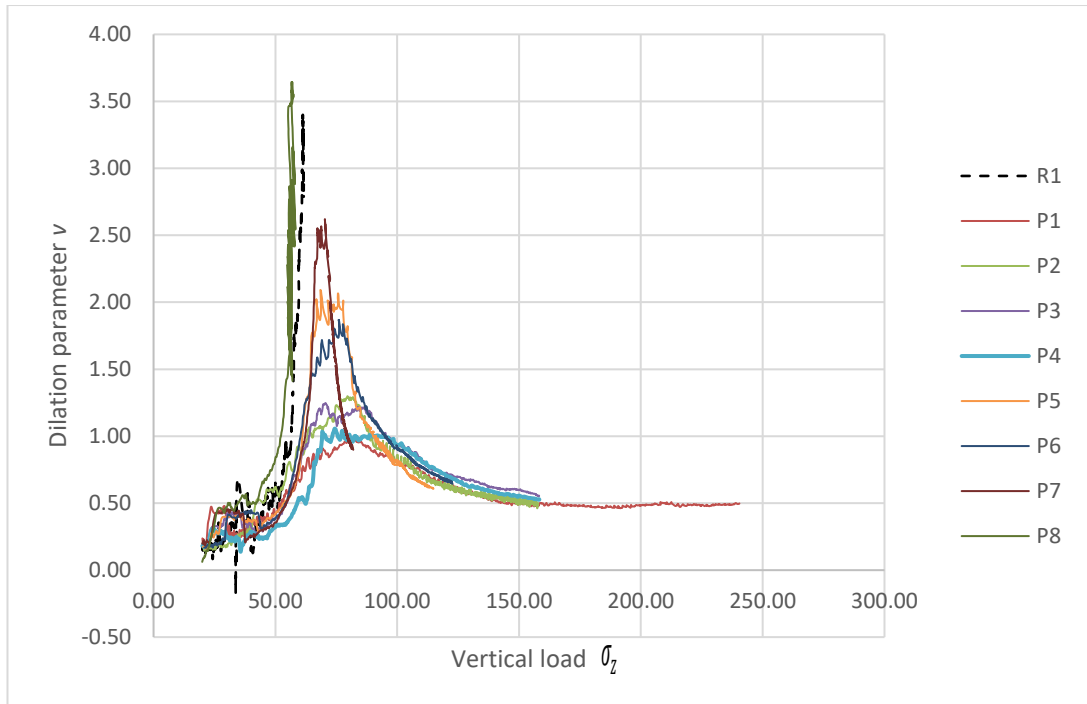


Figure 3.23 Effect of confining stiffness on dilation parameter ν history

3.4.2.5 Observational analysis of the tested specimens

Since the concrete specimen was invisible during the process of testing, observational analysis can only be conducted on tested specimens. Figure 3.24 shows a typical tested specimen P8, subjected to a lateral confining stiffness of 175 MPa (0.2 layer of CFRP). As discussed previously, the passively confined concrete behaves as unconfined concrete until compressive load approaches concrete strength. Then unstable cracks begin to form, which activates lateral confinement. Figure 3.24 illustrates the crack orientation in a typical tested specimen: the cracks form in the vertical direction. This vertical cracking indicates that the friction between the specimen and the Mac^{2t} was well controlled by the measurement of lubricated rigid platens.



Figure 3.24 A typical tested specimen with passive confinement

3.5 Summary

In this chapter, the hypothesis that under compressive load passively confined concrete behaves as perfectly plastic material was tested. Two groups of experimental tests were conducted on true tri-axial apparatus Mac^{2T}. One aimed to determine the failure surface of the concrete through conventional multiaxial tests, and the other aimed to physically simulate passive confinement. Mac^{2T} was proven capable of subjecting the concrete specimen to the confining pressure, which is dependent on its lateral expansion.

According to the results of experimental tests, the behaviour of passively confined concrete under compressive load consists of three phases. Initially, it behaves substantially as unconfined concrete, as its the relatively small lateral expansion fails to effectively activate the lateral confinement. Once the load is close to the unconfined concrete strength, unstable cracks form in the concrete and passive confinement begins to be activated. At this point, the lateral confining pressure can keep pace with the increasing load such that in the stress space concrete moves along the failure surface. Therefore, concrete exhibits the behaviour of a perfectly plastic material. However, it seems that there is a limit to this perfect plasticity. With the lateral expansion exceeding the strain of 0.008, the yielding surface in the

stress space starts to compact. As a result, in the third phase softening of the concrete occurs.

4 Modelling of conventional concrete with passive confinement

According to the observations recorded from the multiaxial tests, the behaviour of passively confined concrete under compressive load consists of three phases. Firstly, concrete under load behaved as if unconfined as the lateral confinement could not be effectively activated due to the minimal lateral expansion. When the load was close to the unconfined concrete's strength, passive confinement was activated by the lateral expansion as a result of unstable cracking. At this point, the lateral confining pressure was able to match the forces of the increasing load, such that in the stress space, concrete moved along the failure surface. Therefore, in the second phase concrete exhibited the behaviours of a perfectly plastic material. However, it has been observed that there is a limit to this perfectly plasticity. With the lateral expansion exceeding a certain level (i.e. 0.008), the yielding surface in the stress space started to compact. As a result, in the third phase softening of concrete occurred. In order to capture all of these characteristics, a plasticity-based material model for passively confined concrete is proposed in this Chapter.

A plasticity-based material model consists of three elements: failure surface, hardening rule and plastic flow rule. Details of the identification of the proposed material model are discussed in section 4.1. For the design-oriented analysis of passively confined concrete, a stress-strain curve is always of interest. Therefore, the proposed material model was simplified and this is expressed in incremental form in section 4.2. Following this, the stress-strain curve of passively confined concrete under compressive load is presented as produced in MATLAB. In section 4.3, the proposed material model is introduced into nonlinear finite element software ABAQUS, in order to analyse passively confined concrete structural components with complicated boundary condition.

4.1 Plasticity-based constitutive model for passively confined concrete

In this section, a plasticity-based constitutive model is proposed to capture the mechanical behaviour of passively confined concrete, which consists of the

identification of the yield surface, the hardening rule, and the plastic flow potential. The yield surface function was first proposed by Lee & Fenves (1998), the parameters of which were identified based on the results of multiaxial tests conducted using Mac^{2t}. The hardening rule was defined to capture the response of passively confined concrete under compressive load: it behaves as a perfectly plastic material at first and eventually exhibits softening. The plastic flow potential is a surface function in the stress space, and the normal surface vector represents the direction of plastic principal strain increment vector. According to the observations made from multiaxial tests, the plastic potential function is affected by the confining stiffness and the confining pressure applied to concrete.

4.1.1 Yield surface

Lee and Fenves (1998) proposed the function of the yield surface to be used, expressed as follows:

$$f(\sigma_{ij}) = \frac{1}{1-\alpha} \cdot (q - 3\alpha p + \beta \langle \sigma_{max} \rangle - \gamma \langle -\sigma_{max} \rangle) \quad (4.1)$$

$$\beta = \frac{\sigma_c}{\sigma_t} (\alpha - 1) - (1 + \alpha)$$

where the stress state σ_{ij} is in the form of p , q and σ_{max} , which represent the hydrostatic pressure, the Mises stress and the maximum principal stress respectively:

$$p = -\frac{1}{3} \cdot (\sigma_1 + \sigma_2 + \sigma_3)$$

$$q = \sqrt{\frac{1}{2} [(\sigma_1 - \sigma_2)^2 + (\sigma_2 - \sigma_3)^2 + (\sigma_3 - \sigma_1)^2]}$$

The parameter α and γ in the function are the constants which control the shape of the yield surface in the stress space. σ_c and σ_t are the hardening parameters that control both the size and the shape of the yield surface and vary with the development of the plasticity.

$\langle \rangle$ is a mathematical operator:

$$\langle a \rangle = \begin{cases} a, & a \geq 0 \\ 0, & a < 0 \end{cases}$$

Therefore, for the cases where all the principal stresses are in compression such as the following:

$$0 \geq \sigma_{max} = \sigma_1 \geq \sigma_2 \geq \sigma_3$$

then the yield surface function Equation (4.1) can be simplified to:

$$f(\sigma_{ij}) = \frac{1}{1 - \alpha} \cdot (q - 3\alpha p + \gamma \sigma_{max} - \sigma_c) \quad (4.2)$$

The compressive meridian and the tensile meridian constitute the intersecting curve of the yield surface and the plane surface: $\sigma_2 - \sigma_3 = 0$. The compressive meridian is the set of the stress states on the intersecting curve that meets the condition:

$$\sigma_1 = \sigma_2 \geq \sigma_3 \quad (4.3)$$

The compressive meridian can then be calculated using simultaneous Equations (4.2) and (4.3), and can be expressed as follows:

$$\left(\frac{1}{3}\gamma + 1\right)q - (\gamma + 3\alpha)p = (1 - \alpha)\sigma_c \quad (4.4)$$

Similarly, the tensile meridian is the set of the stress states on the intersecting curve that meets the condition:

$$\sigma_1 \geq \sigma_2 = \sigma_3 \quad (4.5)$$

The tensile meridian can then be calculated using simultaneous Equations (4.2) and (4.5), and can be expressed as follows:

$$\left(\frac{2}{3}\gamma + 1\right)q - (\gamma + 3\alpha)p = (1 - \alpha)\sigma_c \quad (4.6)$$

γ is the parameter that controls the shape of the yield surface in the π plane, which is a surface perpendicular to the hydrostatic axis. According to multiaxial tests conducted in the past, a γ equal to 3 can be received for typical concrete (Lubliner et al., 1989).

By substituting $\gamma = 3$ into Equation (4.4), the compressive meridian for $0 \geq \sigma_{max}$ can be expressed as:

$$2q - 3(1 + \alpha)p = (1 - \alpha)\sigma_c \quad (4.7)$$

In the compression tests of concrete with constant active confinement, the peak load that the concrete specimen sustained indicates a stress state on the failure

surface. By curve fitting the corresponding data points, a compressive meridian of the failure surface was obtained in the previous section, expressed as follows:

$$q = 1.67 \cdot p + 26.1 \quad (4.8)$$

By comparing the coefficients of Equations (4.7) and (4.8), the parameter α was calculated as equal to 0.1145. The compressive meridian and the tensile meridian are plotted in the p-q coordinate, as is shown in Figure 4.1. Apart from the meridians, the uniaxial compressive and the uniaxial tensile loading paths are also plotted. The intersecting point of the compressive meridian and the uniaxial compressive loading path represent the stress state $(0,0,\sigma_c)$, and as mentioned previously, σ_c is the hardening parameter of the yield surface. Similarly, the other hardening parameter σ_t constitutes the stress state $(\sigma_t,0,0)$, the intersecting point of the tensile meridian and the uniaxial tensile loading path.

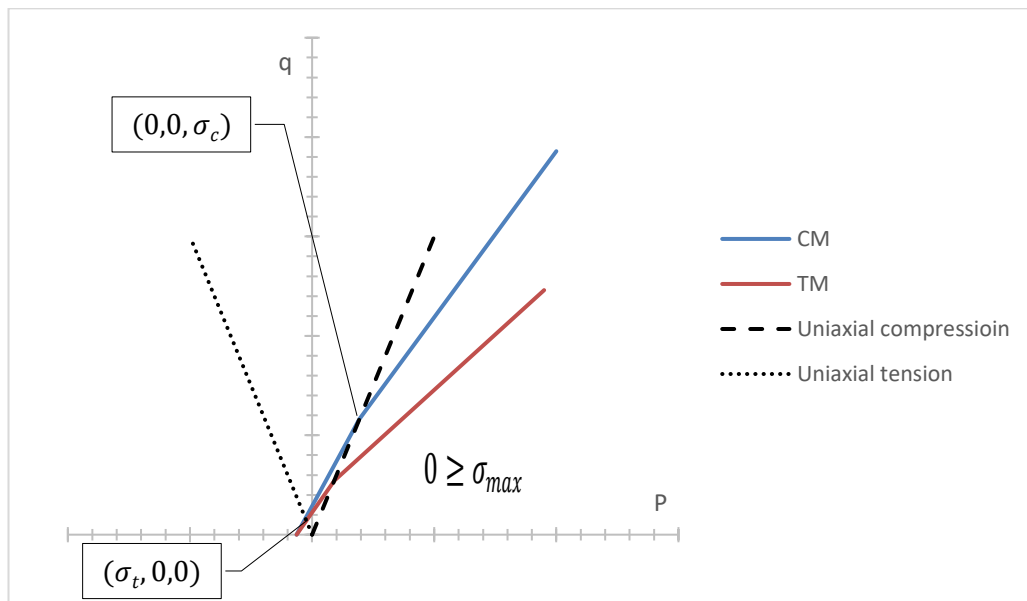


Figure 4.1 The compressive and the tensile meridian of the yield surface

The yield surface is characterised by its two different hardening parameters. Because of the two hardening parameters, the concrete character of different strength in compression and tension can be captured. For the cases where all the principal stresses are in compression, the yield surface can be expressed by Equation (4.2). Under this circumstance, σ_c is the only hardening parameter which controls the yield surface evolution.

4.1.2 Hardening rule of passively confined concrete

A typical loading path of passively confined concrete (specimen P5) is plotted in Figure 4.2 and is compared with the uniaxial loading path and the compressive meridian of the failure surface. The response of passively confined concrete under compressive loading consists of three phases:

1. Following the uniaxial loading path.
2. Moving along the compressive meridian as a perfectly plastic material.
3. Softening as a result of significant lateral expansion.

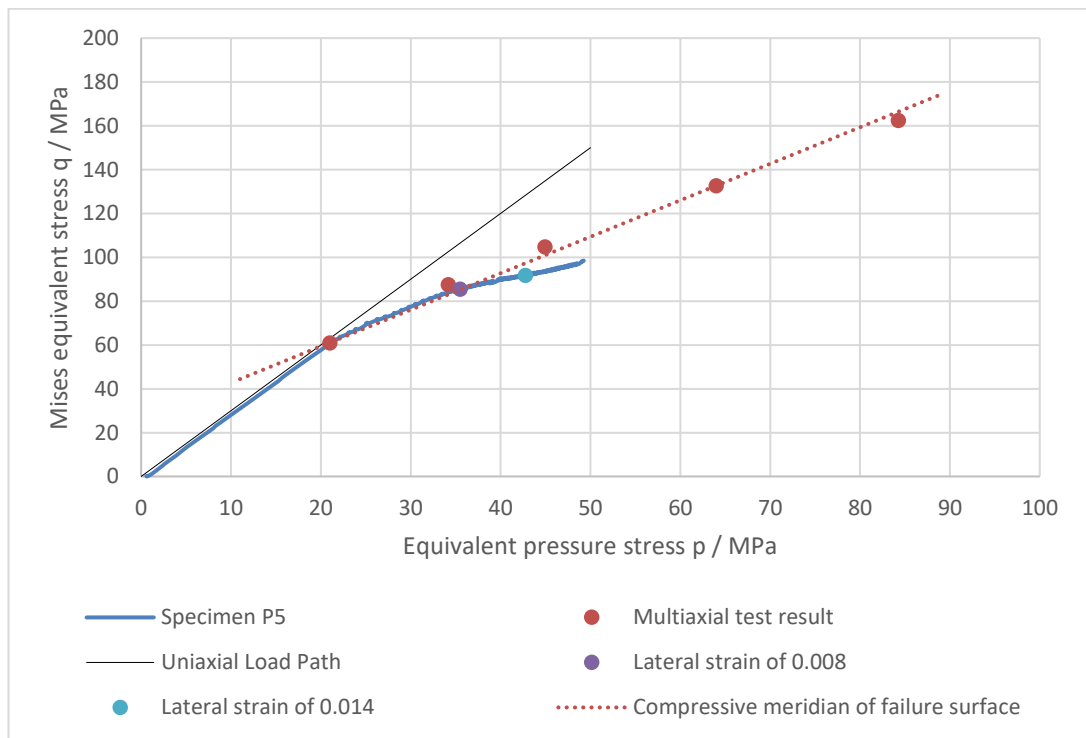


Figure 4.2 Loading path of a passively confined concrete under load

According to Figure 4.2, in the first phase, the compressive pressure applied to concrete was less than its unconfined strength, and the lateral expansion was so small that passive confinement could not be effectively activated. At this stage, concrete behaved as unconfined concrete. This is followed by the second phase when the load exceeded the concrete's unconfined strength. At this stage unstable cracking formed, which generated considerable lateral expansion and effectively activated the passive confinement. The increasing confining pressure kept pace with

the load increment, such that the concrete moved along the failure surface as a perfectly plastic material.

To capture the response of passively confined concrete in the first two phases, the hardening parameter σ_c was defined as a function with respect to the equivalent plastic strain (ε_c^{pl}), which represents the permanent deformation in the compressive loading direction and can be calculated by the time integral of the minimum eigenvalue of the plastic strain rate tensor (ε_{min}^{pl}):

$$\varepsilon_c^{pl} = - \int_0^t \varepsilon_{min}^{pl} dt \quad (4.9)$$

For the cases of passively confined concrete under compressive load, ε_{min}^{pl} is the plastic strain rate in the loading direction.

As illustrated in Figure 4.3, a bilinear relation between the hardening parameter σ_c and the equivalent plastic strain ε_c^{pl} was defined to represent the concrete's response in the first two stages: plastic hardening in the first phase and perfect-plasticity in the second phase. The function of σ_c with respect to ε_c^{pl} is expressed as follows:

$$\sigma_c = \begin{cases} \frac{0.3f'_c}{\varepsilon_{cp1}} \varepsilon_c^{pl} + 0.7 \cdot f'_c, & \varepsilon_c^{pl} < \varepsilon_{cp1} \\ f'_c, & \varepsilon_c^{pl} \geq \varepsilon_{cp1} \end{cases} \quad (4.10)$$

Initial yielding ($\varepsilon_c^{pl} = 0$) occurred once the stress state of concrete satisfied the following:

$$\{(\sigma_{ij}) | f(\sigma_{ij}, \sigma_c) = 0, \sigma_c = 0.7 \cdot f'_c\}$$

where f'_c represents the concrete uniaxial compressive strength.

Following this, the equivalent ε_c^{pl} accumulated as the result of plastic loading, and the hardening parameter σ_c increased with the accumulation of ε_c^{pl} until it was equal to f'_c . Then the concrete behaved as a perfectly plastic material and hardening parameter σ_c was constant after the onset of perfectly plasticity when

the equivalent ε_c^{pl} was equal to ε_{cp1} . Parameter ε_{cp1} corresponds to the plastic strain of concrete under the peak uniaxial compressive load:

$$\varepsilon_{cp1} = \varepsilon_{c1} - \frac{f'_c}{E_c} \quad (4.11)$$

where ε_{c1} is the strain at which concrete sustains the peak uniaxial compressive stress.

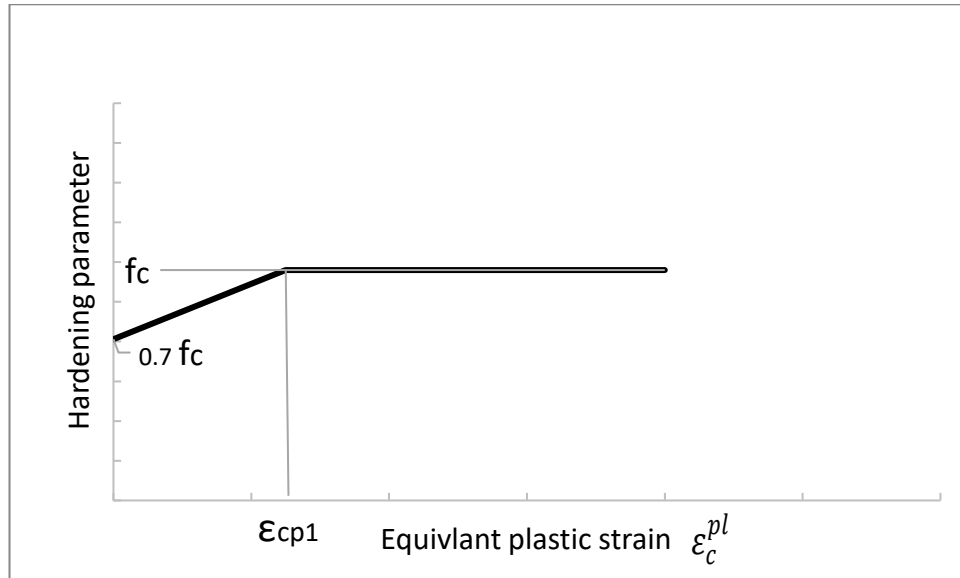


Figure 4.3 Relation between hardening parameter σ_c and hardening variable ε_c^{pl}

However, there is a limit to the perfect-plasticity of passively confined concrete. As illustrated in Figure 4.2, there are two points marked in the loading path of specimen P5 which represent the stress states at the lateral strain (ε_l) of 0.008 and 0.014, respectively. Obviously, the data point corresponding to $\varepsilon_l = 0.008$ was on the failure surface, while the other ($\varepsilon_l = 0.014$) was located within the failure surface. It follows that passively confined concrete exhibited softening behaviour once its lateral strain exceeded 0.008.

Apart from that conducted on specimen P5, there were another six experimental tests conducted on passively confined concrete. The stress states of all these tests at certain levels of lateral strain were collected and the corresponding data points plotted in Figure 4.4. The data points were grouped regarding the corresponding lateral strain, and the trend lines plotted for each group. These represent the compressive meridian of the yield surface. As can be seen, with the increase of

lateral expansion of concrete, the yield surface compacted in an isotropic manner, since all the four trend lines in Figure 4.4 which represent the compressive meridian of yield surface have a similar slope.

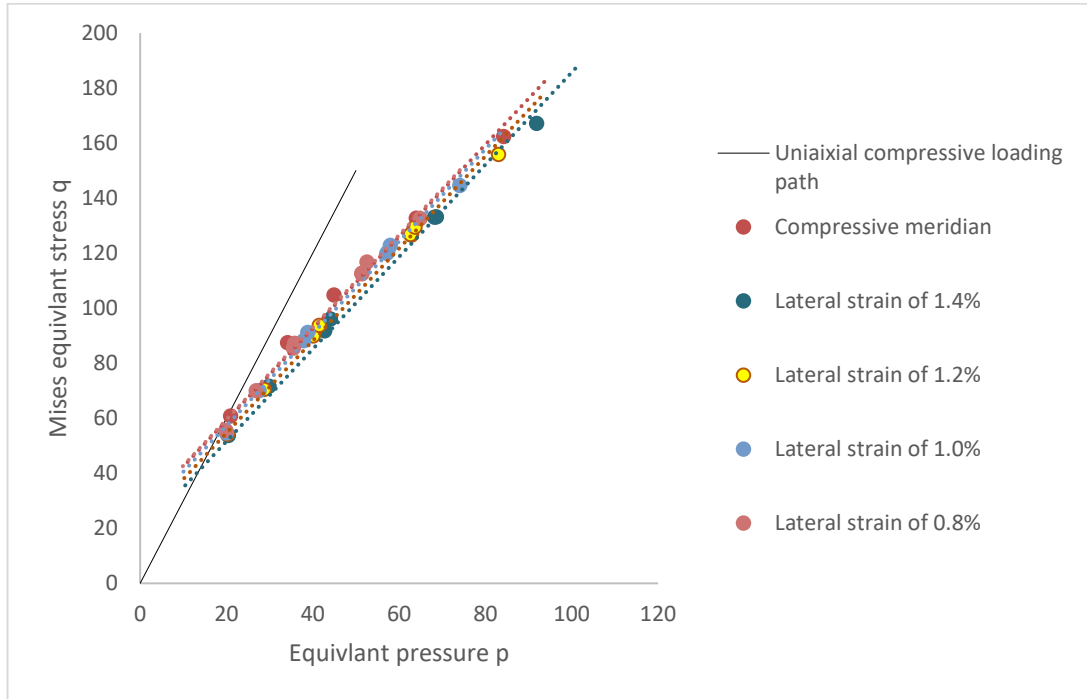


Figure 4.4 Trend lines of the stress state at the same level of lateral strain

A parameter $d = \sigma_c / f'_c$ was introduced to consider the impairment of hardening parameter σ_c by lateral strain ε_l , which is plotted against ε_l in Figure 4.5. Mathematically, the relationship between d and ε_l can be expressed as follows:

$$d(\varepsilon_l) = \begin{cases} 1, & \varepsilon_l < 0.008 \\ -50.8 \cdot \varepsilon_l + 1.414, & \varepsilon_l \geq 0.008 \end{cases} \quad (4.12)$$

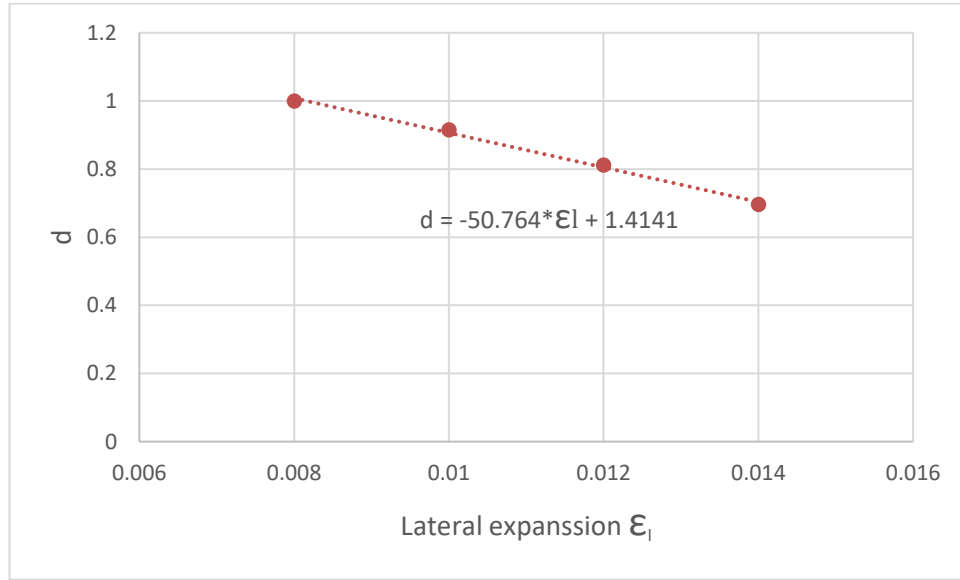


Figure 4.5 Relation between the parameter d and the hardening variable ϵ_l

In summary, the hardening parameter σ_c is a function of ϵ_c^{pl} and ϵ_l which can be expressed as follows:

$$\sigma_c = \begin{cases} \left(\frac{0.3f'_c}{\epsilon_{cp1}} \epsilon_c^{pl} + 0.7f'_c \right) \cdot d(\epsilon_l), & \epsilon_c^{pl} < \epsilon_{cp1} \\ f'_c \cdot d(\epsilon_l), & \epsilon_c^{pl} \geq \epsilon_{cp1} \end{cases} \quad (4.13)$$

4.1.3 Plastic flow potential

The Drucker–Prager function was used as the plastic flow potential:

$$g(p, q) = q - \tan\phi \cdot p \quad (4.14)$$

According to plastic theory, the plastic strain increment $d\epsilon_{ij}^p$ is determined by plastic flow rule as follows:

$$d\epsilon_{ij}^p = d\lambda \cdot \frac{\partial g}{\partial \sigma_{ij}} \quad (4.15)$$

substitute Equation (4.14) into Equation (4.15):

$$d\epsilon_{ij}^p = d\lambda \cdot \left(\frac{\tan\phi}{3} \delta_{ij} + \frac{\sqrt{3}}{2} \frac{1}{\sqrt{J_2}} S_{ij} \right) \quad (4.16)$$

for the cases where $\sigma_2 = \sigma_3$; $\epsilon_2 = \epsilon_3$:

$$d\epsilon_1^p = d\lambda \cdot \left(\frac{\tan\phi}{3} - 1 \right) \quad (4.17.a)$$

$$d\varepsilon_2^p = d\lambda \cdot \left(\frac{\tan\varphi}{3} + \frac{1}{2} \right) \quad (4.17.b)$$

so:

$$\frac{d\varepsilon_1^p + 2 \cdot d\varepsilon_2^p}{d\varepsilon_2^p - d\varepsilon_1^p} = \frac{d\lambda \cdot (\tan\varphi)}{d\lambda \cdot \left(\frac{3}{2} \right)} = \frac{2}{3} \tan\varphi$$

which is equivalent to:

$$\tan\varphi = \frac{3}{2} \cdot \frac{d\varepsilon_1^p + 2 \cdot d\varepsilon_2^p}{d\varepsilon_2^p - d\varepsilon_1^p} \quad (4.18)$$

Therefore, dilation angle φ , the only parameter in the plastic flow potential, can be determined by the ratio of the lateral and the axial plastic strain increment, as follow:

$$\varphi\left(-\frac{d\varepsilon_2^p}{d\varepsilon_1^p}\right) = \tan^{-1}\left(\frac{3}{2} \cdot \frac{2 \cdot \left(-\frac{d\varepsilon_2^p}{d\varepsilon_1^p}\right) - 1}{\left(-\frac{d\varepsilon_2^p}{d\varepsilon_1^p}\right) + 1}\right) \quad (4.19)$$

As illustrated in Figure 4.6, the dilation angle φ is plotted against plastic strain ratio $-d\varepsilon_2^p/d\varepsilon_1^p$, according to Equation (4.19). Obviously, φ is an injective function with respect to $-d\varepsilon_2^p/d\varepsilon_1^p$, over the domain of (0,3). Hence, the dilation angle φ represents the scale of plastic strain incremental ratio.

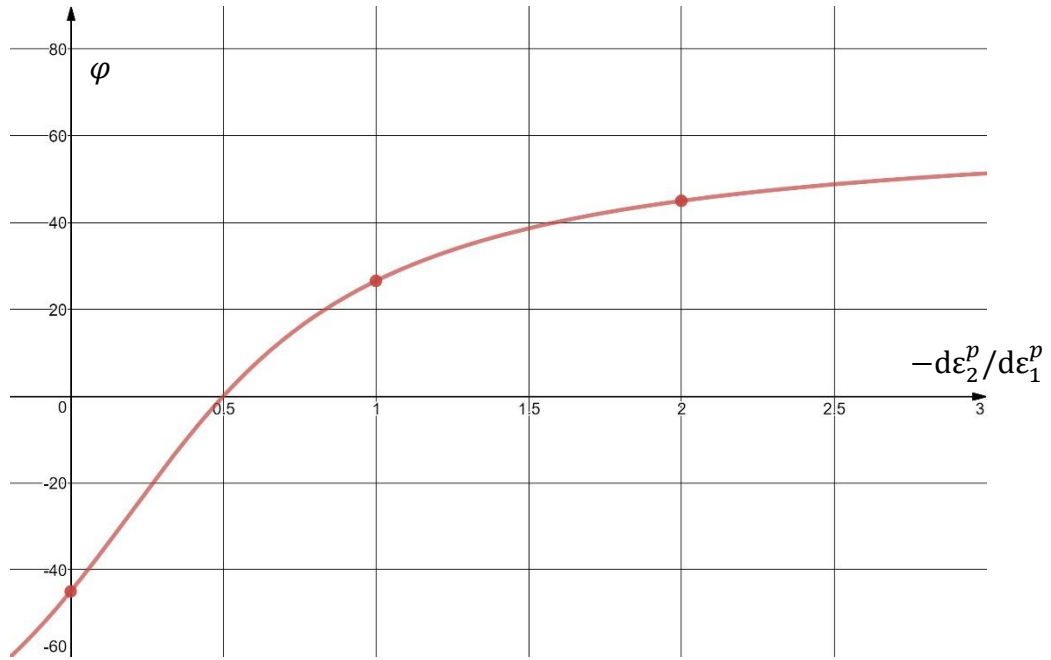


Figure 4.6 The curve of function $\varphi(-\frac{d\epsilon_2^p}{d\epsilon_1^p})$

The parameter identification of the plastic flow rule requires the plastic strain history from experimental tests. However, the plastic strain tensor cannot be directly read using Mac^{2t} during the experimental tests on passively confined concrete. Instead, the only field variables monitored in the process of testing were principal stresses and strains. Therefore, the plastic strain had to be transferred using the test reading of total principal stress and strain.

The total strain can be decomposed as follows:

$$\epsilon_{ij} = \epsilon_{ij}^e + \epsilon_{ij}^p \quad (4.20)$$

According to Hook's Law, the elastic strain is:

$$\epsilon_{ij}^e = C_{ijkl}^{-1} \cdot \sigma_{kl} \quad (4.21)$$

where C_{ijkl} can be determined by material elastic constants Young's modulus and Poisson's ratio.

Then the plastic strain tensor can be determined as follows:

$$\epsilon_{ij}^p = \epsilon_{ij} - C_{ijkl}^{-1} \cdot \sigma_{ij} \quad (4.22)$$

In the cases where $\sigma_2 = \sigma_3$ and $\varepsilon_2 = \varepsilon_3$

$$\varepsilon_1^p = \varepsilon_1 - \frac{1}{E}(\sigma_1 - 2\nu\sigma_2) \quad (4.23.a)$$

$$\varepsilon_2^p = \varepsilon_2 - \frac{1}{E}[(1 - \nu)\sigma_2 - \nu\sigma_1] \quad (4.23.b)$$

Therefore, the plastic strain increment ratio ($-\mathrm{d}\varepsilon_2^p/\mathrm{d}\varepsilon_1^p$) in the testing process can be calculated. $-\mathrm{d}\varepsilon_2^p/\mathrm{d}\varepsilon_1^p$ of a typical test on passively confined concrete, P1, is plotted against lateral confining pressure in Figure 4.7. When the confining pressure was small, $-\mathrm{d}\varepsilon_2^p/\mathrm{d}\varepsilon_1^p$ was relatively large. This can be explained by the unstable cracking as a result of increasing compressive loading. That is, the expansion in the lateral direction was much larger than the deformation in the vertical direction. With the increasing lateral confining pressure, the unstable cracking was minimised and the lateral plastic strain became smaller; as a result, $-\mathrm{d}\varepsilon_2^p/\mathrm{d}\varepsilon_1^p$ gradually reduced. It is worth mentioning that $-\mathrm{d}\varepsilon_2^p/\mathrm{d}\varepsilon_1^p$ fluctuated around 0.5 at $|\sigma_l|$ exceeding 20 MPa. The $-\mathrm{d}\varepsilon_2^p/\mathrm{d}\varepsilon_1^p$ of 0.5 indicates no plastic volume change.

The curve of $-\mathrm{d}\varepsilon_2^p/\mathrm{d}\varepsilon_1^p$ and σ_l can be fit by a broken line, which is represented by a dashed line in Figure 4.7. Due to the 1:1 mapping ratio between φ and $-\mathrm{d}\varepsilon_2^p/\mathrm{d}\varepsilon_1^p$, the function $\varphi(\sigma_l)$ can also be expressed in the form of a broken line.

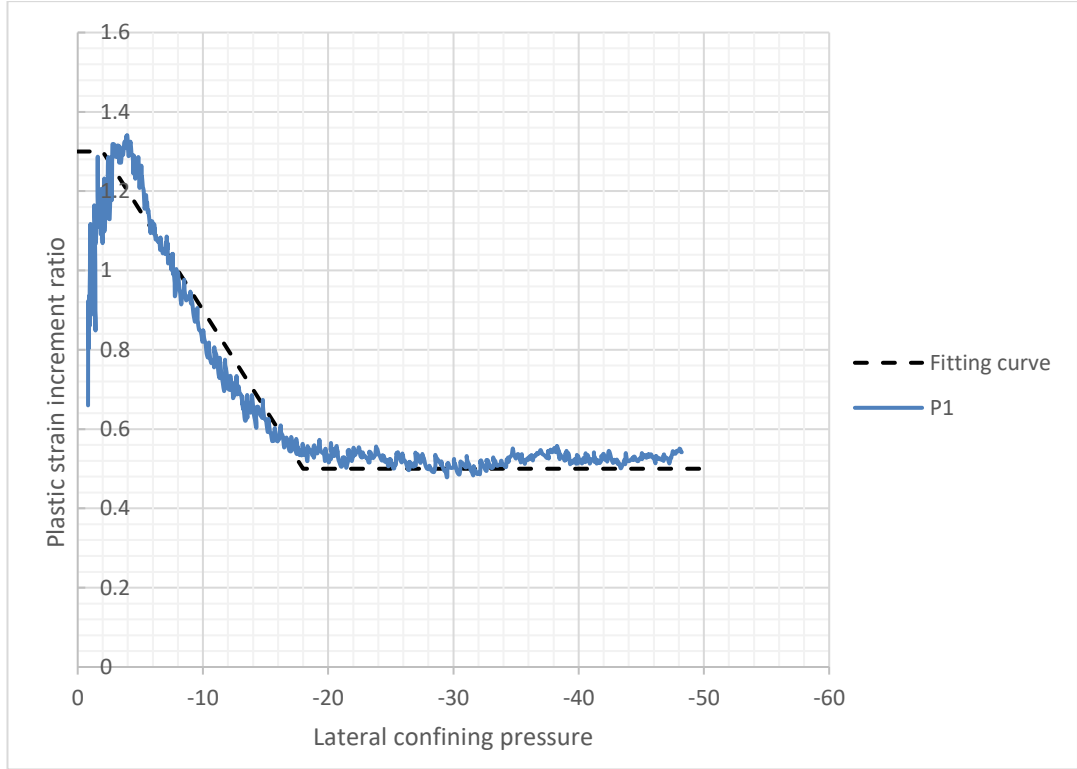


Figure 4.7 The history of plastic strain increment ratio ($-\mathbf{d}\varepsilon_2^p/\mathbf{d}\varepsilon_1^p$) of P1

Apart from σ_l , the confining stiffness ($k = -d\sigma_l/d\varepsilon_l$) is the other variable that affects the dilation angle φ . The $\sigma_l - \varphi$ curves of the experimental tests (P1, P4, P6 and P7) with different levels of confining stiffness are plotted in Figure 4.8. A broken line function (dashed line in Figure 4.8) was introduced to fit the curves, which is mathematically expressed as follows:

$$\varphi = \begin{cases} \varphi_1 & \sigma_l \geq -2 \\ \frac{\varphi_1 + 18}{16} \cdot (\sigma_l + 18) - 18 & -2 > \sigma_l \geq -18 \\ 2 & -18 > \sigma_l \end{cases} \quad (4.24)$$

where φ_1 represents the initial value of the dilation angle, which is a parametric function with respect to the confining stiffness k applied to the concrete. The relationship between φ_1 and k was obtained from experimental test results, as illustrated in Figure 4.9. The interpolation of φ_1 can be implemented for the k at other values.

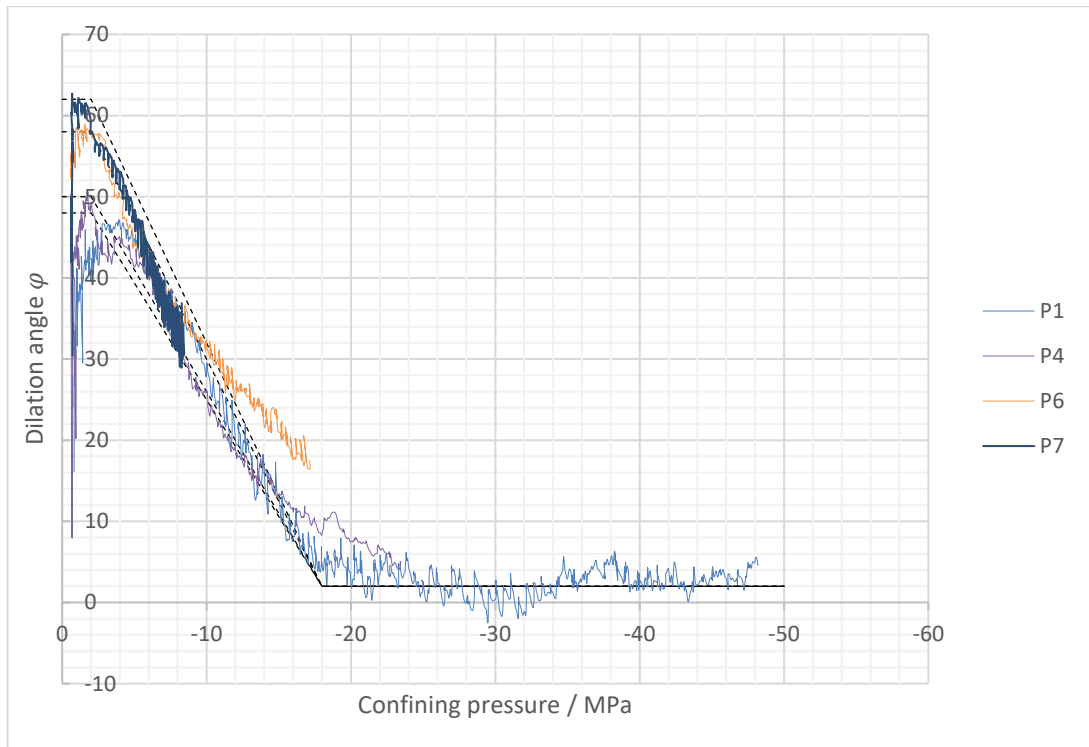


Figure 4.8 History of dilation angle of multiaxial tests

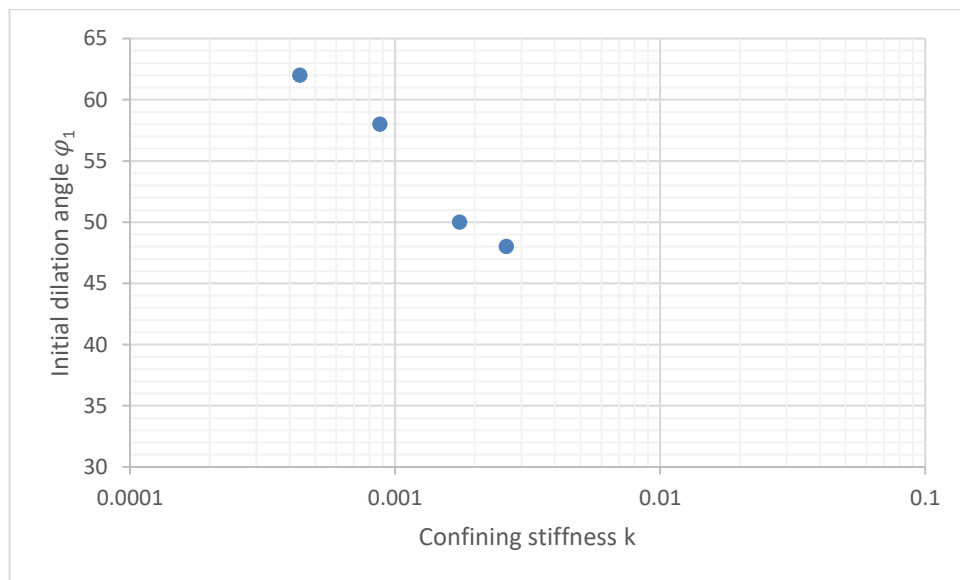


Figure 4.9 Initial dilation angle φ_1 at different levels of confining stiffness

4.2 Analytical simulation through MATLAB

The plasticity-based material model proposed in section 4.1 is too complicated for the design-oriented analysis of passively confined concrete structural components where a stress-strain curve is always of interest. In order to facilitate the design-oriented analysis, a MATLAB program was developed to produce the stress-strain curve of passively confined concrete under compressive load and is described in this section.

The hardening rule in the proposed material model was simplified. In other words, passively confined concrete was assumed to behave as a perfectly plastic material. Moreover, the failure surface and the plastic flow rule were maintained as defined in the previous section. The perfectly plastic-based constitutive model could then be expressed by a matrix equation in an incremental form, i.e. $\{d\sigma\} = [C]^{ep} \cdot \{d\varepsilon\}$. Apart from the material equation, there is a linear relation between the lateral expansion of passively confined concrete and the confining pressure applied to concrete (i.e. $\sigma_l = k \cdot \varepsilon_l$), which is deemed as the complementary condition.

The stress-strain curve of passively confined concrete under compression was then generated through a MATLAB program by uniting the material matrix equation and the complementary condition. Since the parameter of the plastic potential equation, the dilation angle, varies with respect to the field variables, the matrix $[C]^{ep}$ is not constant. Therefore, an iterative stepwise algorithm was needed for the program to incorporate the material matrix equation and the complementary equation.

The derivation of the incremental material equation is firstly reviewed in this section, followed by a description of the algorithm of the MATLAB program. Numerical results of the MATLAB program are evaluated by comparing them to the experimental tests results.

4.2.1 Incremental form of perfectly-plastic based constitutive model

The general form of the incremental model is expressed as follow:

$$d\sigma_{ij} = C_{ijkl}^{ep} \cdot d\varepsilon_{kl} \quad (4.25)$$

Based on the plasticity theory, the strain increment consists of the elastic and the plastic components:

$$d\varepsilon_{ij} = d\varepsilon_{ij}^e + d\varepsilon_{ij}^p \quad (4.26)$$

The incremental stress vector is equal to the elastic strain increment multiplied by a fourth order tensor due to the Hooke's Law:

$$d\sigma_{ij} = C_{ijkl} \cdot d\varepsilon_{ij}^e \quad (4.27)$$

$$C_{ijkl} = 2G(\delta_{ik}\delta_{jl} + \frac{\nu}{1-2\nu}\delta_{ij}\delta_{kl}) \quad (4.28)$$

where

G is the shear moduli of concrete,

ν is the Poisson ratio, and

δ_{ij} is Kronecker's delta.

The direction of the stress increment vector is tangential to the failure surface $f(\sigma_{ij}) = 0$, known as the consistency condition for perfectly plastic material:

$$\frac{\partial f}{\partial \sigma_{ij}} \cdot d\sigma_{ij} = 0 \quad (4.29)$$

By substituting Equations (4.26) and (4.27) into Equation (4.29), then:

$$\frac{\partial f}{\partial \sigma_{ij}} \cdot C_{ijkl} \cdot d\varepsilon_{kl} - \frac{\partial f}{\partial \sigma_{ij}} \cdot C_{ijkl} \cdot d\varepsilon_{kl}^p = 0 \quad (4.30)$$

According to the theory of plasticity, the plastic strain increment is calculated as the product of a scale $d\lambda$ and a partial differential vector $\frac{\partial g}{\partial \sigma_{ij}}$,

$$d\varepsilon_{ij}^p = d\lambda \cdot \frac{\partial g}{\partial \sigma_{ij}} \quad (4.31)$$

where $g(\sigma_{ij}) = 0$ is the plastic potential function.

By substituting Equation (4.31) into Equation (4.30):

$$\frac{\partial f}{\partial \sigma_{ij}} \cdot C_{ijkl} \cdot d\varepsilon_{kl} - \frac{\partial f}{\partial \sigma_{ij}} \cdot C_{ijkl} \cdot d\lambda \cdot \frac{\partial g}{\partial \sigma_{kl}} = 0 \quad (4.32)$$

After having organised equation, $d\lambda$ can be expressed by:

$$d\lambda = \frac{1}{H} \cdot \frac{\partial f}{\partial \sigma_{ij}} \cdot C_{ijkl} \cdot d\varepsilon_{kl} \quad (4.33)$$

where $H = \frac{\partial f}{\partial \sigma_{ij}} C_{ijkl} \frac{\partial g}{\partial \sigma_{kl}}$.

By substituting Equation (4.33) into Equation (4.31):

$$d\varepsilon_{kl}^p = \frac{1}{H} \cdot \frac{\partial f}{\partial \sigma_{ij}} \cdot C_{ijkl} \cdot \frac{\partial g}{\partial \sigma_{kl}} \cdot d\varepsilon_{kl} \quad (4.34)$$

Equation (4.27) can be expressed:

$$d\sigma_{ij} = C_{ijkl} \cdot d\varepsilon_{kl} - C_{ijkl} \cdot d\varepsilon_{ij}^p \quad (4.35)$$

By substituting Equation (4.34) into Equation (4.35):

$$d\sigma_{ij} = C_{ijkl} \cdot d\varepsilon_{kl} - \frac{1}{H} \cdot \frac{\partial f}{\partial \sigma_{ij}} \cdot C_{ijkl} \cdot C_{ijkl} \cdot \frac{\partial g}{\partial \sigma_{kl}} \cdot d\varepsilon_{kl} \quad (4.36)$$

which can be organised as follows:

$$d\sigma_{ij} = (C_{ijkl} - \frac{1}{H} H_{ij}^* H_{kl}) \cdot d\varepsilon_{kl} \quad (4.37)$$

Therefore, C_{ijkl}^{ep} in Equation (4.25) can be expressed by:

$$C_{ijkl}^{ep} = C_{ijkl} - \frac{1}{H} H_{ij}^* H_{kl} \quad (4.38)$$

where

$$H_{ij}^* = C_{ijkl} \frac{\partial g}{\partial \sigma_{kl}}$$

$$H_{kl} = \frac{\partial f}{\partial \sigma_{ij}} C_{ijkl}$$

As illustrated above, the generation of fourth order tensor C_{ijkl}^{ep} requires calculating the scalar H as well as the second order tensors H_{ij}^* and H_{kl} . This in turn requires the calculation of partial differential of the failure surface (i.e. $f(\sigma_{ij}) = 0$) and the plastic potential (i.e. $g(\sigma_{ij}) = 0$) with respect to the stress tensor. However, the failure surface and the plastic potential for the cases where $0 \geq \sigma_1 = \sigma_2 \geq \sigma_3$ are with respect to I_1 and J_2 . Therefore, the chain's rule is employed, as follows:

$$\frac{\partial f}{\partial \sigma_{ij}} = \frac{\partial f}{\partial I_1} \frac{\partial I_1}{\partial \sigma_{ij}} + \frac{\partial f}{\partial J_2} \frac{\partial J_2}{\partial \sigma_{ij}} \quad (4.39.a)$$

$$\frac{\partial g}{\partial \sigma_{ij}} = \frac{\partial g}{\partial I_1} \frac{\partial I_1}{\partial \sigma_{ij}} + \frac{\partial g}{\partial J_2} \frac{\partial J_2}{\partial \sigma_{ij}} \quad (4.39.b)$$

Note that only the compressive meridian of failure surface is under investigation in this section, due to the same lateral stress $\sigma_1 = \sigma_2$. Therefore, the partial differential is irrelevant to the Loda angle.

The compressive meridian of the failure surface defined in the previous section is expressed as follows:

$$f(p, q) = q - 1.67 \cdot p - 26.1 \quad (4.40)$$

equivalent to:

$$f(I_1, J_2) = \sqrt{3 \cdot J_2} + 0.557 \cdot I_1 - 26.1 \quad (4.41)$$

The Drucker-Prager type of plastic potential was employed for the non-associated flow rule:

$$g(p, q) = -\tan \varphi \cdot p + q \quad (4.42)$$

equivalent to:

$$g(I_1, J_2) = \frac{\tan \varphi}{3} \cdot I_1 + \sqrt{3} \cdot \sqrt{J_2} \quad (4.43)$$

Hence, by substituting the failure surface function Equation (4.41) and the plastic potential Equation (4.43) into Equation (4.39), the incremental stiffness tensor C_{ijkl}^{ep} can be expressed as:

$$C_{ijkl}^{ep} = C_{ijkl} - \frac{1}{H} H_{ij}^* H_{kl} \quad (4.44)$$

where

$$H = 2G \cdot \left[0.557 \cdot \frac{1+v}{1-2v} \cdot \tan \varphi + 1.5 \right]$$

$$H_{ij}^* = 2G \left[\frac{\tan \varphi}{3} \cdot \frac{1+v}{1-2v} \delta_{ij} + \frac{\sqrt{3}}{2\sqrt{J_2}} s_{ij} \right]$$

$$H_{kl} = 2G \left[0.557 \cdot \frac{1 + \nu}{1 - 2\nu} \delta_{kl} + \frac{\sqrt{3}}{2\sqrt{J_2}} s_{kl} \right]$$

where, δ_{ij} and s_{ij} represent the Kronecker's delta and deviator stress tensor respectively.

For the convenience of numerical manipulation, the fourth order tensor has been suggested to be expressed as a matrix (Han & Chen 1985). As for the problem where the shear components in the stress and the strain could be neglected, the incremental constitutive relation is defined by:

$$\begin{bmatrix} d\sigma_1 \\ d\sigma_2 \\ d\sigma_3 \end{bmatrix} = [C]^{ep} \cdot \begin{bmatrix} d\varepsilon_1 \\ d\varepsilon_2 \\ d\varepsilon_3 \end{bmatrix} \quad (4.45)$$

$$\begin{bmatrix} d\sigma_1 \\ d\sigma_2 \\ d\sigma_3 \end{bmatrix} = \left([C]^e - \frac{1}{H} \cdot \begin{bmatrix} H_{11}^* \\ H_{22}^* \\ H_{33}^* \end{bmatrix} \cdot [H_{11} \quad H_{22} \quad H_{33}] \right) \cdot \begin{bmatrix} d\varepsilon_1 \\ d\varepsilon_2 \\ d\varepsilon_3 \end{bmatrix} \quad (4.46)$$

where,

$$[C]^e = \frac{2G}{1 - 2\nu} \cdot \begin{bmatrix} 1 - \nu & \nu & \nu \\ \nu & 1 - \nu & \nu \\ \nu & \nu & 1 - \nu \end{bmatrix}$$

$$G = \frac{E}{2(1 + \nu)}$$

Hence, the incremental stiffness matrix $[C]^{ep}$ at any strain increment is related to the current stress tensor σ_{ij} and material properties (i.e. E , ν and φ). As defined in the previous section, parameter φ is related to the confining stiffness and the confining pressure.

In summary, once the FRP confinement was effectively activated by the unstable cracking of concrete, the concrete was prevented from failure and can be represented as a perfectly plastic material. In this section, the matrix form of the incremental constitutive model based on perfectly plasticity has been derived.

4.2.2 Iterative stepwise algorithm for stress-strain generation

In this section, a MATLAB program written to generate the stress-strain curve of passively confined concrete under compressive loading is described. The principal stress σ_1 and the principal strain ε_1 were in the direction of compressive loading, while the principal stresses in another two directions were identical ($\sigma_2 = \sigma_3$) and represented the passive confining pressure. The scale of passive confining pressure was dependent on concrete lateral expansion such that:

$$\sigma_2 = k \cdot \varepsilon_2 \quad (4.47.a)$$

$$\sigma_3 = k \cdot \varepsilon_3 \quad (4.47.b)$$

The confining stiffness k and the concrete strength were the inputs of the program, and the curves of $\sigma_1 - \varepsilon_1$ and $\sigma_1 - \varepsilon_2$ were the outputs which were used to facilitate the structural analysis of concrete structural elements with passive confinement.

The concrete response was assumed as an elastic-perfectly plastic material to simplify the algorithm. Therefore, the stress-strain curve consisted of two parts: the linear-elastic and the perfectly plastic. For the stress state of concrete within the failure surface, i.e. $f(\sigma_{ij}) < 0$, concrete exhibits the linear-elastic behaviour:

$$\begin{bmatrix} \sigma_1 \\ \sigma_2 \\ \sigma_3 \end{bmatrix} = [C]^e \cdot \begin{bmatrix} \varepsilon_1 \\ \varepsilon_2 \\ \varepsilon_3 \end{bmatrix} \quad (4.48)$$

where matrix $[C]^e$ can be expressed as follows:

$$[C]^e = \frac{2G}{1-2\nu} \cdot \begin{bmatrix} 1-\nu & \nu & \nu \\ \nu & 1-\nu & \nu \\ \nu & \nu & 1-\nu \end{bmatrix}$$

For the stress state of concrete on the failure surface, i.e. $f(\sigma_{ij}) = 0$, perfect-plasticity of passively confined concrete occurs, and concrete's behaviour can be represented by the incremental material function derived in the last section [i.e. Equation (4.45)].

The end of linear elasticity is the onset of perfect-plasticity. The stress and the strain state at this moment are $\{\sigma_0\}$ and $\{\varepsilon_0\}$ respectively. When the concrete behaves as a linear elastic material, its lateral expansion as a result of compressive loading is so small that the passive confinement of concrete cannot be effectively activated.

Therefore, the confining pressure at the end of linear elasticity can be neglected, and the stress state $\{\sigma_0\}$:

$$\{\sigma_0\} = \{f'_c \quad 0 \quad 0\}^T$$

According to Equation (4.27), the corresponding strain at $\{\sigma_0\}$:

$$\{\varepsilon_0\} = ([C]^e)^{-1} \cdot \{\sigma_0\}$$

After this, with the increasing load applied to concrete, concrete with passive confinement behaves as a perfectly plastic material. The incremental concrete material model has been proposed previously to represent such behaviour:

$$\begin{bmatrix} d\sigma_1 \\ d\sigma_2 \\ d\sigma_3 \end{bmatrix} = [C]^{ep} \cdot \begin{bmatrix} d\varepsilon_1 \\ d\varepsilon_2 \\ d\varepsilon_3 \end{bmatrix} \quad (4.49)$$

The stiffness matrix $[C]^{ep}$ was determined by the failure surface and the plastic potential function, the coefficients of which vary with respect to certain field variables (e.g. confining pressure σ_l and confining stiffness). Details of the generation of matrix $[C]^{ep}$ refers to Equation (4.44).

Hence, the problem was reduced to determining the stress-strain history, based on the following conditions:

$$\begin{cases} \text{Initial condition: } \{\sigma_0\}, \{\varepsilon_0\} \\ \text{Material property: } \{d\sigma\} = [C]^{ep} \cdot \{d\varepsilon\} \\ \text{Consistency condition: } \sigma_l = k \cdot \varepsilon_l \end{cases}$$

Since the stiffness matrix $[C]^{ep}$ varies with respect to the field variables confining pressure and confining stiffness, an iterative stepwise algorithm was used. The flow chart of a loop in the algorithm is illustrated in Figure 4.10.

A constant axial strain increment $d\varepsilon_1$ was applied (step 2) in every loop to initiate the displacement control program. The lateral strain consistent with $d\varepsilon_1$ was then determined by an iterative process through steps 3 to 7, based on the material property and consistency condition. A lateral strain increment $d\varepsilon_l$ was assumed according to the equations in step 3. It follows that the dilation angle was calculated according to the field variables obtained from the last loop, and then the stiffness

matrix was generated. In step 6, the stress increment was calculated through equation (4.49) based on the assumed lateral strain at step 3. The consistency condition was introduced in step 7 to identify the assumed lateral strain increment. The lateral strain increment was not accepted and a new value of Δ was to be attempted, until the consistency condition was met. It is worth mentioning that Δ was initiated at the value of 0.001, and an increase of 0.001 was applied to Δ at every loop from steps 3 to 7.

Once the assumed lateral strain incremental was accepted, the corresponding stress and the strain increment were stored and another axial strain increment $d\varepsilon_1$ was applied for the next loop until the termination of the program.

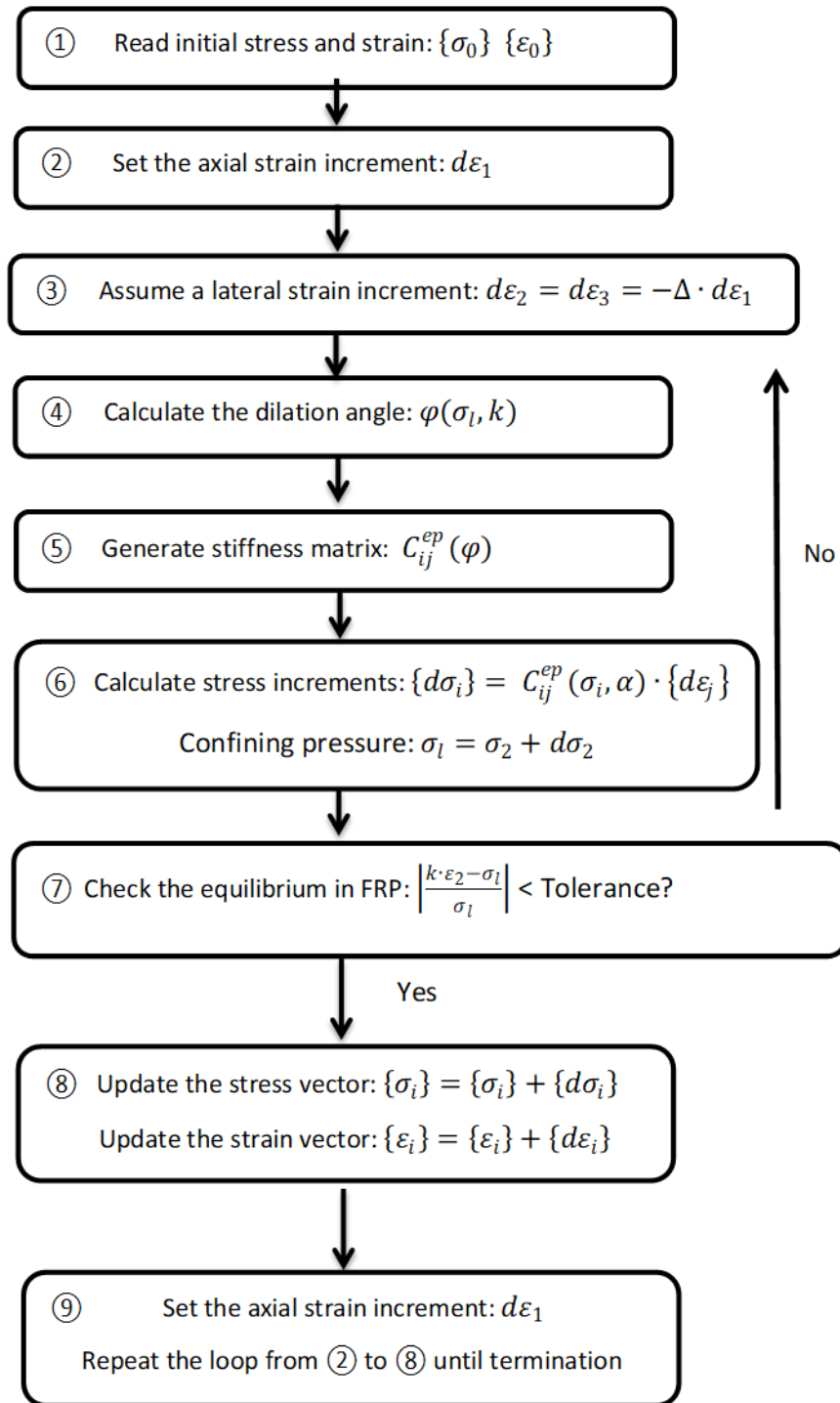


Figure 4.10 Flow chart of the verification program

4.2.3 Numerical simulation through the MATLAB program

The program developed in the previous sections was executed to generate the stress-strain curve of passively confined concrete. The input parameters of the program consisted of concrete strength, elastic constants, and confining stiffness applied to concrete, as is illustrated in Table 4.1. The concrete's strength, Young's modulus, and the Poisson's Ratio were obtained from the multiaxial tests on concrete with active confinement, details of which are provided in section 3.4.1. The confining stiffness of $2580 \text{ MPa}/\varepsilon$ is equivalent to a concrete cylinder of 100 mm diameter wrapped with 3 layers of CFRP sheet. Hence, the program with the input parameters listed in Table 4.1 numerically simulated the scenario of experimental test P1.

Table 4.1 Input parameters for the MATLAB program

Concrete Strength f'_c / MPa	Young's modulus E / GPa	Poisson's Ratio ν	Confining Stiffness k / MPa
59	51.5	0.206	2580

With the compressive stress σ_1 in the loading direction less than f'_c , passively confined concrete was assumed to exhibit linear elastic behaviour and the stress-strain curves in this segment are therefore in the form of a straight line. Following this, the perfectly plastic based program was initiated.

The $\sigma_1 - \varepsilon_1$ and $\sigma_1 - \varepsilon_2$ curves as the output of the program are plotted in Figure 4.11 together with that of the experimental test P1 as the benchmark. The vertical axis represents the stress σ_1 in the loading direction while the lateral axis represents the strain. Due to the sign convention that tensile is positive, the left curve with positive strain represents $\sigma_1 - \varepsilon_2$ and the right represents $\sigma_1 - \varepsilon_1$.

The numerical simulation matches the test data well with only a minor deviation until the lateral strain exceeds 0.008. Hence, the elastic-perfectly plastic assumption is reasonable for lateral strain less than 0.008. However, as the lateral strain increases and becomes larger than 0.008, errors from the numerical program accumulate. At a lateral strain of 1.4%, the strength of passively confined concrete estimated by the program is around 15% higher than that of experimental test

results. As has been presented in the previous Chapter, compaction of the yielding surface in the stress space occurred at a high level of lateral expansion, and concrete did not exhibit perfectly plastic behaviour. Therefore, the perfectly plastic assumption is no longer validated when the lateral strain of passively confined concrete is larger than 0.008.

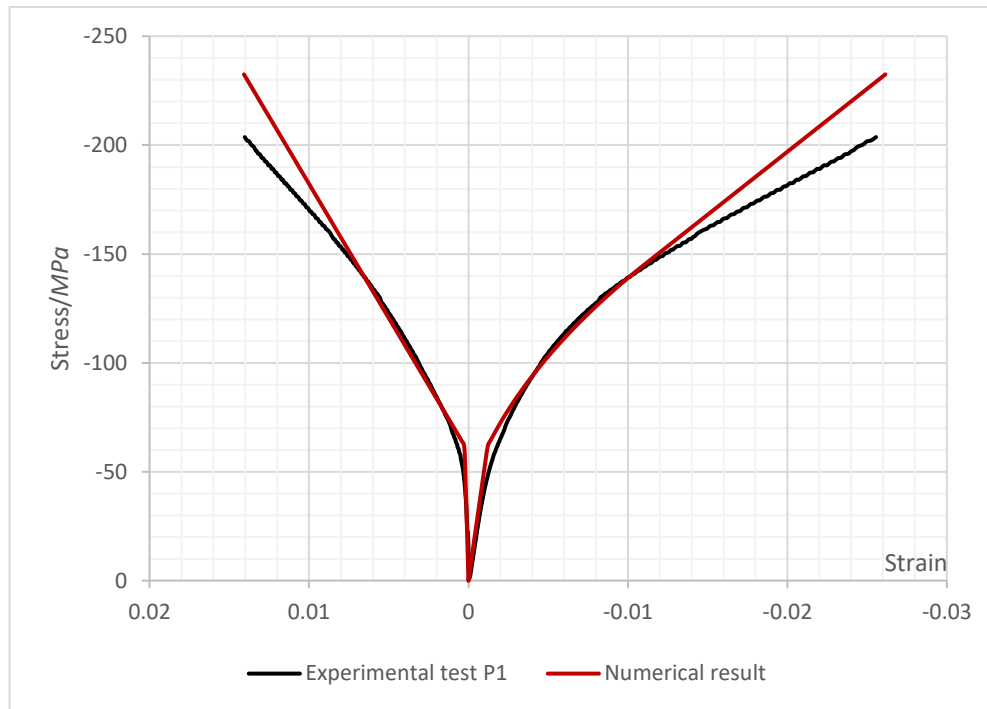
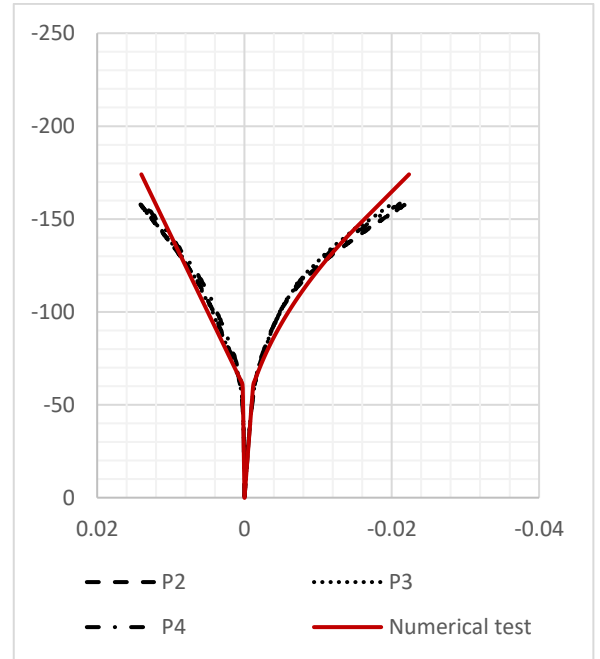
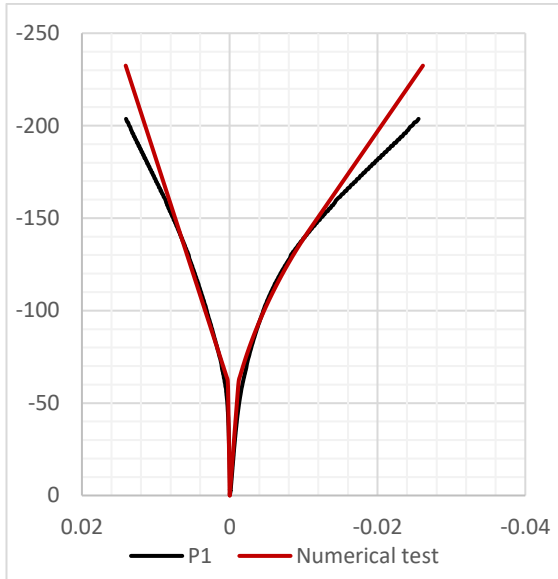


Figure 4.11 Numerical simulation results of the experimental test P1

Other multiaxial tests of passively confined concrete with different levels of confining stiffness were numerically simulated through the program, and the corresponding results are illustrated in Figure 4.12. Similarly, the numerical simulation agrees well with the experimental test results if the lateral strain of concrete is no more than 0.008, which is the onset of the softening of passively confined concrete. The perfectly plastic assumption could lead to an overestimation of loading capacity by as much as 15% at a lateral strain of 1.4%.

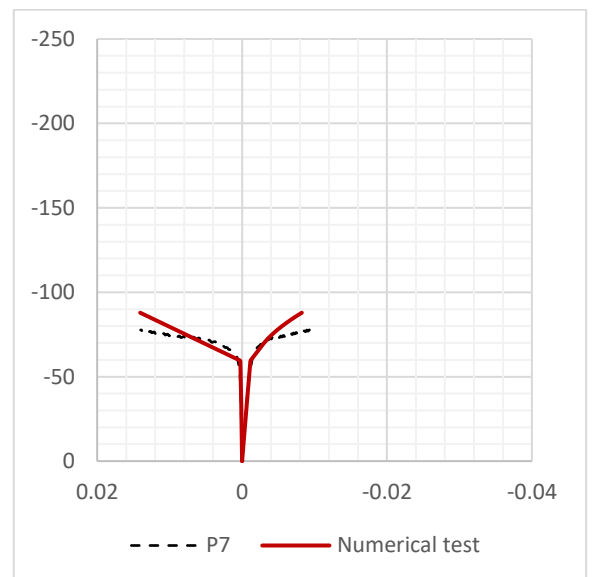
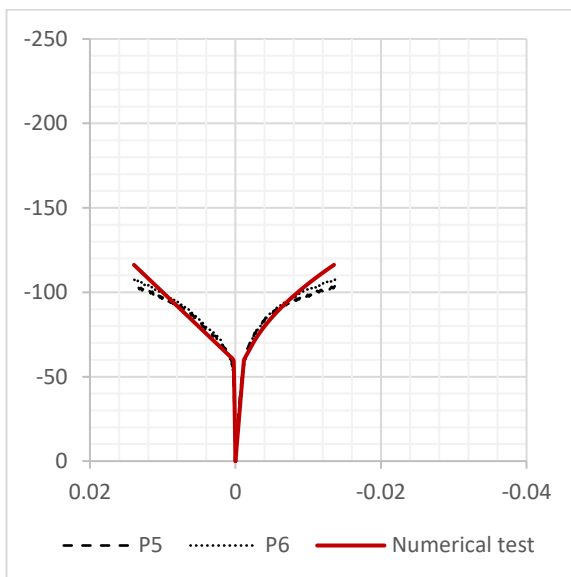
It is worth mentioning that the axial strain at any level of lateral expansion can be accurately predicted by the MATLAB program, as illustrated in Figure 4.12. That is, the plastic flow rule which controls the ratio between the lateral and the axial strain is well defined.

In summary, the program based on the elastic-perfectly plastic assumption is capable of numerically simulating the scenario of passively confined concrete under compressive loading. For the design cases in which the lateral expansion of concrete is more than 0.008, the stress-strain curves obtained by the MATLAB program must be used with caution.



a) 3 layers of CFRP

b) 2 layers of CFRP



c) 1 layer of CFRP

d) 0.5 layer of CFRP

Figure 4.12 Comparison between the numerical and the experimental test results

4.3 Numerical simulation through finite element software

Finite element analysis can solve the continuum mechanical problem with complicated boundary conditions, which makes it versatile for the analyses of structural components. Additionally, the material nonlinearity can be taken into account in a nonlinear finite element software such as ABAQUS. Therefore, it is appropriate to numerically simulate passively confined concrete through ABAQUS as was done in this research.

In this section, the algorithm for the finite element software in solving the material nonlinearity is firstly reviewed. Following this, the results from proposed material model of passively confined concrete being introduced into ABAQUS are presented. The multiaxial tests on passively confined concrete in the previous Chapter were numerically simulated using ABAQUS with the proposed material model and these results are presented. In order to confirm the effectiveness of the material model of passively confined concrete in ABAQUS, the numerical results are finally compared to the experimental ones.

4.3.1 Algorithm in non-linear finite element analysis

According to the theory of continuum mechanics, the quasi-static behaviour of a body (Ω) is governed by the momentum equation:

$$\sigma_{ij,j} + f_i = 0 \quad (4.50)$$

where $\sigma_{ij,j}$ represents spatial differential of stress tensor and f_i is the body force tensor.

There is a type of continuum mechanics problem where the force or the displacement distribution on the boundary of the body ($\partial\Omega$) is known and the field variable distribution within the body is of interest: the initial boundary value problem (IBVP). The Finite Element Method is one of the effective solutions to IBVP. In the finite element method, the body Ω is separated into numerous non-overlapping elements Ω_e :

$$\Omega = \sum_{i=0}^n \Omega_{e,i} \quad (4.51)$$

Moreover, the field variables, displacement tensor $\mathbf{u}(x, y, z)$ and strain tensor $\boldsymbol{\varepsilon}(x, y, z)$ within the element are interpolated according to the element nodal displacement (\mathbf{d}_i):

$$\mathbf{u}(x, y, z) = \sum_{i=1}^n \mathbf{N}_i(x, y, z) \cdot \mathbf{d}_i \quad (4.52)$$

$$\boldsymbol{\varepsilon}(x, y, z) = \sum_{i=1}^n \mathbf{B}_i(x, y, z) \cdot \mathbf{d}_i \quad (4.53)$$

where subscript i indicates the nodal number;

\mathbf{N}_i is the matrix of shape function in associate with nodal i , and

\mathbf{B}_i is the partial differential of \mathbf{N}_i with respect to the coordinates x, y and z .

Based on the virtual work principle, the virtual displacement δu and the corresponding virtual strain $\delta \boldsymbol{\varepsilon}$ can be expressed as:

$$\int_{\Omega} tr([\delta \boldsymbol{\varepsilon}]^T [\boldsymbol{\sigma}]) d\Omega - \int_{\Omega} \delta \mathbf{u}^T \cdot \mathbf{f} d\Omega - \int_{\partial\Omega} \delta \mathbf{u}^T \cdot \mathbf{t} d\Gamma = 0 \quad (4.54)$$

where \mathbf{t} represents the traction on the body boundary $\partial\Omega$ as the force boundary condition. By substituting Equations (4.52) and (4.53) into Equation (4.54) and integrating on an element basis, then:

$$\sum_{i=1}^n \delta \mathbf{d}_i^T \cdot \left(\int_{\Omega_e} \mathbf{B}_i^T \cdot \{\boldsymbol{\sigma}\} d\Omega - \int_{\Omega_e} \mathbf{N}_i^T \cdot \mathbf{f} d\Omega - \int_{\Gamma} \mathbf{N}_i^T \cdot \mathbf{t} d\Gamma \right) = 0 \quad (4.55)$$

Equation (4.55) is valid for any $\delta \mathbf{d}_i^T$; therefore:

$$\int_{\Omega_e} \mathbf{B}_i^T \cdot \{\boldsymbol{\sigma}\} d\Omega - \int_{\Omega_e} \mathbf{N}_i^T \cdot \mathbf{f} d\Omega - \int_{\Gamma} \mathbf{N}_i^T \cdot \mathbf{t} d\Gamma = 0 \quad (4.56)$$

The first term on the left side of Equation 4.56 represents the internal resistance of element i :

$$f_i^{int} = \int_{\Omega_e} \mathbf{B}_i^T \cdot \{\boldsymbol{\sigma}\} d\Omega \quad (4.57)$$

while the other two terms in Equation (4.56) constitute the nodal force of element i to be balanced by f_i^{int} :

$$f_i^{ext} = \int_{\Omega_e} \mathbf{N}_i^T \cdot \mathbf{f} d\Omega - \int_r \mathbf{N}_i^T \cdot \mathbf{t} d\Gamma \quad (4.58)$$

Then the global internal resistance and the global nodal force can be obtained through a linear finite element assembly operator Λ (Simo & Hughes, 2006), such that:

$$\mathbf{F}^{int} = \bigwedge_{i=1}^n f_i^{int} = \int_{\Omega} \mathbf{B}_i^T \cdot \{\boldsymbol{\sigma}\} d\Omega \quad (4.59)$$

$$\mathbf{F}^{ext} = \bigwedge_{i=1}^n f_i^{ext} = \int_{\Omega} \mathbf{N}_i^T \cdot \mathbf{f} d\Omega - \int_r \mathbf{N}_i^T \cdot \mathbf{t} d\Gamma \quad (4.60)$$

The IBVP reduces to the determination of nodal displacement, which satisfies the equilibrium:

$$\mathbf{F}^{int} = \mathbf{F}^{ext} \quad (4.61)$$

Based on Equation (4.59), \mathbf{F}^{int} is a function with respect to the stress tensor $\boldsymbol{\sigma}$, which according to material constitutive relation can be expressed as follows:

$$\{\boldsymbol{\sigma}\} = [\mathbf{D}] \cdot \{\boldsymbol{\varepsilon}\} = [\mathbf{D}] \cdot [\mathbf{B}]_e \cdot \{\mathbf{d}\} \quad (4.62)$$

where $[\mathbf{D}]$ is the constitutive matrix. For nonlinear material such as concrete, matrix $[\mathbf{D}]$ is not constant and varies with respect to the nodal displacement \mathbf{d} . It follows that Equation (4.62) becomes the nonlinear equation of \mathbf{d} . To solve such nonlinear matrix equation, a numerical solution based on a stepwise-iterative algorithm (e.g. the Newton-Raphson iterative) is needed. In such a stepwise-iterative algorithm the external force vector is increased step-by-step and the nodal displacement vector, which is consistent with the force increment, is calculated by the following iteration at every step.

Consider a balanced state at step (n), where the equilibrium is satisfied:

$$\mathbf{F}_n^{int}(\mathbf{d}_n) = \mathbf{F}_n^{ext} \quad (4.63)$$

A nodal force increment $\Delta \mathbf{F}^{ext}$ is applied at the following step (n+1); then, the external force is:

$$\mathbf{F}_{n+1}^{ext} = \mathbf{F}_n^{ext} + \Delta \mathbf{F}^{ext} \quad (4.64)$$

An iteration is needed to calculate the nodal displacement vector \mathbf{d}_{n+1} that remains the equation system in balance. The residual of the equilibrium at step (n+1) can be expressed as follows:

$$\mathbf{R} = \mathbf{F}_{n+1}^{ext} - \mathbf{F}_n^{int}(\mathbf{d}_n) \quad (4.65)$$

According to the Newton-Raphson, the incremental nodal displacement to decrease the residual \mathbf{R} can be calculated by solving the following equation:

$$\frac{\partial \mathbf{R}}{\partial \mathbf{d}} \cdot \{\Delta \mathbf{d}\} = \mathbf{R} \quad (4.66)$$

Then the nodal displacement is updated:

$$\mathbf{d}_{n+1} = \mathbf{d}_n + \Delta \mathbf{d} \quad (4.67)$$

The updated nodal displacement vector is substituted into Equation (4.63) and then the new residual \mathbf{R} of the equilibrium can be determined. Such a process from Equation (4.63) to Equation (4.67) is repeated until the scale of residual \mathbf{R} is within the tolerance. Then the corresponding nodal displacement \mathbf{d}_{n+1} is received as the consistent field variable to the nodal force increment $\Delta \mathbf{F}^{ext}$.

However, there is one problem left in the iteration of nodal displacement: the calculation of $\partial \mathbf{R} / \partial \mathbf{d}$ in Equation (4.66). Since the external nodal force \mathbf{F}_{n+1}^{ext} is constant and independent of nodal displacement, $\partial \mathbf{R} / \partial \mathbf{d}$ can be expressed as follow:

$$\frac{\partial \mathbf{R}}{\partial \mathbf{d}} = - \frac{\mathbf{F}^{int}}{\partial \mathbf{d}} \quad (4.68)$$

By substituting Equation (4.57) into Equation (4.68):

$$\frac{\partial \mathbf{R}}{\partial \mathbf{d}} = - \bigwedge_{i=1}^n \int_{\Omega_e} \mathbf{B}_e^T \cdot \frac{\partial \boldsymbol{\sigma}}{\partial \boldsymbol{\varepsilon}} \cdot \mathbf{B}_e d\Omega \quad (4.69)$$

Hence, the determination of $\partial \mathbf{R} / \partial \mathbf{d}$ reduces to the calculation of vector partial differential $\partial \boldsymbol{\sigma} / \partial \boldsymbol{\varepsilon}$, which is dependent of the material constitutive model.

According to the theory of material plasticity, $\partial\boldsymbol{\sigma}/\partial\boldsymbol{\varepsilon}$ of a time-independent hardening material can be expressed as follows (Hinton et al., 2010):

$$\frac{\partial\boldsymbol{\sigma}}{\partial\boldsymbol{\varepsilon}} = \mathbf{C} - \frac{\mathbf{C}^T \cdot \mathbf{b} \cdot \mathbf{a}^T \cdot \mathbf{C}}{A + \mathbf{b}^T \cdot \mathbf{C} \cdot \mathbf{a}} \quad (4.70)$$

where \mathbf{C} is the matrix form of tensor C_{ijkl} defined in Equation (4.28), which represents the material elastic behaviour; vector \mathbf{a} is the gradient of yield surface in the stress space ($\partial f/\partial\boldsymbol{\sigma}$); vector \mathbf{b} is the gradient of plastic potential in the stress space ($\partial g/\partial\boldsymbol{\sigma}$); and parameter A is governed by the hardening rule and can be expressed by $A = -\left\{\frac{\partial f}{\partial\varepsilon^{pl}}\right\}^T \cdot \left\{\frac{\partial g}{\partial\boldsymbol{\sigma}}\right\}$. Obviously, vector \mathbf{a} and \mathbf{b} vary with respect to stress state $\boldsymbol{\sigma}$; therefore, $\partial\boldsymbol{\sigma}/\partial\boldsymbol{\varepsilon}$ is not constant and needs to be determined numerically. In most commercial finite element software (e.g. ABAQUS), an implicit iteration is used to determine $\partial\boldsymbol{\sigma}/\partial\boldsymbol{\varepsilon}$ based on the back-Euler algorithm, details of which refer to Simo and Hughes (2006), Hinton et al. (2010) and Lee and Fenves (2001).

4.3.2 Material model of passively confined concrete in FEA

ABAQUS was used to conduct the finite element analysis on the passively confined concrete structures. The material model developed in section 4.1 for passively confined concrete was introduced to ABAQUS under the framework of an incorporated material model - Concrete Damage Plasticity (CDP).

4.3.2.1 Framework for the plastic-damage model CDP

Lubliner et al. (1989) proposed the constitutive model based on the plasticity theory, with a novel yielding surface function which fits well with the multiaxial tests results from Kupfer et al. (1969). Lee and Fenves (1998) maintained the formulation of plasticity theory but modified the yield surface function of Lubliner et al. (1989) by introducing two hardening parameters, since concrete exhibits different hardening behaviour when subject to compressive and tensile loading.

When subject to cyclic loads, concrete exhibits stiffness reduction according to the observations from experimental tests conducted by Karsan and Jirsa (1969). Such stiffness reduction is believed to be attributed to the damage accumulated in the process of loading. Therefore, Lee and Fenves (1998) introduced a scalar

degradation variable in accordance with plastic deformation, such that the loading/unloading stiffness impaired with the increasing deformation can be taken into account. It is worth mentioning that the scale degradation variable is decoupled with the formulation of the plasticity theory. Without the definition on the scale degradation variable, the plastic-damage model reduces to the conventional plasticity-based model.

The material model proposed by Lee and Fenves (1998) was incorporated into ABAQUS and termed as CDP (Systemes, 2014) for this research with some modification. The Drucker-Prager hyperbolic function was taken by CDP as the plastic flow rule, which is a smooth cone surface in stress space. The hardening rule in the model of Lee and Fenves (1998) was simplified such that the hardening parameters were related to the equivalent tensile plastic strain and the equivalent compressive plastic strain, which are the maximum and the minimum eigenvalue of the plastic strain tensor, respectively.

In summary, the CDP model in ABAQUS was simplified and defined as a conventional plasticity-based material model. The yield surface function proposed by Lee and Fenves (1998) with two different hardening parameters was used. The evolution of the yield surface in the process of plasticity was in an isotropic pattern and controlled by the hardening rule, which related the hardening parameter to the equivalent strain. The plastic flow rule was defined by the Drucker-Prager hyperbolic function.

4.3.2.2 Parameter identification of the CDP

The material constitutive model proposed for passively confined concrete in this research is plasticity-based, as discussed in section 4.1. The yield surface proposed by Lee and Fenves (1998) and the Drucker-Prager form plastic flow function were employed by the model developed, which are the same as those in the model CDP. As a result, it was appropriate to define the material model in ABAQUS based on the CDP framework.

The mechanical performance of concrete is notably enhanced by its lateral confinement; therefore, the parameters in the material model varied with respect

to the confining pressure, the lateral expansion and the confining stiffness, which can be regarded as the field variables in ABAQUS. Therefore, the user subroutine option USDFLD in ABAQUS was needed whereby the field variables could be redefined and related to material parameters. There were three field variables included in the material model proposed, as listed in Table 4.2. The confining pressure as Field 1 was calculated by the averaged principal stresses, and the lateral expansion as Field 2 was calculated by the averaged principal strain. Then the last field variable, confining stiffness, was evaluated by the ratio between the other two.

It is worth mentioning that the parameters identified in this section are in accordance with the conventional concrete used for the multiaxial tests in Chapter 3. Adjustment of the parameters might be needed for the numerical simulation of passively confined concrete with another level of concrete strength.

Table 4.2 Material-properties-dependent field variables

	Physical interpretation	Formula
Field 1	Confining pressure	$(\sigma_2 + \sigma_3)/2$
Field 2	Lateral expansion	$(\varepsilon_2 + \varepsilon_3)/2$
Field 3	Confining stiffness	- Field 1 / Field 2

i. Elastic Constants

Young's modulus and Poisson's ratio had to be defined in CDP as elastic constants. For the conventional concrete tested in the lab, these two constants were equal to 51 *GPa* and 0.206 respectively.

ii. Yield surface

The evolution of the yield surface in the process of plastic development is in an isotropic pattern; that is, the shape of the yield surface remains unchanged and the corresponding parameters are constant. According to ABAQUS Theory Manual (Systemes, 2014), the shape of the yield surface in CDP is determined by the parameters f_{b0}/f_{c0} and κ , which are related to the parameters α and γ in Equation (4.1). The relationship between f_{b0}/f_{c0} and α is expressed by Equation (4.71), while that between κ and γ is expressed by Equation (4.72). As identified in section 4.1,

the α and γ are equal to 0.1145 and 3 respectively for the concrete used in the multiaxial tests; therefore, f_{b0}/f_{c0} and κ were calculated according to Equations 4.71 and 4.72 and the results are listed in Table 4.3.

$$\frac{f_{b0}}{f_{c0}} = \frac{\alpha - 1}{2\alpha - 1} \quad (4.71)$$

$$\kappa = \frac{\gamma + 3}{2\gamma + 3} \quad (4.72)$$

Table 4.3 Parameters for the shape of the yield surface

f_{b0}/f_{c0}	κ
1.149	0.6667

iii. Hardening parameter

The compressive parameter σ_c identified in section 4.1.2 is a function with respect to the equivalent compressive plastic strain (ϵ_c^{pl}) and the lateral strain (ϵ_l), which is the field variable "Field 2". ABAQUS cannot read the hardening rule in the form of a function; instead, it can accept data points only. Therefore, data points were calculated according to the function of the hardening rule and imported into ABAQUS. Linear interpolation was used by ABAQUS for the determination of the values between the data points.

Table 4.4 Data points imported into ABAQUS for hardening rule

Yield stress / MPa	Inelastic Strain	Field 2
41.3	0	0.008
59	0.001855	0.008
59	0.05	0.008
16.4	0	0.02
23.5	0.001855	0.02
23.5	0.05	0.02

The data points were calculated based on Equation (4.13), the results of which are listed in Table 4.4. As illustrated in Figure 4.13, two broken lines were plotted according to the data points, which constitutes the boundaries of lateral expansion. In ABAQUS, the value of the hardening parameter was assumed to be constant outside of the range of independent variables defined. For lateral strain less than 0.008, the upper broken line governs the hardening rule and the concrete behaved as a perfectly plastic material.

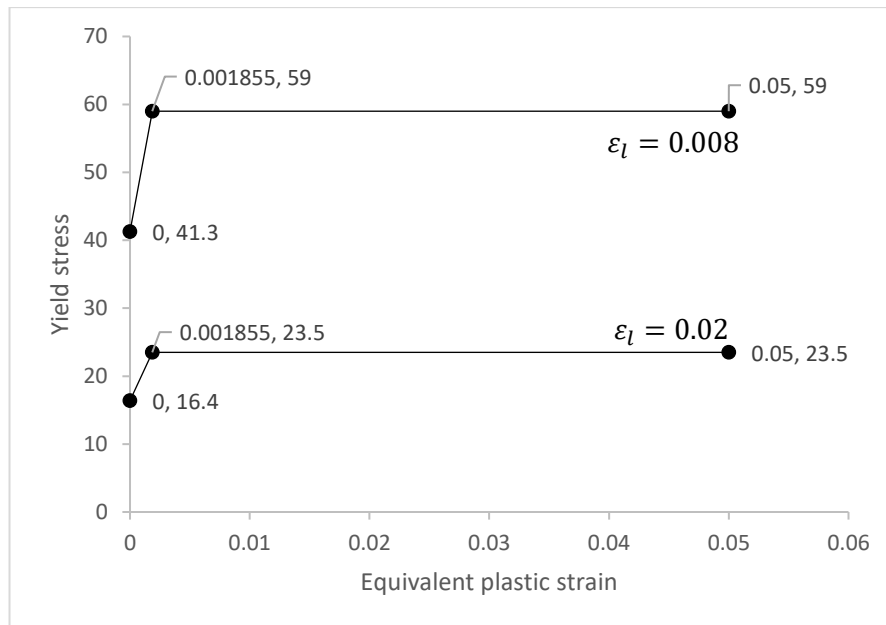


Figure 4.13 Linear interpolation between data points for hardening rule

iv. Plastic flow rule

The plastic flow rule is governed by a Drucker-Prager type function in the material developed, where dilation angle φ is the only parameter. As discussed in section 4.1.3, the dilation angle φ is related to the confining pressure and the confining stiffness, which are the field variable Field 1 and Field 3, respectively. The definition of plastic flow rule in ABAQUS was similar to that of hardening rule. The data points were calculated based on the broken line Equation 4.24 and imported to ABAQUS. Linear interpolation was used by ABAQUS for the determination of the values of φ between the data points.

Table 4.5 Data points imported into ABAQUS for plastic flow rule

Dilation angle φ	Field 1 /MPa	Field 3 /MPa
48	0	2623
48	-2	2623
2	-18	2623
2	-100	2623
50	0	1748
50	-2	1748
2	-18	1748
2	-100	1748
56.3	0	874
56.3	-2	874
2	-18	874
2	-100	874

4.3.3 Numerical simulation through ABAQUS

In this section, the results of the experimental tests on passively confined concrete as numerically simulated through ABAQUS with the material model defined in the previous sections are presented. The numerical results are compared to those obtained from the experimental tests to confirm that material model CDP can be modified to simulate passively confined concrete. Four numerical simulations were carried out with four different levels of lateral confining stiffness in accordance with those in the experimental tests.

4.3.3.1 Modelling of the passively confined concrete cube

The 100 mm cubic specimens in the experimental tests were modelled at full size with the compressive load applied in the vertical direction. The passive lateral confinement was applied through four rigid pads in contact with the sides of the cubic specimen in a frictionless manner. Rotational constrain was defined at the centre of each rigid shell such that the translation was only allowed in the direction perpendicular to the cube side.

The linear relationship between confining pressure and lateral expansion was realised through the spring installed in the centre of rigid pads. In the experimental tests of Mac^{2t}, the confining stiffness was expressed in the form of σ_l/ε_l . However,

in ABAQUS the spring property had to be defined by the ratio between the spring force and spring displacement (F/Δ).

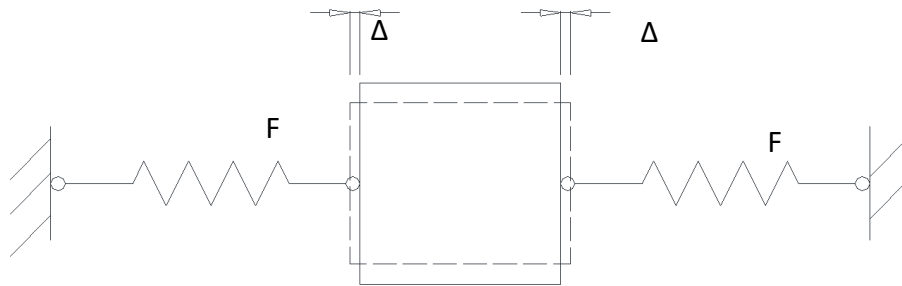


Figure 4.14 Diagram of spring defined in ABAQUS

From Figure 4.14, the lateral strain and the confining pressure can be calculated as follow:

$$\varepsilon_l = \frac{2 \cdot \Delta}{l} \quad (4.73)$$

$$\sigma_l = \frac{F}{A} \quad (4.74)$$

where A and l are the cubic surface area and cubic length respectively.

Then, the spring property can be expressed by σ_l/ε_l as follows:

$$\frac{F}{\Delta} = \frac{\sigma_l}{\varepsilon_l} \cdot 2 \cdot \frac{A}{l} \quad (4.75)$$

According to Equation (4.75), the spring properties of specimens in the ABAQUS modelling, corresponding to the experimental tests, were calculated and are listed in Table 4.6.

Table 4.6 Spring property in ABAQUS model

Experimental tests specimen	σ_l/ε_l MPa	F/Δ N/m	Numerical simulation No.
P1	2623	5.25E+08	A1
P2 P3 P4	1748	3.50E+08	A2
P5 P6	874	1.75E+08	A3
P7	437	8.74E+07	A4

The deformable brick element with reduced integration (C3D8R) and the rigid shell element (R3D4) were used for the concrete cubic specimen and the rigid pads respectively. The mesh size of the cube and the shells were 10 mm but since the uniform distribution of stress and strain was expected, the numerical results are independent of the mesh size.

4.3.3.2 Numerical simulation results

Firstly, the loading paths of passively confined concrete specimens obtained from ABAQUS numerical simulation are plotted in Figure 4.15 and compared with those of the experimental tests to evaluate the yielding surface and the hardening rule defined. The loading path of A2, A3 and A4, agree well with that of the experimental tests, while the loading path of A1 deviates from that of experimental test P1 with the same level of confining stiffness.

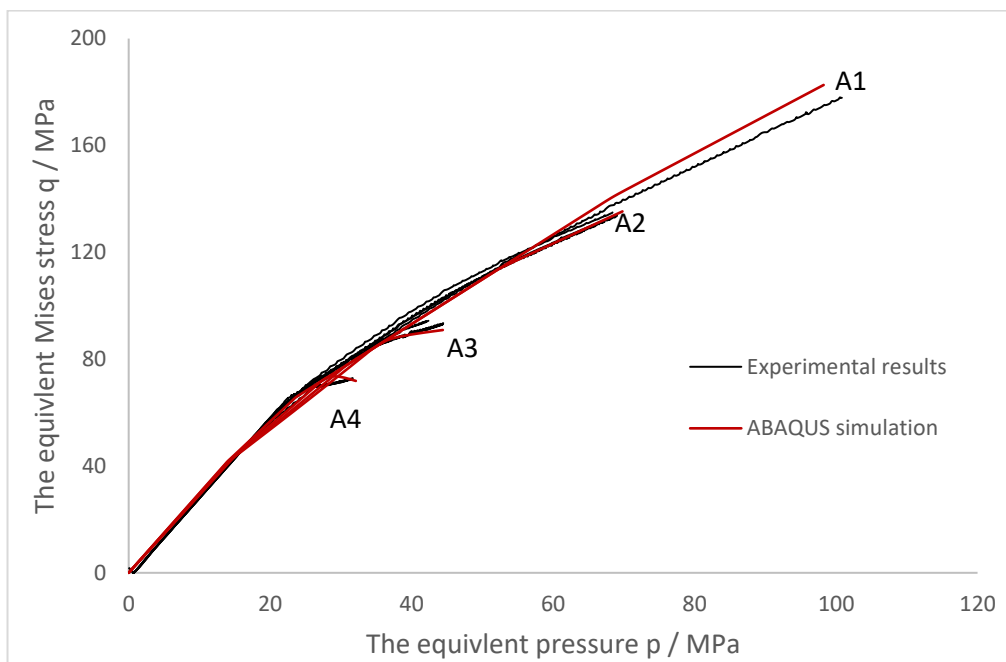


Figure 4.15 Loading path of concrete in the experimental and the numerical test

The compressive meridian of the yielding surface at a lateral strain of 0.01 and 0.014 is plotted in Figure 4.16 according to the yield surface function and the hardening rule defined in section 4.1. The red points marked in Figure 4.16 represent the concrete stress state of the experimental test P1 when its lateral strain is at 0.01 and 0.014. As discussed in section 4.1, the compressive meridian function exhibits a good correlation with the corresponding experimental data

points. However, the data points of test P1 are always located below the yield surface, as shown in Figure 4.16.

A similar conclusion has been made by Chen (1994): the linear compressive meridian of the yielding surface could overestimate the stress state of concrete at a high level of hydrostatic pressure. Therefore, errors in predicting the loading path might occur when the load and lateral confining pressure is large, which was the case with test P1 where the concrete specimen was subjected to a high level of passive confinement and compressive load.

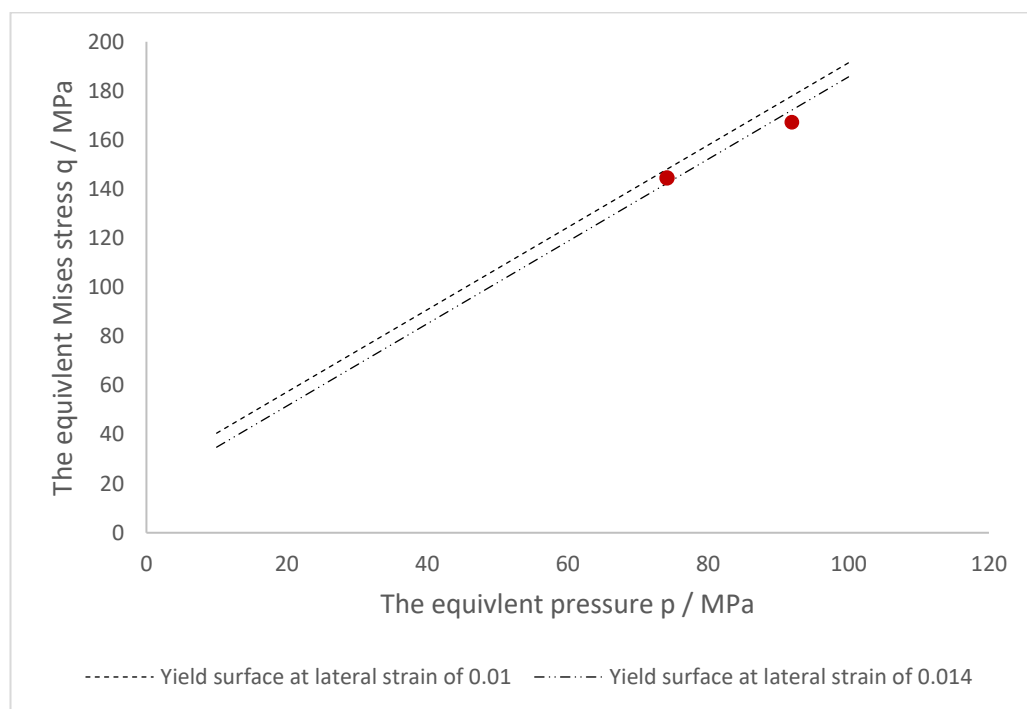


Figure 4.16 Comparison between the defined yielding surface and data points from experimental test P1

The stress and the strain were uniformly distributed in the concrete specimen according to the numerical simulation results. σ_1 and ε_1 represent the stress and the strain in the loading direction while σ_2 and ε_2 represent the stress and the strain in the lateral direction. The stress-strain curves of $\sigma_1 - \varepsilon_2$ and $\sigma_1 - \varepsilon_1$ according to the numerical simulation results are plotted in Figure 4.17 (red lines) and compared with that of the experimental test results (black dashed lines).

Since the concrete was passively confined, there is a linear relation between lateral stress (σ_2) and lateral strain (ε_2):

$$\sigma_2 = k \cdot \varepsilon_2 \quad (4.76)$$

Therefore, the $\sigma_1 - \varepsilon_2$ curve has the same trend as $\sigma_1 - \sigma_2$, which represents the stress state history. That is, the accuracy of the numerical simulation of the $\sigma_1 - \varepsilon_2$ curve depends on whether the loading path of passively confined concrete can be captured. As discussed previously, the error of the loading path prediction might occur when the hydrostatic pressure is at a high level which was the case with A1. As a result, the $\sigma_1 - \varepsilon_2$ curves obtained from ABAQUS analysis agrees well with the experimental tests except for A1, where the stress σ_1 was overestimated by 10%.

The $\sigma_1 - \varepsilon_1$ curves obtained by ABAQUS agree well with the experimental tests, which indicate that the plastic flow rule was defined correctly. Hence, the material model CDP with appropriated modification is capable of simulating passively confined concrete.

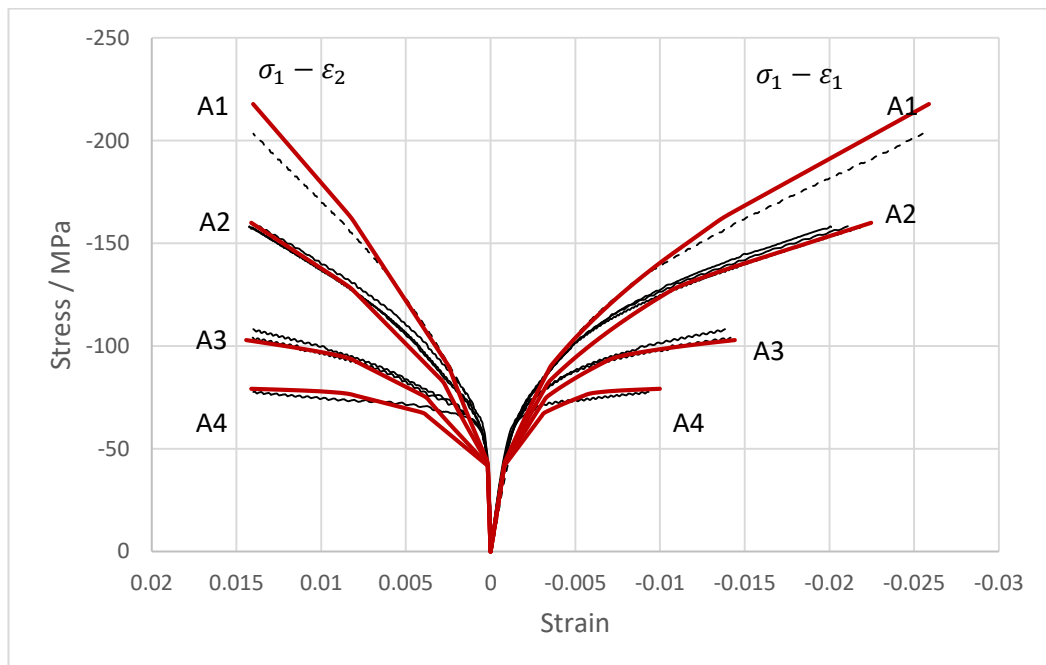


Figure 4.17 Stress-strain curves from the numerical and the experimental tests

4.4 Summary

In this Chapter, a plasticity-based material has been proposed according to the experimental observations made in Chapter 3. The proposed material model is capable of representing the behaviour of passively confined concrete in stress space. Moreover, the proposed material model considers the effect of FRP confinement on the dilation property of concrete.

For a design-oriented problem, the stress-strain relationship of passively confined concrete is of interest, which can be obtained through the developed MATLAB program. Provided the lateral expansion of concrete is no more than 0.008, the behaviour of passively confined concrete can be well predicted by the program. Finally, the proposed material model can be introduced into the nonlinear finite element software ABAQUS, which facilitates the analysis of mechanical problems with complicated boundary condition.

5 Multiaxial tests on rubberised concrete

Rubberised concrete is a novel construction material initially proposed for environmental purposes, where the mineral aggregates of conventional concrete are partly replaced by one of the reused tyre components - rubber. With the increased rubber content, the rubberised concrete exhibits impaired fresh properties and strength reduction. According to previous research from the University of Sheffield, the former issue can be addressed by an optimal mix design, details of which are provided in section 2.1. Despite this, it has been found in the compressive tests, rubberised concrete exhibits larger lateral expansion under compressive loading compared to its counterpart - conventional concrete without rubber content.

To exploit the deformability of rubberised concrete and address the strength reduction, FRP was introduced to the rubberised concrete as lateral confinement. FRP confinement – a type of passive confinement – is activated by the lateral expansion of rubberised concrete. Then FRP produces the confining pressure and enhances the strength and the ductility of rubberised concrete. Most importantly, a pilot study has shown that FRP confined rubberised concrete (CRC) can enable much larger deformations compared to conventional concrete, which makes it feasible for some unique structural applications; for instance, it can be placed in the critical region of a frame's structure where an enormous deformation is expected in rare events such as earthquakes with the occurrence rate of once every 2000 years.

In order to enable engineering use of CRC components, it is essential to not only understand the material properties of this novel material but also develop material models which can facilitate its structural analysis and design. Therefore, multi-axial tests on rubberised concrete were conducted for this present thesis to identify its mechanical behaviour.

5.1 Specimens preparation

The multiaxial tests in this research focused on rubberised concrete in which recycled rubber particles constitute 60% volume of the aggregates. The multiaxial testing apparatus Mac^{2t} is in possession of a restriction requirement on the cubic

specimen which were to be tested. Therefore, the specimens were carefully prepared, details of which are provided in this section. More than 20 rubberised concrete cubic specimens were prepared, and then the specimens in the best condition in terms of shape were selected to be tested.

5.1.1 Mix design

Because of its high rubber content, fresh rubberised concrete can exhibit poor fresh properties, specifically segregation or low slump. The former can be mitigated by improving the concrete particle packing structure. The cement blender for rubberised concrete used in this research consisted of Silica Fume (10%), Pulverised Fuel Ash (10%) and cement (80%). The ultra-fine particle, Silica Fume, can fill into the gap of cement particles and therefore improve particle packing. The plasticiser and the superplasticiser were introduced into the mix as admixtures so as to maintain the workability of the fresh rubberised concrete.

According to a parametric study on mix design by Samar et al. (2016), a concrete mix with a water-cement ratio of 0.35 exhibits a good balance between the fresh property and the compressive strength when the mineral aggregates are largely replaced by reused rubber. The details of the concrete mix used here are illustrated in Table 5.1.

Table 5.1 Optimised concrete mix

Material	Optimised mix
CEM II – 52.5 MPa	340 kg/m ³
Silica Fume (SF)	42.5 kg/m ³
Pulverised Fuel Ash (PFA)	42.5 kg/m ³
Aggregates 0/5mm	820 kg/m ³
Aggregates 5/10mm	364 kg/m ³
Aggregates 10/20mm	637 kg/m ³
Water	149 l/m ³
Plasticiser (Sika Viscoflow 1000)	2.5 l/m ³
Superplasticiser (Sika Viscoflow 2000)	5.1 l/m ³

5.1.2 Recycled rubber products

The tests in this research focused on the rubberised concrete in which the recycled rubber particles constituted 60% of the aggregates (by volume). That is, the mineral aggregates of the conventional concrete mix illustrated in Table 5.1 had to be partly replaced by rubber particles.

The aggregate grading represents the relative particle proportion, and the concrete property can be adversely affected by poor grading. However, little research has been done regarding the optimisation of rubber particle grading. Therefore, in this research, the grading of rubber particles was determined based on the requirements originally proposed for mineral aggregate in ASTM C 33 (2005).

In the Concrete & Material Lab of the University of Sheffield, rubber particles were purchased from two sources: Gumiimpex and Conica. The rubber particles in the shape of crumb/granulate were provided by Gumiimpex and were grouped according to particle size: 0-0.5, 0.5-2 and 2-3.5 mm, while Conica provided with the rubber products (crumb/chips) at relatively large sizes: 2-6, 4-10 and 10-20 mm. Four of the rubber products (all three from Gumiimpex and the 2-6 mm from Conica) were combined to substitute fine aggregate while the remaining two were used for coarse aggregate replacement.

The relative proportion between the different types of recycled rubber products was determined through a trial and error process. The relative proportion for the fine and the coarse rubber particles products are listed in Table 5.2 and Table 5.3, respectively. The results of sieve analysis in the form of a grading curve are illustrated in Figure 5.1. The grading curves of both the fine and the coarse rubber particles are within limits specified in standard ASTM C 33.

Table 5.2 Relative proportion of rubber particles for fine aggregates replacement

<i>Rubber source</i>	<i>Gumiimpex</i>			<i>Conica</i>
<i>Particle size</i>	0-0.5	0.5-2	2-3.5	2-6
<i>Mass ratio</i>	3	4	1	1

Table 5.3 Relative portion of rubber particles for fine aggregates replacement

Rubber source	Gumiimpex	Conica
Particle size	4-10	10-20
Mass ratio	3	5.25

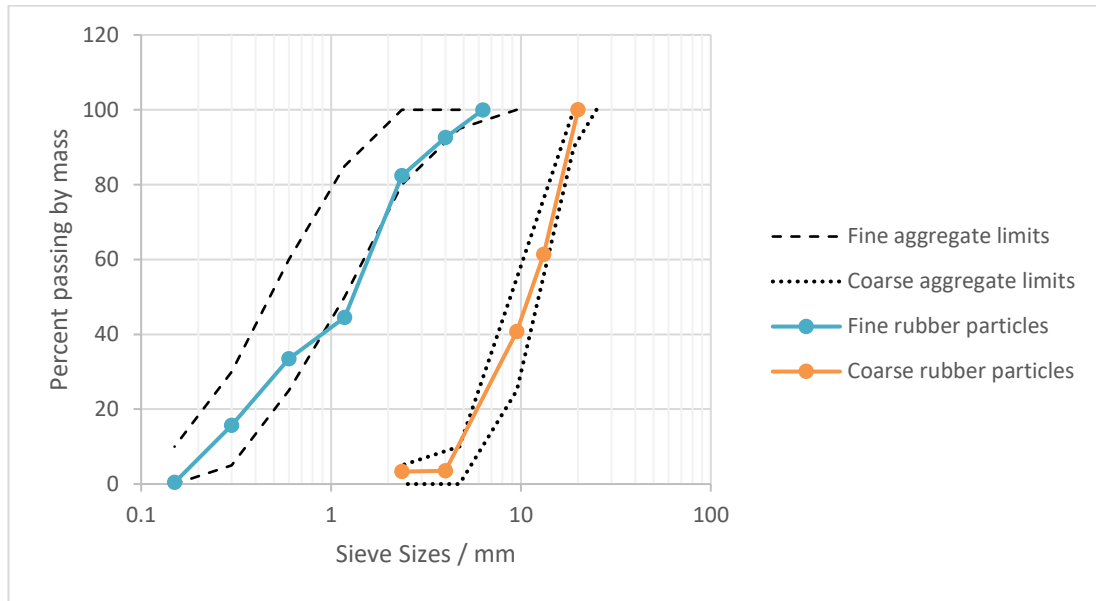


Figure 5.1 Grading curves of the fine and the coarse rubber particles

5.1.3 Production of rubberised concrete specimen

In the multiaxial testing of conventional concrete, the concrete specimens were prepared through a process of casting, cutting and polishing. That is, a large concrete block was cast and cut into cubes (105 mm) using a saw after having been cured for no less than 28 days. Following this, the cubes were polished such that the length of the edge was approximately 100 mm and the difference between the edges in the same direction was less than 0.1 mm. However, the cutting process could not be applied to rubberised concrete since the rubber particles were too tough to be cut using the concrete saw. Hence, the cubic specimen had to be directly cast. Twelve steel cubic moulds in a relatively good condition were selected such that the rubberised concrete specimens produced from the moulds met the requirements of Mac^{2t}: 1. Specimen faces must be flat and smooth; 2. Two adjacent faces must be perpendicular to each other.

The rubberised concrete was mixed in the lab using a rotary mixing machine. The aggregates, including both the mineral aggregates and the recycled rubber particles, were placed in a container and dry mixed for 30 seconds. After this, half of the total amount of water was added to the container. The mineral aggregates, rubber particles and water were mixed for one minute and then covered by a plastic film to allow the aggregates to be saturated. This was then followed by adding the cement blender (cement, silica fume and fly ash), the remainder of the water and the chemical admixtures to the container. All materials were finally mixed for another three minutes before cubic moulds were filled the fresh rubberised concrete. The moulds were then placed on a vibration table for 30 seconds to compact the fresh concrete and remove the air content. As mentioned previously, a smooth and flat surface of the cubic specimen was required for testing by Mac^{2t}; therefore, the top surface of the specimen had to be ground after it had been cured and hardened. However, the tough rubber particles were very likely to be ripped off during the process of polishing and leave a hole on the top of the cubic specimen. In order to facilitate the grinding process, the fresh rubberised concrete was topped with a layer of high strength cement mortar, as illustrated in Figure 5.2.

Having been filled by fresh rubberised concrete, the cubic moulds were covered with plastic films to maintain the water content in the fresh concrete. Demoulding was then conducted in 48 hours, and the rubberised concrete specimens were placed in a curing room for 28 days. Following the, the cubic specimens were sent to the workshop for polishing of their top surface. Figure 5.3 illustrates a cubic specimen with the top surface polished.

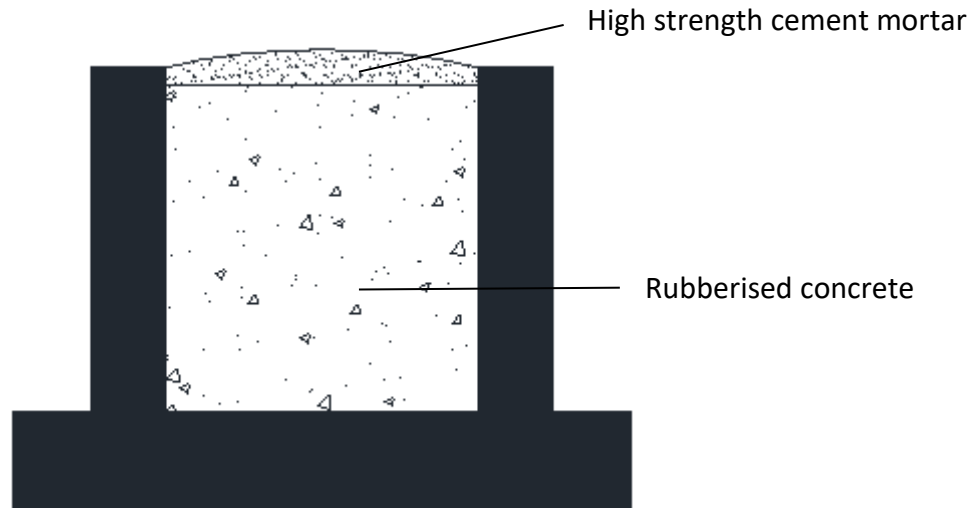


Figure 5.2 Profile of the mould with rubberised concrete and cement mortar top



Figure 5.3 Rubberised concrete specimen with top surface polished

5.2 Testing scheme

The testing scheme for rubberised concrete is similar to that for conventional concrete presented in Chapter 3. The strength criterion of rubberised concrete was determined through a conventional multiaxial testing scheme; then, the rubberised concrete with passive lateral confinement under compressive loading was physically simulated. The compressive meridian of the failure surface was obtained in the

former tests, which became the benchmark when compared to the loading path of rubberised concrete with passive confinement.

5.2.1 Multiaxial tests on rubberised concrete with active confinement

In this group of tests, a loading path was predefined to the cubic specimen by Mac^{2t}. Hydrostatic pressure was applied from the beginning, which represented the level of active confinement. The compressive pressure in the lateral direction was maintained while increasing the load in the vertical direction up to the peak to identify the strength criterion of rubberised concrete. Five tests with different levels of active confinement were conducted, the details of which are listed in Table 5.4.

The loading steps applied by Mac^{2t} are as follows:

1. Applying contacting stress of 0.4 MPa to the specimen in all three directions.
2. Hydrostatic pressure was then applied in the load control mode up to a certain level.
3. Maintaining the active confining pressure in the lateral direction (x and y), through the load control program; increasing displacement in another direction (z) through the displacement control program until the corresponding pressure reached the peak.

Table 5.4 Constant confining pressure

<i>Specimen No.</i>	<i>Confining pressure/MPa</i>
RR1	0.7
RR2	5
RR3	10
RR4	15
RR5	20

5.2.2 Multiaxial tests on rubberised concrete with passive confinement

In this group of tests, the loading path of passively confined concrete was the objective, which was compared with the failure surface obtained in the former testing group to identify its failure mechanism.

Mac^{2t} was used to physically simulate the scenario of passive confinement to the specimen (i.e. applying the confining pressure in accordance with concrete lateral

expansion). The confining stiffness, as a parameter in the control program, represented the ratio of the confining pressure (σ_l) and the concrete lateral expansion (ε_l). Five compressive tests were conducted on rubberised concrete with different levels of confining stiffness, as illustrated in Table 5.5.

Table 5.5 Confining stiffness

<i>Specimen No.</i>	<i>Confining stiffness /MPa</i>	<i>Equivalent to the 102 mm cylinder confined by:</i>
<i>RP1</i>	1748	2 layers of CFRP
<i>RP2</i>	874	1 layer of CFRP
<i>RP3</i>	874	1 layer of CFRP
<i>RP4</i>	437	0.5 layers of CFRP
<i>RP5</i>	174.8	0.2 layers of CFRP

The steps for multiaxial tests with passive confinement are as follows:

1. Applying contacting stress of 0.4 MPa to the specimen in all three directions.
2. Increasing load in the z direction in the displacement control mode then updating confining pressure according to the lateral expansion and confining stiffness.

5.3 Multiaxial testing results of rubberised concrete

5.3.1 Active confinement

The compressive testing results of concrete with constant confining pressure are illustrated in Figure 5.4 in the form of stress-strain curves where stress in the loading direction (σ_z) is plotted against strain (ε_x , ε_y and ε_z). The vertical axis represents σ_z while the horizontal axis represents strain. The peak compressive load that the rubberised concrete specimen sustained enhanced with the increase of confining pressure. The peak σ_z of specimen RR5 was around 50 MPa, five times as much as that of specimen RR1 with little lateral confinement.

Apart from the compressive loading capacity, the ductility of rubberised concrete was improved by the confining pressure. σ_z of specimen RR1 dropped by around 20% to the maximum value at strain ε_z of 0.0048, while for the specimens with relatively large confining pressure – RR4 and RR5 – little strength decrease could be observed

in the post-peak region. Additionally, for specimens RR3, RR6 and RR5, compressive strain in the loading direction could have increased to 4 % if the tests had not been terminated. Therefore, rubberised concrete with adequate lateral confinement is extremely deformable in the loading direction.

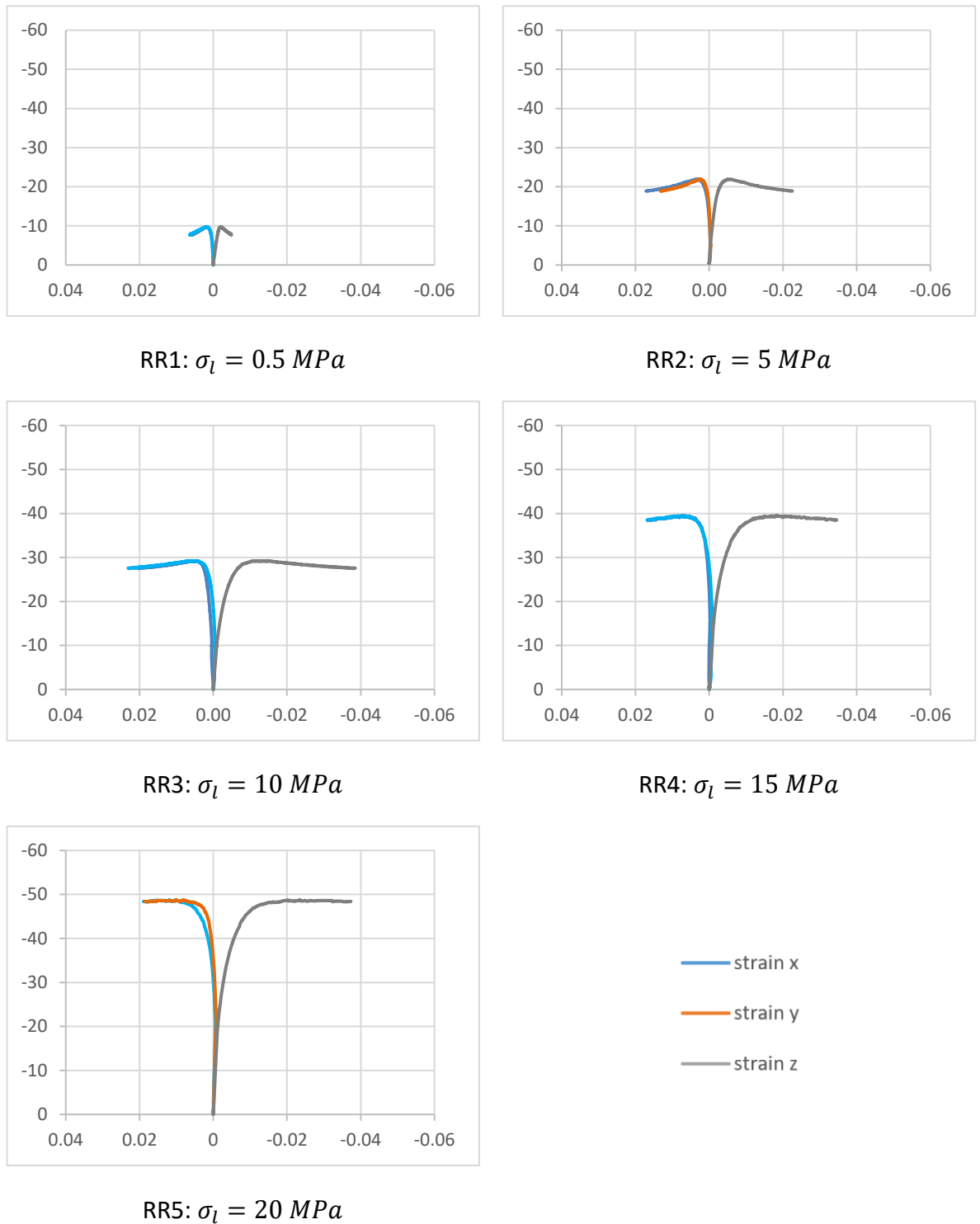


Figure 5.4 Stress-strain of rubberised concrete with constant confining pressure

The stress state corresponding to the peak compressive load for each test is illustrated in Table 5.6. The equivalent pressure (p) and Mises equivalent stress (q) in accordance with the stress state were then calculated according to the equation:

$$p = -\frac{1}{3} \cdot (\sigma_1 + \sigma_2 + \sigma_3) \quad (5.1)$$

$$q = \sqrt{\frac{1}{2} [(\sigma_1 - \sigma_2)^2 + (\sigma_2 - \sigma_3)^2 + (\sigma_3 - \sigma_1)^2]} \quad (5.2)$$

Afterwards, the data points listed in Table 5.6 were plotted in the p - q coordinate system as illustrated in Figure 5.5. The trend line of the data points was obtained using statistical analysis, which is expressed by the following equation:

$$q = 0.7228 \cdot p + 7.6525 \quad (5.3)$$

The trend line fits well with the data points since the correlation parameter R^2 is as much as 0.98. In the p - q coordinates, the uniaxial compressive loading path can be expressed by:

$$q = 3 \cdot p \quad (5.4)$$

The intersection point of the trend line and the uniaxial compressive loading path represents the rubberised concrete compressive strength f_c . By solving the simultaneous equations: Equation 5.1, 5.2, 5.3 & 5.4, the rubberised concrete compressive strength f_c was obtained, which is 10.1 MPa.

Table 5.6 Stress state of rubberised concrete at peak compressive load

Specimen No.	Confining pressure	Vertical pressure	p	q
			0	0
RR1	0.5	9.7	3.6	9.2
RR2	5.0	21.9	10.6	16.9
RR3	10.0	29.2	16.4	19.2
RR4	15.1	39.5	23.2	24.5
RR5	20.0	48.8	29.6	28.7

In the plasticity-based material model developed for passively confined concrete, the yield surface function proposed by Lee and Fenves (1998) was used. As is

deduced in section 4.1, the compressive meridian of the yield surface function can be expressed by:

$$\left(\frac{1}{3}\gamma + 1\right)q - (\gamma + 3\alpha)p = (1 - \alpha)\sigma_c \quad (5.5)$$

The parameter σ_c represents the compressive strength; therefore, the value of 10.1 is in accordance with the stress state of actively confined concrete under peak compressive load. The parameters α and γ , which control the shape of the yield surface, were obtained by curve fitting the data points plotted in Figure 5.5. When $\alpha=0.12$ and $\gamma=0.478$, the compressive meridian of the yield surface complies with the trend line in Figure 5.5.

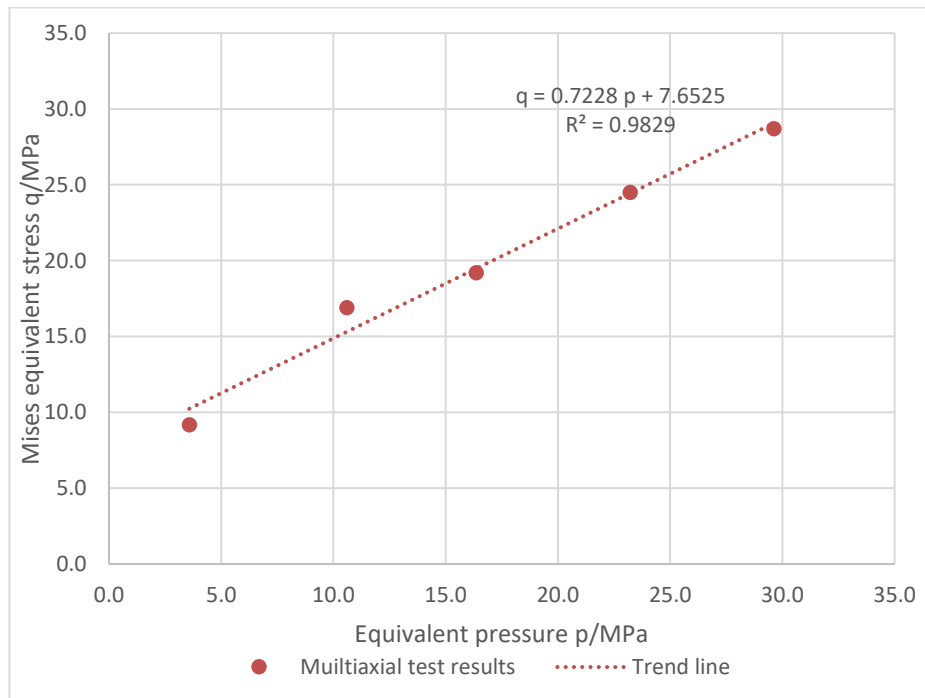


Figure 5.5 Trend line of test results in p-q coordinate

In the experimental tests on rubberised concrete with active confinement, loading was applied through two steps:

1. Applying hydrostatic pressure.
2. Increasing displacement in the vertical direction while keeping lateral stress constant.

Elastic constant of rubberised concrete tangent module (E_t) and Poisson's ratio (ν_t) were determined in the second step using the following equations:

$$E_t = \frac{\Delta\sigma_z}{\Delta\varepsilon_z} \quad (5.6)$$

$$v_t = -\frac{\Delta\varepsilon_x + \Delta\varepsilon_y}{2 \cdot \Delta\varepsilon_z} \quad (5.7)$$

As is illustrated in Figure 5.6 and Figure 5.7, the history of E_t and v_t were plotted respectively against the normalised vertical stress, which is the vertical stress σ_z divided by its peak value $\sigma_{z,max}$.

For the specimens with less confining pressure, RR1 and RR2, the tangent module remains constant initially followed by a decreasing trend with the increase of σ_z . Tangent module represents the slope of the stress-strain curve of ε_z - σ_z . Therefore, when the compressive load was small, specimen RR1 and RR2 exhibited linear elastic behaviour. For specimen RR3, RR6 and RR5, σ_z is relatively large at the onset of the second step, 10, 15 and 20 MPa respectively. The tangent module of these three specimens decreases with the increasing σ_z , which indicates the stress state at the onset of the second step is not in the elastic range. Hence, Young's modulus, as one of the elastic constants E was taken as 7 GPa for further numerical modelling.

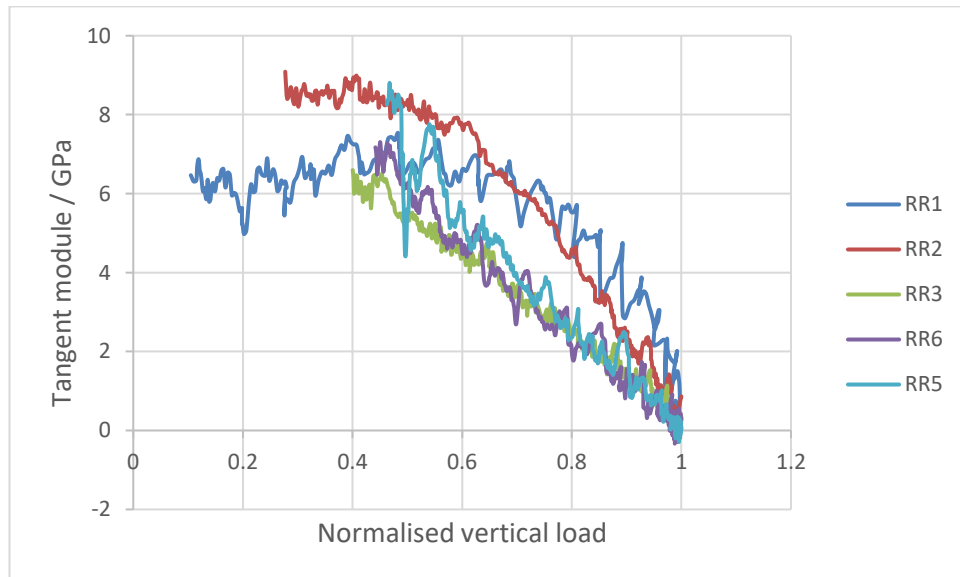


Figure 5.6 Tangent module history of rubberised concrete with constant confinement

As illustrated in Figure 5.7, v_t fluctuates at around 0.3 when the load is relatively small (i.e. no more than 0.4). Therefore, Poisson's ratio ν , as one of elastic constants

in the numerical material model, was identified as 0.3 of rubberised concrete, which is much higher than that of conventional concrete.

With increasing compressive load, v_t gradually increases. When the compressive stress σ_z exceeds 80% of its peak value $\sigma_{z,max}$, v_t of specimen RR1 with little confining pressure soars, which indicates a dramatic lateral expansion; on the contrary, with confining pressure no less than 5 MPa, the lateral expansion of the other four specimens is well controlled.

It can also be observed that when the stress state is close to the failure surface (i.e. $\sigma_z/\sigma_{z,max} \approx 1$), v_t is affected by the constant confining pressure (σ_l); the more σ_l applied to rubberised the concrete specimen, the less v_t . Hence, in the material model of rubberised concrete, the parameter that controlled dilation should be related to confining pressure.

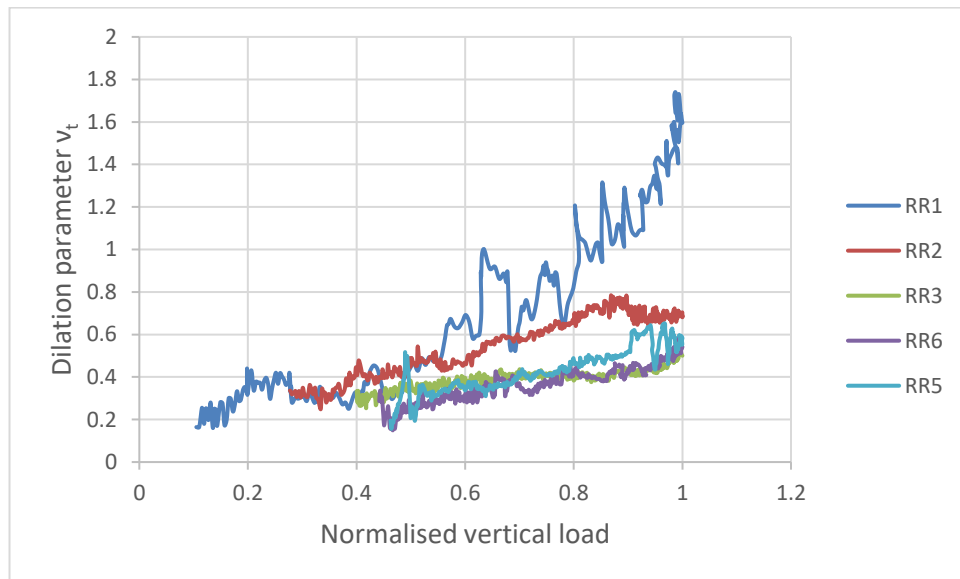
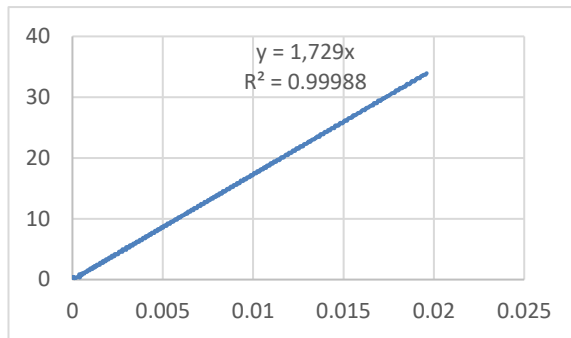


Figure 5.7 History of dilation parameter v_t

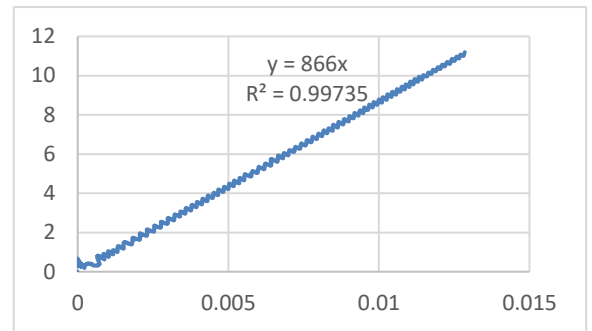
5.3.2 Passive confinement

The passive confinement applied to rubberised concrete was done through a control program in Mac^{2T}. To evaluate the effectiveness of the program, the history of the confining pressure (σ_l) and the lateral expansion (ϵ_l) was investigated. As illustrated in Figure 5.8, σ_l is plotted against ϵ_l . A linear regression analysis of σ_l and ϵ_l was conducted for all rubberised concrete specimens with passive confinement.

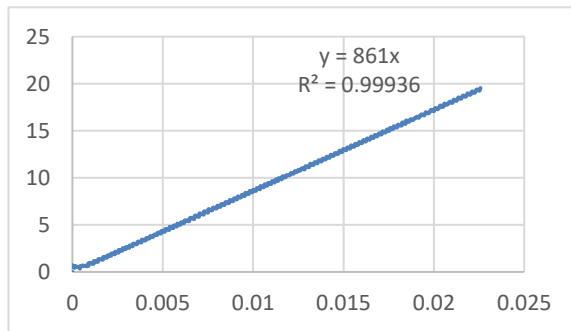
The analysis results, in the form of linear regression function and regression parameter R^2 , are listed in Figure 5.8.



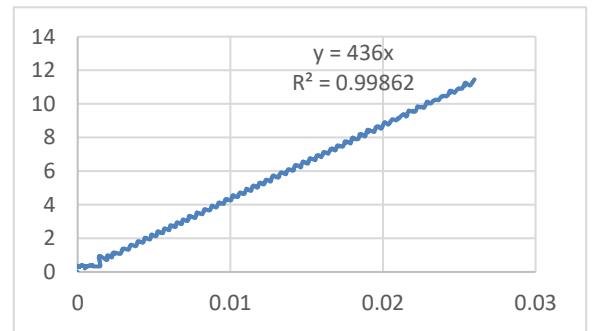
RP1



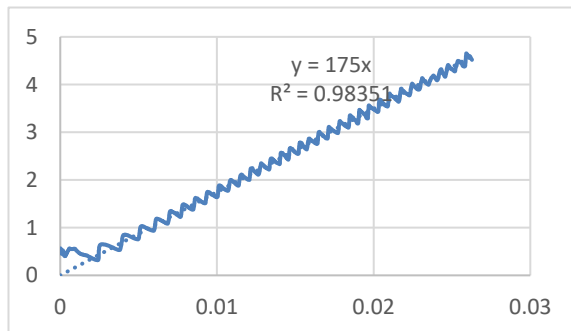
RP2



RP3



RP4



RP5

Figure 5.8 Evaluation of the control program for passive confinement

The regression parameter R^2 for all specimens is close to 1, which indicates the linear function, as the result of regression analysis, fits well to the data points. The slope of the linear function, which represents the actual confining stiffness applied to the specimen, was compared to the one specified previously to the tests as illustrated in Table 5.7. In general, the difference between the specified and the actual confining stiffness is no more than 1.5%. Hence, it can be concluded that

passive confinement was successfully applied to rubberised concrete specimens as desired.

Table 5.7 The specified and the actual confining stiffness

Specimen number	Confining stiffness (k) as input to Mat ^{2t} /MPa	Confining stiffness from regression analysis of the testing results	Difference
RP1	1748	1729	1.1%
RP2	874	866	0.9%
RP3	874	861	1.5%
RP4	437	436	0.2%
RP5	174.8	175	-0.1%

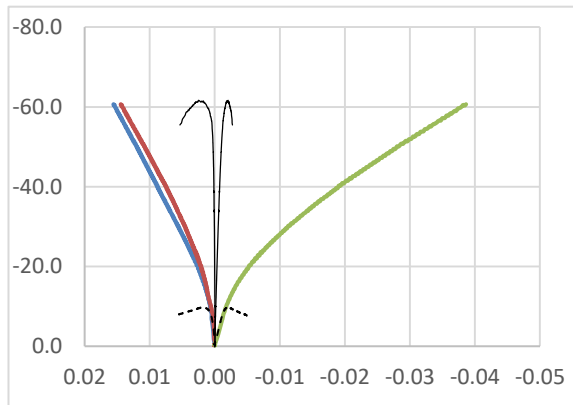
The test results of passively confined rubberised concrete under compressive load are illustrated in Figure 5.9, where the stress in the loading direction (σ_z) is plotted against strain (ϵ_x , ϵ_y and ϵ_z). The stress-strain curve of RR1, a rubberised concrete specimen with a tiny constant confining pressure of 0.5 MPa, is provided in Figure 5.9 as a benchmark.

Obviously, before the vertical stress σ_z exceeds the concrete strength f_c , the stress-strain curves of all specimen with passive confinement almost coincides with that of RR1, which implies the fact that passive confinement plays a negligible role when the compressive load is small.

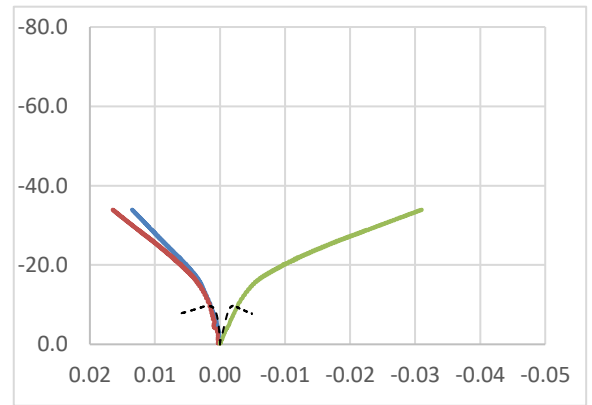
When the vertical stress σ_z exceeded rubberised concrete's compressive strength, dramatic lateral expansion occurred, and as a result, the confining pressure applied to rubberised concrete was effectively activated. No reduction of σ_z can be observed for the specimens with passive confinement, even for the case where the confining stiffness is as small as that of specimen RP5 (i.e. confining pressure $k=175$ MPa).

The stress-strain curve of a conventional concrete specimen (R1) subjected to uniaxial compression is plotted in Figure 5.9 a and compared with specimen RP1. At the same level of compression, rubberised concrete with passive confinement can

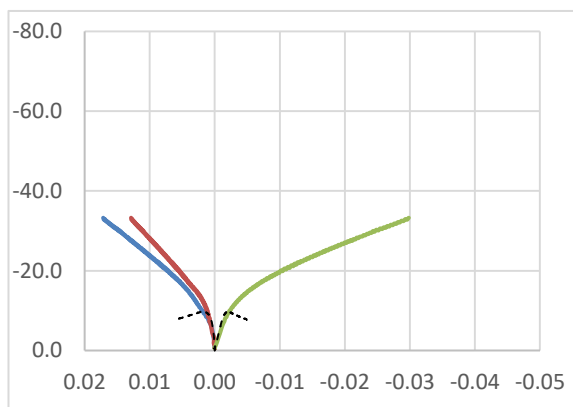
deform 10 times more than that of conventional concrete with little confining pressure, which can confirm the deformable capacity of FRP confined rubberised concrete.



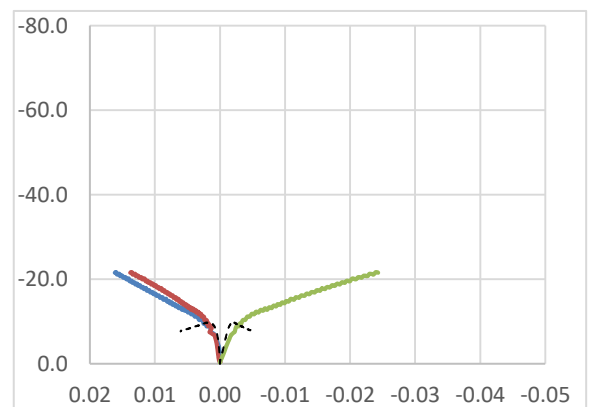
RP1 (2CFRP)



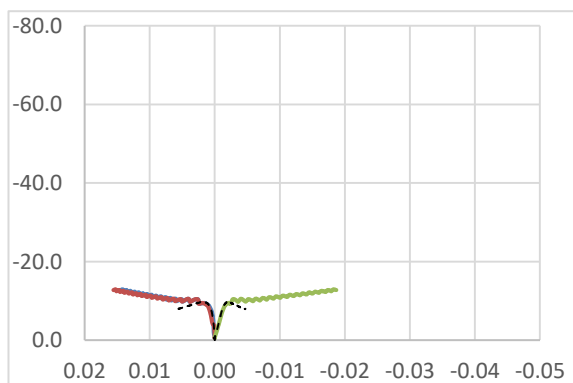
RP2 (1CFRP)



RP3 (1CFRP)



RP4 (0.5 CFRP)



RP5 (0.2CFRP)

Figure 5.9 Stress-strain of rubberised concrete with passive confinement

The loading path of all the tests is also plotted in Figure 5.10. As can be seen, the passively confined rubberised concrete specimens seem in possession of a large variability of strength when compared to the failure surface obtained from compressive tests of rubberised concrete specimens with constant confining pressure. The specimen RP1 exhibits a larger compressive strength compared to the other specimens since its loading path is located outside of that of the others, as illustrated in Figure 5.10.

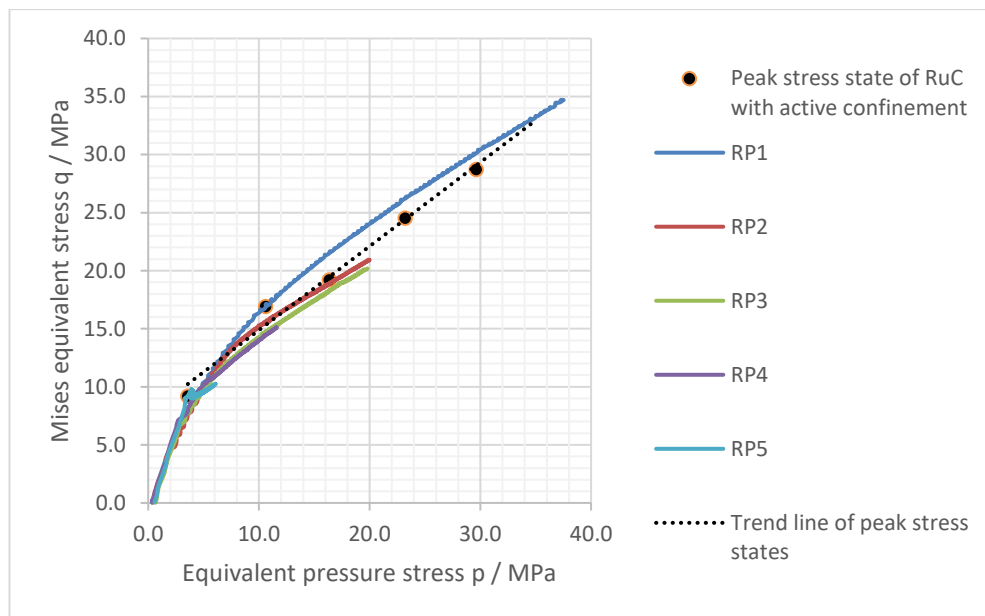


Figure 5.10 Loading path of rubberised concrete with passive confinement

Extensive previous research has confirmed the correlation between the rubber content and the strength of rubberised concrete. The more rubber content the specimen contains, the less compressive strength it exhibits. Therefore, the variability of rubberised concrete strength might result from the various rubber content within the specimens.

Before having been tested, the density of all the rubberised concrete specimens was evaluated, the results of which are listed in Table 5.8. The density of specimen RP1 was found to be higher than that of other specimens. The density of rubber particles – i.e. 800 KG/m³ (Samar et al., 2016) – was found to be much lower than for other concrete components (e.g. mineral aggregates). A higher specimen density

indicates a lower rubber content, which could be the reason why specimen RP1 had a higher compressive strength compared to its counterparts.

Table 5.8 Density of rubberised concrete specimen

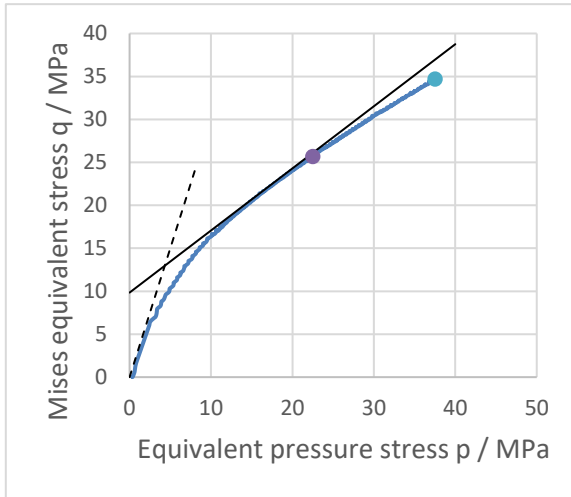
<i>Specimen</i>	<i>Density (KG/m³)</i>
<i>RP1</i>	1874
<i>RP2</i>	1837
<i>RP3</i>	1823
<i>RP4</i>	1828
<i>RP5</i>	1831

To identify the failure pattern of rubberised concrete with passive confinement, the loading paths of the tests are plotted in Figure 5.11 and were compared with the uniaxial loading path and the compressive meridian of failure surface. According to the previous discussion the parameters α and γ which control the shape of the failure surface are equal to 0.12 and 0.478, respectively. Then the compressive meridian of failure surface can be expressed as follows:

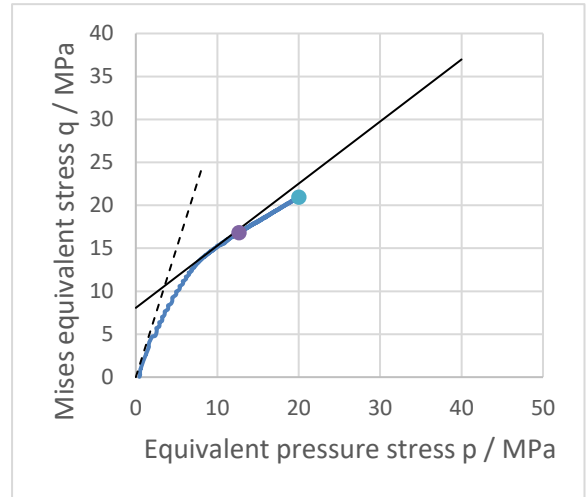
$$1.159 \cdot q - 0.838 \cdot p = 0.88 \cdot f_c \quad (5.8)$$

According to the experimental observation on conventional concrete, the passive lateral confinement prevents the failure of concrete from compressive loading, and the corresponding loading path of concrete is tangential to its compressive meridian of the failure surface. With passive confinement, rubberised concrete is expected to follow a similar loading path when subjected to the compressive load.

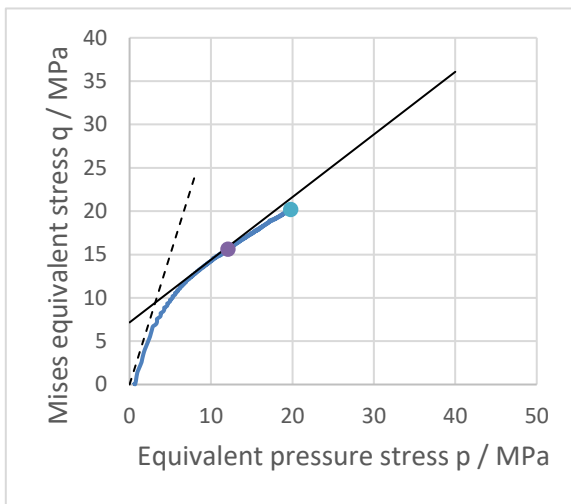
Since the rubberised concrete exhibited strength variability, the parameter f_c in Equation 5.8 that represents the rubberised concrete strength had to be adjusted for different tests, such that the compressive meridian of failure surface was at a tangent to the loading path of rubberised concrete with passive confinement. Through a trial and error process, f_c for each test was determined and the corresponding compressive meridian of the failure surface is plotted as a solid line (see Figure 5.11)



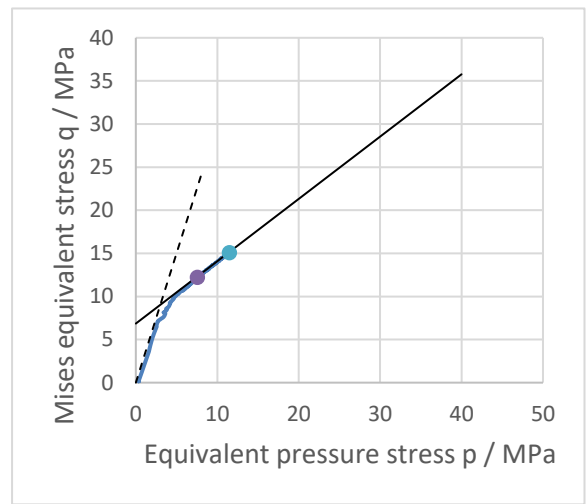
RP1 2CFRP $f_c=13.0$



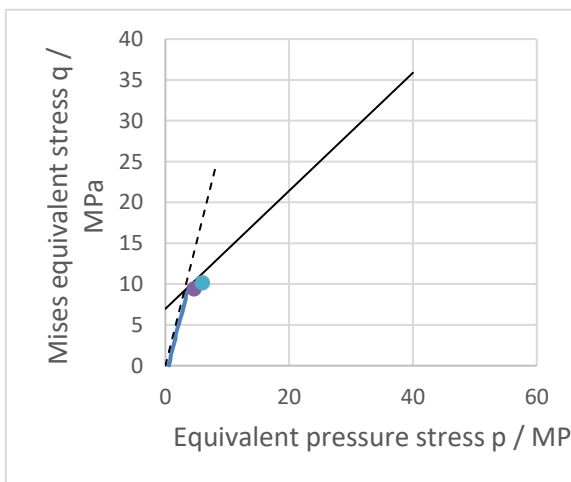
RP2 1CFRP $f_c=10.6$



RP3 1CFRP $f_c=9.4$



RP4 0.5CFRP $f_c=9.0$



RP5 0.2CFRP $f_c=10.3$

- Loading path of passively confined rubberised concrete
- Failure surface
- - - Uniaxial loading path
- Stress state at lateral strain of 0.008
- Stress state at lateral strain of 0.015

Figure 5.11 Loading path of rubberised concrete with passive confinement

As illustrated in Figure 5.11, the rubberised concrete followed the uniaxial loading path initially. With the increase of compressive loading, the stress state of rubberised concrete approached its failure surface. The manner in which the passively confined rubberised concrete approached its failure surface was different to that of the passively confined conventional concrete.

For the conventional concrete, the confining pressure applied to it was negligible until its stress state was on the failure surface, which was also the onset of unstable cracking. The dramatic lateral expansion due to the unstable cracking effectively activated the passive confinement, which prevented the concrete from failure and kept its stress state on the failure surface as the load increased. As a result, the loading path of conventional concrete was strictly along the uniaxial loading path before it moved on the failure surface, as shown in Figure 3.21.

For the passively confined rubberised concrete, especially with a high level of confining stiffness, its loading path deviated from uniaxial loading path far before the stress state was on the failure surface. That is, the confining pressure was effectively activated in advance. Hence, dramatic lateral expansion of rubberised concrete under compressive load occurred earlier compared to its counterpart without any rubber content.

With increasing compressive load, the loading path became tangent to the failure surface, and then it moved along the failure surface as a perfectly plastic material. As has been found in the experimental tests on passively confined conventional concrete, there is a limit to its perfectly plastic behaviour. The loading path moved away from the failure surface when the lateral strain of concrete exceeded 0.008. Therefore, the stress state of the rubberised concrete specimen at the lateral strain of 0.008 and 0.015 was significant, as illustrated in Figure 5.11.

Almost all rubberised concrete specimens exhibited similar behaviour as that of conventional concrete. The stress state corresponding to the lateral strain of 0.008 represents the end of perfectly plasticity and the onset of softening. Only specimen RP4 exhibited perfectly plastic behaviour when the lateral strain was as much as

0.015, as its stress state was always on the failure surface. This might be due to the material's variability.

In summary, the response of rubberised concrete with passive confinement under compressive load consists of 4 phases:

1. Following the uniaxial loading path and exhibiting linear elastic behaviour;
2. Deviating from the uniaxial loading path and behaving as plastic hardening material;
3. Moving on the failure surface and behaving as perfectly plastic material;
4. Moving away from the failure surface and becoming soft due to significant lateral expansion.

5.4 Summary

The following generalisations can be made based on the results analysed in this Chapter. Firstly, rubberised concrete exhibits weak compressive strength compared to conventional concrete. Secondly, passive confinement seems likely to be necessary for structural components composed of rubberised concrete. With passive lateral confinement, compressive failure of rubberised concrete can be prevented. It has also been observed that at the same level of compressive loading, rubberised concrete exhibits larger lateral expansion, which could effectively activate passive lateral confinement.

In general, the failure mechanism of passively confined rubberised concrete is similar to that of conventional concrete. With passive confinement, rubberised concrete moves along with the failure surface when subjected to a compressive load and can become soft when the lateral expansion exceeds 0.008 as its stress state moves away from the failure surface. In addition, at the same level of compressive loading, the deformation in the loading direction of rubberised concrete with passive confinement can be 10 times larger than the conventional concrete, which might facilitate its use in novel structural applications.

It is worth mentioning that the rubberised concrete specimens exhibited relatively large variability compared to their counterpart, conventional concrete. The

different rubber content among specimens might be attributed to the variability of mechanical behaviour.

6 Modelling of rubberised concrete with passive confinement

According to the observations made from the multiaxial tests on rubberised concrete, the mechanical behaviour of rubberised concrete is similar to that of conventional concrete. Under compressive load, passively confined rubberised concrete moved along its failure surface in the stress space. Therefore, rubberised concrete can be assumed as a perfectly plastic material in numerical simulations. It has also been observed that rubberised concrete experiences strength reduction when the lateral expansion is greater than 0.008, as its stress state moves away from the failure surface. Therefore, this needs to be taken into account in numerical modelling.

A plasticity-based material model has been proposed in Chapter 4 which has been proved capable of representing the compressive behaviour of concrete with passive confinement. Therefore, the numerical modelling in this Chapter for rubberised concrete uses same framework.

In this Chapter, a description of the plasticity-based material model calibration for rubberised concrete is provided. Then, the results from the material model having been introduced to finite element software ABAQUS are presented. This is followed by a description of the experimental tests using Mac^{2T} which were numerically simulated. Finally, a comparison of the numerical results to their experimental counterpart as the verification of material modelling of rubberised concrete concludes the chapter.

6.1 Plasticity-based material model of passively confined rubberised concrete

The plasticity-based material model proposed in Chapter 4 was aimed at capturing the mechanical behaviour of passively confined concrete under compressive loads. As discussed in Chapter 4, the plasticity-based material model consists of three elements: yield surface function, hardening rule and plastic potential function. In the proposed material model, the yield surface function was provided Lee and Fenves (1998), while the Drucker-Prager function was taken as the plastic potential

function. The hardening rule relates the hardening parameter to the equivalent plastic strain and lateral strain in order to simulate the limited perfectly-plastic behaviour of rubberised concrete. In this section, the material model calibration for rubberised concrete is described.

6.1.1 Yield surface function

The yield surface function proposed by Lee and Fenves (1998) can be expressed as follows:

$$f(\sigma_{ij}) = \frac{1}{1 - \alpha} \cdot (q - 3\alpha p + \beta \langle \sigma_{max} \rangle - \gamma \langle -\sigma_{max} \rangle) - \sigma_c \quad (6.1)$$

$$\beta = \frac{\sigma_c}{\sigma_t} (1 - \alpha) - (1 + \alpha)$$

The parameters α and γ that control the shape of the failure surface have been determined in section 5.3 – 0.12 and 0.478 respectively – such that the failure surface complied with the multiaxial test results of rubberised concrete with active confinement. Since the plastic-hardening was assumed to be in an isotropic pattern, the shape of the yield surface remained unchanged. Therefore, the parameters α and γ were kept constant.

6.1.2 Hardening rule

According to the experimental observation from Chapter 5, under monotonic compressive loading, passively confined rubberised concrete experienced elastic behaviour initially, followed by plastic hardening. Once it reached the failure surface, it moved along it as a perfectly plastic material. After the lateral expansion of rubberised concrete exceeded a certain level (strain of 0.008), the rubberised concrete moved away from the failure surface. One typical loading path of passively confined concrete (specimen RP1) is illustrated in Figure 6.1.

The framework of hardening rule for conventional concrete, defined in Chapter 4, was used for the rubberised concrete. That is, the hardening parameter σ_c is a function with respect to the equivalent strain ε_c^{pl} and the lateral strain ε_l , expressed as follows:

$$\sigma_c = \begin{cases} \left(\frac{0.3f'_c}{\varepsilon_{cp1}} \varepsilon_c^{pl} + 0.7f'_c \right) \cdot d(\varepsilon_l), & \varepsilon_c^{pl} < \varepsilon_{cp1} \\ f'_c \cdot d(\varepsilon_l), & \varepsilon_c^{pl} \geq \varepsilon_{cp1} \end{cases} \quad (6.2)$$

where

f'_c is the rubberised concrete uniaxial compressive strength;

ε_{cp1} is the parameter corresponding to the equivalent plastic strain when rubberised concrete initially reach its failure surface; and

$d(\varepsilon_l)$ is the parametric function with respect to lateral strain ε_l .

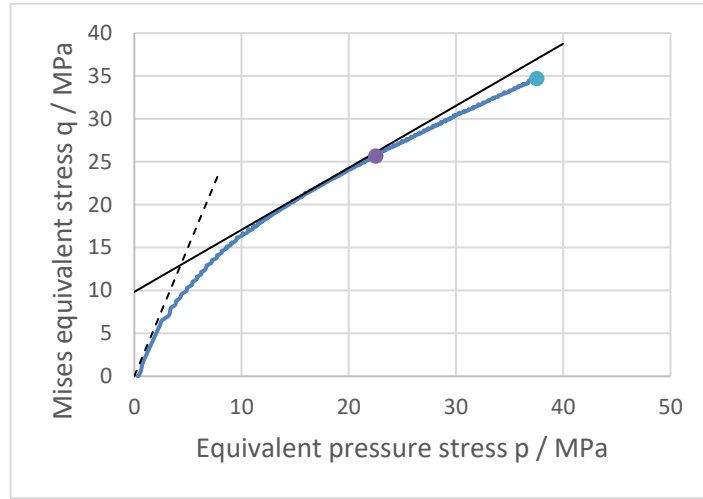


Figure 6.1 Typical loading path of passively confined concrete

By dividing both sides with f'_c , Equation 6.2 becomes:

$$\sigma_c/f'_c = \begin{cases} \left(\frac{0.3}{\varepsilon_{cp1}} \varepsilon_c^{pl} + 0.7 \right) \cdot d(\varepsilon_l), & \varepsilon_c^{pl} < \varepsilon_{cp1} \\ d(\varepsilon_l), & \varepsilon_c^{pl} \geq \varepsilon_{cp1} \end{cases} \quad (6.3)$$

Parametric function $d(\varepsilon_l)$ represents the strength reduction of rubberised concrete as the result of lateral expansion. As observed in experimental tests, when lateral strain was no more than 0.008, rubberised concrete could move along its failure surface. In other words, the rubberised concrete exhibited no strength reduction. Therefore, under this circumstance, the value of $d(\varepsilon_l)$ was taken as 1. For $\varepsilon_l \leq 0.008$, Equation 6.3 then reduces to the following:

$$\sigma_c/f_c' = \begin{cases} \frac{0.3}{\epsilon_{cp1}} \epsilon_c^{pl} + 0.7, & \epsilon_c^{pl} < \epsilon_{cp1} \\ 1 & \epsilon_c^{pl} \geq \epsilon_{cp1} \end{cases} \quad (6.4)$$

Then, σ_c/f_c' is plotted against ϵ_c^{pl} , as illustrated in Figure 6.2.

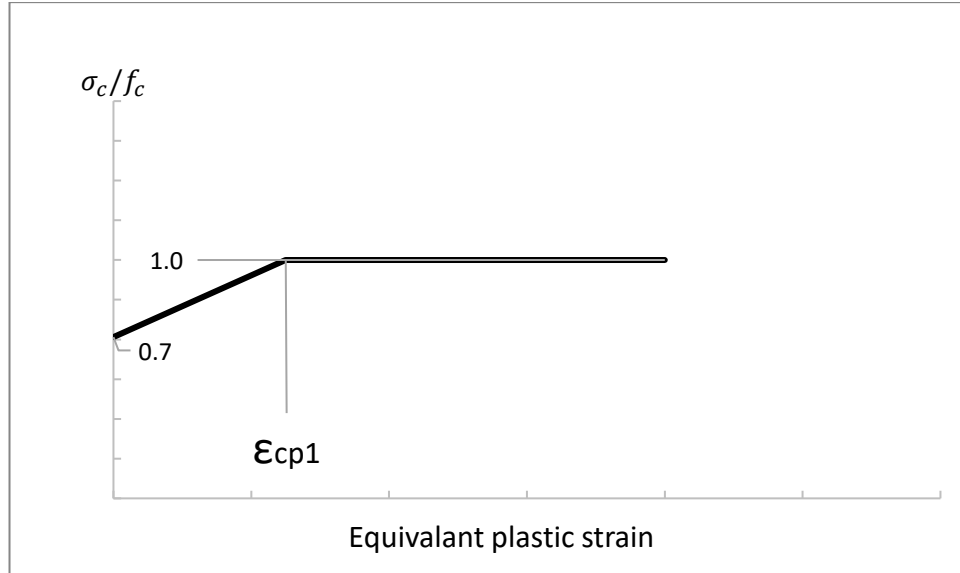


Figure 6.2 The relation between σ_c and ϵ_{cp1} at $\epsilon_l \leq 0.008$

It is worth mentioning that when the equivalent plastic strain exceeded ϵ_{cp1} and the rubberised concrete reached its failure surface, the hardening parameter σ_c was governed by parametric function $d(\epsilon_l)$, as illustrated in Figure 6.3.

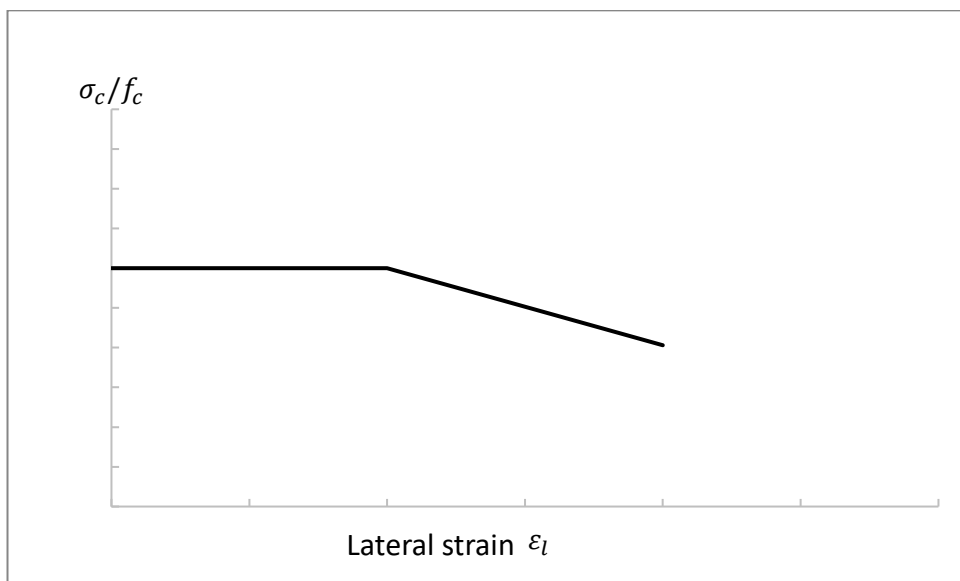


Figure 6.3 The relation between σ_c and ϵ_l

Following this, parameter ε_{cp1} and parametric function $d(\varepsilon_l)$ had to be determined by fitting the curves plotted in Figure 6.2 and Figure 6.3 to those obtained in the experimental tests. For the scenario of all principal stresses in compression, the yield surface function Equation (6.1) can be simplified and expressed as follows:

$$\left(\frac{1}{3}\gamma + 1\right)q - (\gamma + 3\alpha)p = (1 - \alpha)\sigma_c \quad (6.5)$$

σ_c is the only hardening parameter that controls the evolution of the yield surface.

Substituting $\alpha=0.12$ and $\gamma=0.478$ into Equation 6.5 provides:

$$1.159q - 0.838p = 0.88\sigma_c \quad (6.6)$$

Therefore, the hardening parameter σ_c corresponding to any stress state can be calculated by Equation 6.6. For the cases of passively confined concrete under compressive load, the equivalent plastic strain ε_c^{pl} is the plastic strain in the loading direction (ε_z^p), which can be calculated using the following equation:

$$\varepsilon_c^{pl} = \varepsilon_z^p = \varepsilon_z - \frac{1}{E}(\sigma_z - 2\nu\sigma_l) \quad (6.7)$$

where

σ_z and ε_z are stress and strain in the loading direction;

σ_l is the stress in the lateral direction, average of σ_x and σ_y .

By substituting the reading of stress and strain by Mac^{2T} into Equation 6.7, equivalent plastic strain ε_c^{pl} can be evaluated. In order to determine parameters in Equation 6.2, σ_c was normalised by rubberised strength f_c' and plotted against equivalent plastic strain ε_c^{pl} and lateral strain ε_l respectively, as is illustrated in Figure 6.4 and Figure 6.5. The fitting curves were also plotted. Hence, the parameter for rubberised concrete could be taken as 0.004; i.e. when plastic strain in the compressive loading direction was 0.004, rubberised concrete reached its failure surface. The parametric function $d(\varepsilon_l)$ is expressed as follows:

$$d(\varepsilon_l) = \begin{cases} 1, & \varepsilon_l < 0.008 \\ -28.6 \cdot \varepsilon_l + 1.229, & \varepsilon_l \geq 0.008 \end{cases} \quad (6.8)$$

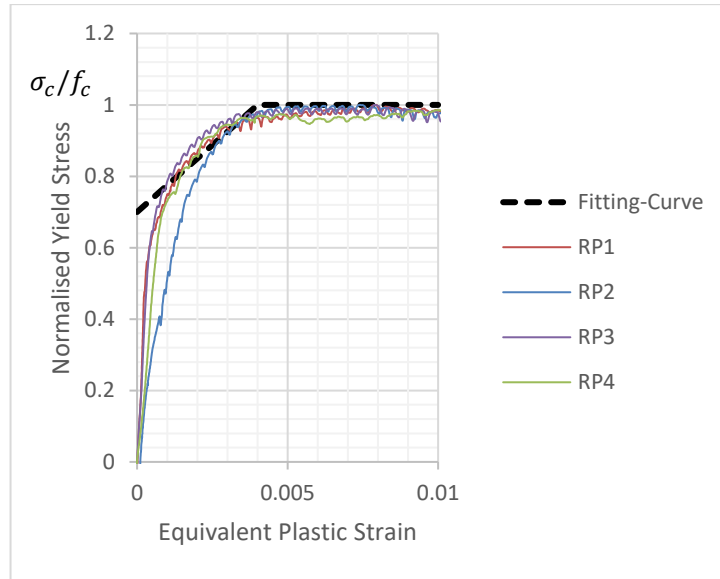


Figure 6.4 Relation between ε_c^{pl} and σ_c from experimental tests

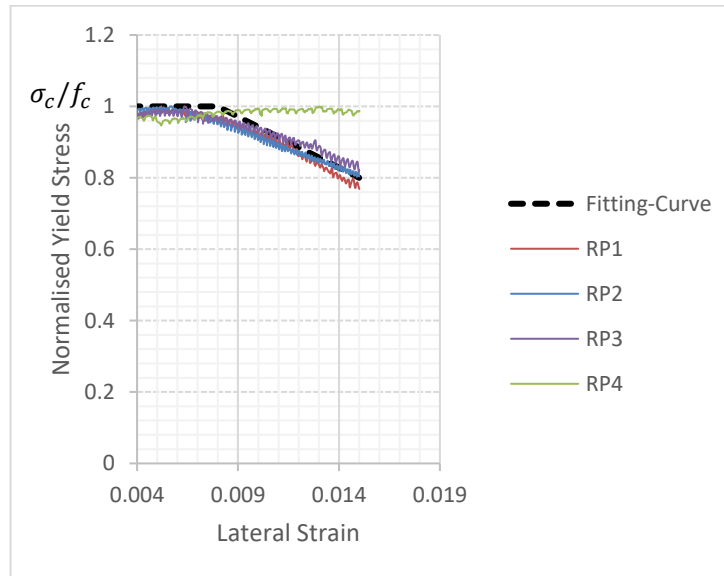


Figure 6.5 Relation between ε_l and σ_c from experimental tests

6.1.3 Plastic flow rule

In the proposed material model, the Drucker-Prager function was taken as the plastic flow potential, with the only parameter dilation angle φ :

$$g(p, q) = q - \tan\varphi \cdot p \quad (6.9)$$

Therefore, this section shows the process of identification of parameter φ . As deduced in section 4.1.3, the dilation angle φ represents the ratio of plastic strain increment in the loading and the lateral direction, and can be expressed as follows:

$$\varphi = \tan^{-1} \left(\frac{3}{2} \cdot \frac{2 \cdot \left(-\frac{d\varepsilon_2^p}{d\varepsilon_1^p} \right) - 1}{\left(-\frac{d\varepsilon_2^p}{d\varepsilon_1^p} \right) + 1} \right) \quad (6.10)$$

According to the experimental observation on rubberised concrete with active confinement (Figure 5.7), its dilation property is dependent on the confining pressure applied to it. Therefore, dilation parameter φ is believed to be a parametric function with respect to confining pressure σ_l .

In the process of testing, strain in all three directions (ε_1 , ε_2 and ε_3) was read by Mac^{2T}. From this, the plastic components of the strain could be calculated as follows:

$$\varepsilon_1^p = \varepsilon_1 - \frac{1}{E} (\sigma_1 - 2\nu\sigma_2) \quad (6.11.a)$$

$$\varepsilon_2^p = \varepsilon_2 - \frac{1}{E} [(1 - \nu)\sigma_2 - \nu\sigma_1] \quad (6.11.b)$$

where Young's modulus E and Poisson's ratio ν was determined in the previous section, the values of which are 7 GPs and 0.3, respectively.

Dilation angle φ can be calculated by substituting Equation 6.11 into Equation 6.10. Dilation angle φ of rubberised concrete specimens (RP1, RP3, RP4 and RP5) with different level of confining stiffness were then plotted against σ_l , as illustrated in Figure 6.6.

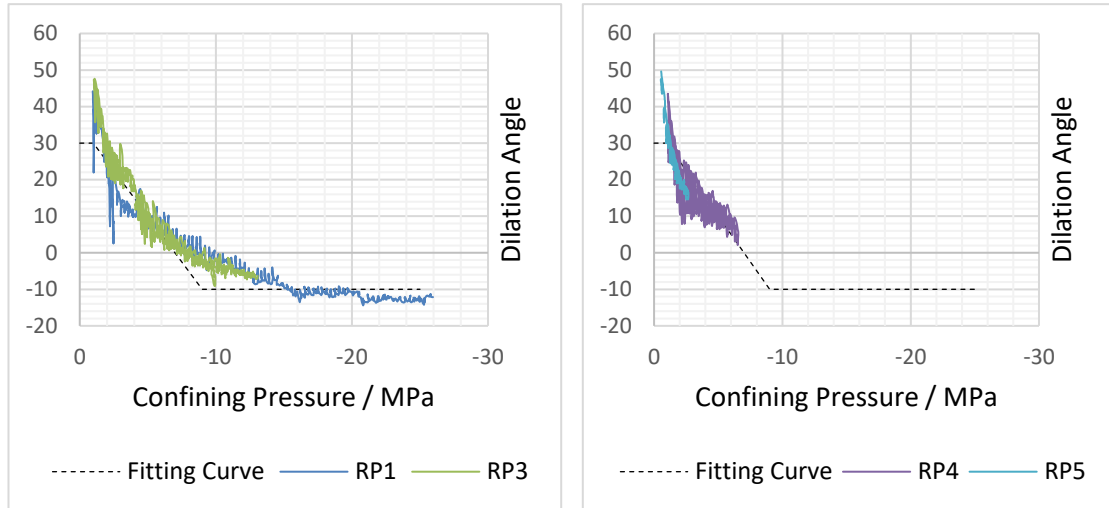


Figure 6.6 The history of dilation angle φ plotted against confining pressure σ_l

As has been found in conventional concrete, the dilation angle decreased with the increasing confining pressure and became stable when the confining pressure exceeded a certain level.

According to the theory of plasticity, the relationship between plastic volumetric strain increment $d\varepsilon_v^p$ and dilation angle φ can be expressed as follows:

$$d\varepsilon_v^p = d\lambda \cdot \tan\varphi \quad (6.12)$$

That is, a positive value of φ indicates the trend of swelling, while a negative one indicates the trend of compacting. For conventional concrete, the minimum value of dilation angle observed in the experimental tests was no less than 0 – the trend of compacting could not be observed for conventional concrete. However, for specimen RP1 and RP3, the dilation angle eventually became negative.

It is worth mentioning that all the tests stopped when the lateral expansion of the specimen reached 0.015. For specimens RP1 and RP3 with relatively large confining stiffness, the confining pressure reached 26 and 14 MPa respectively. Compared to the unconfined rubberised concrete strength (around 10 MPa), such confining pressures specimen RP1 and RP3 experienced are very large. Under such a high

level of lateral confinement, the rubberised concrete tended to compact. The cracking as a result of vertical loading was limited to an extent by the huge lateral confining pressure.

The parametric function of dilation angle was obtained by a curve fitting process, and the fitting function is in the form of broken line function as follows:

$$\varphi = \begin{cases} 30 & \sigma_l \geq -1 \\ -5 \cdot \sigma_l + 35 & -1 > \sigma_l \geq -9 \\ -10 & -9 > \sigma_l \end{cases} \quad (6.13)$$

6.2 Implementation of the proposed model in ABAQUS

In the previous section, the material model for passively confined concrete was calibrated for rubberised concrete. Since the yield surface function and the plastic potential function are the same as defined in the ABAQUS CDP material model, the proposed material model was easily imported into ABAQUS.

The hardening parameter σ_c and dilation angle φ are a parametric function with respect to field variables. Therefore, user subroutine option USDFLD in ABAQUS was needed, whereby the field variables could be redefined and related to material parameters. Two field variables were defined for the rubberised concrete material model, as listed in Table 6.1.

Table 6.1 Material-properties-dependent field variables

	<i>Physical interpretation</i>	<i>Formula</i>
<i>Field 1</i>	Confining pressure	$(\sigma_2 + \sigma_3)/2$
<i>Field 2</i>	Lateral expansion	$(\varepsilon_2 + \varepsilon_3)/2$

Young's modulus and Poisson's ratio had to be defined in CDP as elastic constants. For the rubberised concrete tested in the lab, these two constants were 7 GPa and 0.3 respectively.

The parameters of yield surface function α and γ were calibrated for rubberised concrete in the previous section, equal to 0.12 and 0.4783 respectively. However, ABAQUS received f_{b0}/f_{c0} and K as the parameters in charge of the shape of yield

surface, related to α and γ through Equation 6.14. Therefore, CDP yield surface parameters f_{b0}/f_{c0} and k for rubberised concrete were calculated and are listed in Table 6.2.

$$\frac{f_{b0}}{f_{c0}} = \frac{\alpha - 1}{2\alpha - 1} \quad (6.14.a)$$

$$k = \frac{\gamma + 3}{2\gamma + 3} \quad (6.14.b)$$

Table 6.2 Parameters for the shape of the yield surface

f_{b0}/f_{c0}	k
1.149	0.6667

The hardening rule is defined by Equation 6.2 in section 6.1.2 for rubberised concrete, in which the hardening parameter is a parametric function with respect to equivalent plastic strain and lateral strain (field variable **Field 2**). Software ABAQUS is not capable of receiving the hardening rule in the form of parametric function; instead, it can only accept data points. Thus, linear interpolation was used by ABAQUS for the determination of the values between the data points. The crucial data points for rubberised concrete were calculated based on Equation 6.2, as are listed in Table 6.3.

Table 6.3 Data points imported into ABAQUS for hardening rule identification

Yield stress	Inelastic Strain	Field 2
$0.56 \cdot f'_c$	0	0.015
$0.8 \cdot f'_c$	0.004	0.015
$0.8 \cdot f'_c$	0.05	0.015
$0.7 \cdot f'_c$	0	0.008
f'_c	0.004	0.008
f'_c	0.05	0.008

where

f'_c represents the unconfined compressive strength of rubberised concrete.

In the developed material model, a Drucker-Prager type function was used as the plastic flow rule, in which dilation angle φ is a parametric function with respect to the field variable confining pressure.

The plastic flow rule in ABAQUS was identified in a similar fashion to the hardening rule. The crucial data points were calculated based on Equation 6.13. ABAQUS accepted these data points and conducted linear interpolation in order to determine the values between the data points.

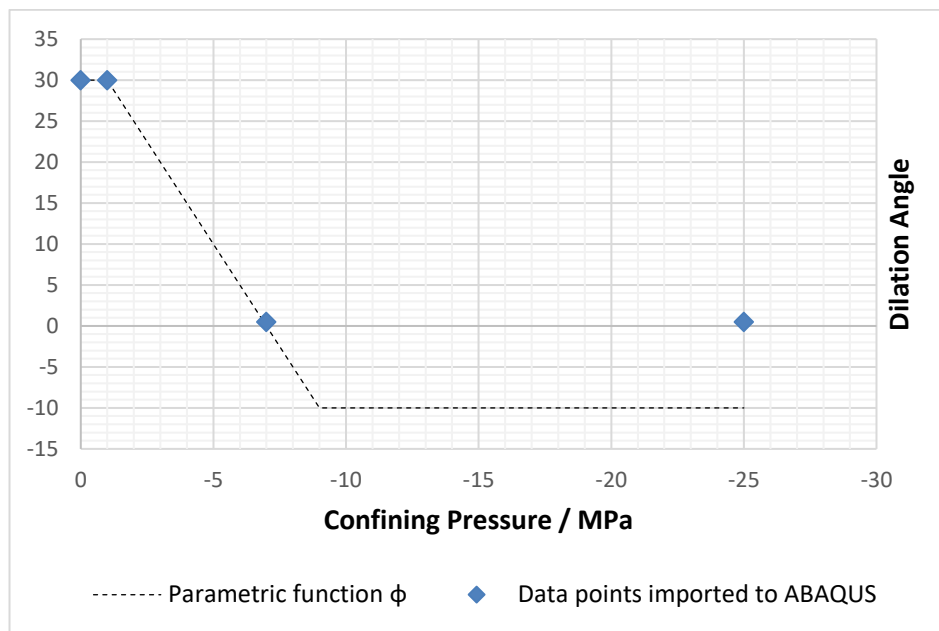


Figure 6.7 Comparison between data points and function $\varphi(\sigma_l)$

It is worth mentioning that a negative dilation angle could not be accepted by ABAQUS under the framework of the ABAQUS CDP material model. Thus, when the rubberised concrete was subjected to large lateral confining pressure, its compacting volumetric trend could not be precisely captured.

A compromise was made whereby the dilation angle was defined to be 0.5° for confining pressures exceeding 7 MPa. The data points imported to ABAQUS were then compared to the parametric function obtained in section 6.1.3, as illustrated in Figure 6.7. The error of numerical simulation due to such compromise is assessed in the following section.

6.3 Validation of the material modelling through ABAQUS

In this section, the results of the numerical simulation of experimental tests on passively confined rubberised concrete through ABAQUS are presented, making use of the material model defined in the previous sections. The numerical results are compared to those obtained from the experimental tests in order to verify the proposed material model for rubberised concrete.

Rubberised concrete specimens were simulated in ABAQUS through the deformable brick elements with reduced integration (C3D8R). The mesh of the rubberised concrete specimen is illustrated in Figure 6.8, with an element size of 10 mm. Since the material model was independent of element size, and uniform stress and strain distribution was expected, the mesh of the specimen did not affect the numerical results.

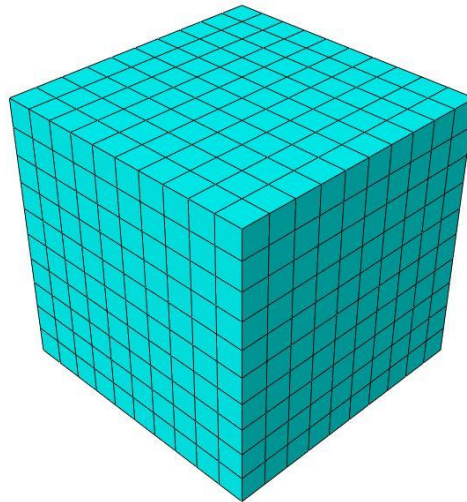


Figure 6.8 Mesh of the rubberised concrete specimen

Passive lateral confinement was applied to the rubberised concrete specimen through the rigid shell with the same mesh size, which was in contact with each side of the specimen in a frictionless manner. Rotational constrain was defined at the centre of the rigid shell and only translation in the direction perpendicular to the cubic specimen side was allowed. A spring was installed at the centre of each rigid shell in order to relate the confining pressure to rubberised concrete lateral

expansion. The confining stiffness σ_l/ε_l could be adjusted by setting the spring stiffness in ABAQUS.

There were four numerical simulations carried out with four different levels of lateral confining stiffness. The confining stiffness was the same as that defined in the experimental tests and is listed in Table 6.4. The numerical analysis results of rubberised concrete were then compared to their experimental counterparts and are presented here.

Table 6.4 Confining stiffness defined in numerical model

Numerical simulation No.	σ_l/ε_l MPa	Experimental tests specimen
B1	1748	RP1
B2	874	RP2 & RP3
B3	437	RP4
B4	175	RP5

The loading path of passively confined rubberised concrete as a result of the numerical simulation (red solid line) and its experimental counterpart (black solid line) were plotted and are shown in Figure 6.9. Clearly, the numerical simulation agrees well with the experimental tests. Therefore, the yield surface function and the hardening rule were correctly defined for the rubberised concrete.

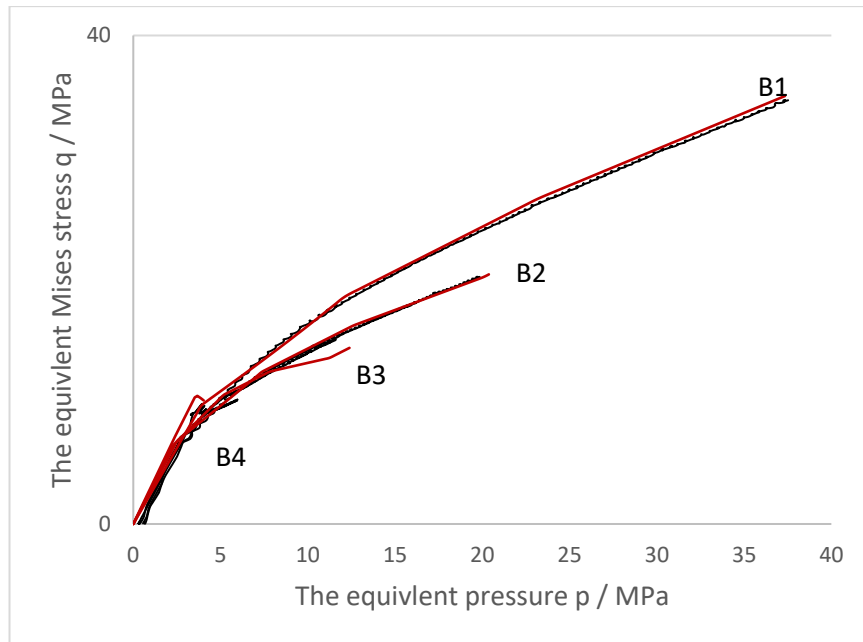


Figure 6.9 Loading path of RuC in the experimental and the numerical test

The stress and the strain were uniformly distributed in the concrete specimen according to the numerical simulation results. σ_1 and ε_1 represent the stress and the strain in the loading direction while σ_2 and ε_2 represent the stress and the strain in the lateral direction. The stress-strain curves of $\sigma_1 - \varepsilon_2$ and $\sigma_1 - \varepsilon_1$ which are plotted in Figure 6.10 (red solid lines) as the numerical simulation results, were compared with those of the experimental test results (black dashed lines). As discussed in Chapter 4, the accuracy of the $\sigma_1 - \varepsilon_2$ curves from numerical tests depends on whether the loading path of passively confined concrete could be correctly simulated. The numerical results of $\sigma_1 - \varepsilon_2$ agree well with their experimental counterparts.

In general, the $\sigma_1 - \varepsilon_1$ curves obtained from the numerical simulation are close to the experimental test results with the exception of B1. The plastic flow rule governs the relation between the strain in the loading direction (ε_1) and the strain in the lateral direction (ε_2). Since the lateral expansion of the passively confined rubberised concrete was correctly simulated by ABAQUS, the accuracy of the prediction of $\sigma_1 - \varepsilon_1$ curves depends on the correctness of the plastic flow rule.

In the numerical testing B1, a relatively large confining stiffness was applied. When the compressive load was high, a large confining pressure was activated. As has

been observed in the experimental tests, when subjected to large confining pressure, the rubberised concrete tended to compact. Under this circumstance, the parameter in the proposed plastic flow rule, dilation angle φ , was predicted to be negative. However, ABAQUS CDP material model could accept a φ value less than 0. Therefore, a compromise was made in the previous section. When the confining pressure exceeded 7 MPa, φ was taken as 0.5 instead of a negative value. As a result, the axial strain in B1 was underestimated when at a high level of confining pressure.

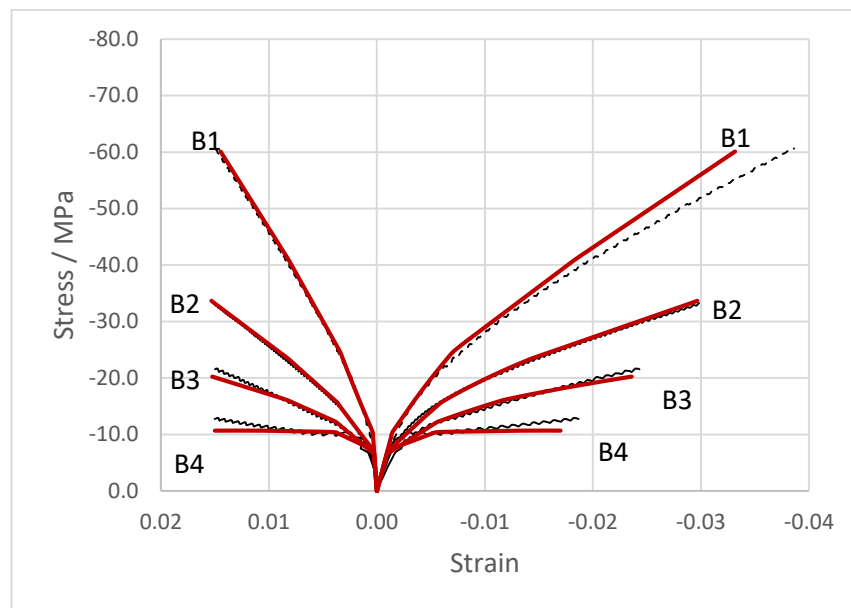


Figure 6.10 Stress-strain from the experimental and the numerical tests

6.4 Summary

In this Chapter, a material model for rubberised concrete has been proposed based on the failure mechanism of rubberised concrete. The behaviour of rubberised concrete in the stress space is well simulated by the proposed model. Moreover, the proposed model considers the dilation property, which is influenced by FRP confinement.

The material model used the framework of plasticity and was easily introduced into finite element software ABAQUS. The experimental tests on the rubberised concrete by Mac^{2T} were numerically simulated by ABAQUS. From this, it is obvious that the numerical results exhibit a good agreement to their experimental

counterparts. Hence, the proposed material model has been proven capable of simulating passively confined rubberised concrete under compressive loads.

7 Conclusions and Recommendations for future work

This study investigated the mechanical behaviour of rubberised concrete under lateral confinement. The research started with an experimental study on conventional concrete, in order to investigate the failure mechanism of FRP-confined concrete. Based on the observed failure mechanism, the mechanical behaviour of passively confined concrete has been modelled numerically. The experimental and numerical study on conventional concrete provided the methodology for the study of rubberised concrete with passive confinement. The objectives of the research are all accomplished, and the main conclusions from the previous chapter are reported below.

7.1 Main conclusion

From the experimental study on conventional concrete, it is concluded that:

- A hypothesis that under compressive load passively confined concrete behaves as perfectly plastic material is made using results from conventional concrete.
- The proposed hypothesis is validated through a novel use of a true tri-axial apparatus Mac^{2T}.
- Mac^{2T} is proven capable of physically simulate passive confinement to concrete.
- The behaviour of passively confined concrete under compressive load consists of three phases. Initially, it behaves as an unconfined one, as lateral confinement is not effectively activated. Once the load is approaching unconfined concrete strength, unstable cracks form in the concrete that activate FRP confinement. The lateral confining pressure is found keep in pace with increasing load, such that in the stress space of concrete moves along the failure surface. Therefore, concrete initially exhibits the behaviour as of a perfectly plastic material.
- There is a limit to the perfect plasticity. With the lateral expansion exceeding the strain of 0.008, the yielding surface in the stress space starts to compact. As a result, a third phase of softening of concrete occurs.

From the numerical study on conventional concrete, it is concluded that:

- A plasticity-based material model for conventional concrete with passive confinement is developed according to the experimental observation.
- The proposed material model is capable of representing the behaviour of passively confined concrete in the stress space. Moreover, the proposed material model considers the effect of FRP confinement on the dilation properties of concrete.
- A MATLAB program that incorporates the proposed material model is developed to generate the stress-strain relation of passively confined concrete, which can be used in the design-oriented analysis.
- The proposed material model can be introduced into nonlinear finite element software, such as ABAQUS, whereby a mechanical problem with complicated boundary condition can be solved.

From the experimental study on rubberised concrete, it is concluded that:

- Rubberised concrete exhibits weak compressive strength compared to conventional concrete; therefore, passive confinement is necessary for the structural components made up with rubberised concrete. With passive lateral confinement, the compressive strength of rubberised concrete can be increased to the level of conventional concrete.
- The failure mechanism of passively confined rubberised concrete is similar to that of conventional concrete. With passive confinement, rubberised concrete moves along the failure surface when subjected to compressive loads. It also softens when the lateral expansion is larger than 0.008, as its stress state moves away from the failure surface.
- At the same level of compressive loading, the deformation in the loading direction of rubberised concrete with passive confinement can be ten times larger than that of the conventional concrete, which makes it feasible for some novel structural applications, e.g. integral/semi-integral bridges and bridge bearings.

- Rubberised concrete specimens exhibit larger variability compared to conventional concrete. There is a strong correlation between specimen density and strength, and this may partly explain its variability.

Following the numerical study on rubberised concrete, it is concluded that:

- A plasticity-based material model for rubberised concrete with passive confinement is proposed which simulate well the behaviour of rubberised concrete in the stress space.
- The material model was incorporated in ABAQUS with good results.

7.2 Recommendations for the future work

Multiaxial experimental apparatus Mac^{2T} is proved capable of physically simulate passive confinement to concrete. The loading path of passively confined concrete under compressive load overlaps with the compressive meridian, which verifies that with passive confinement concrete initially behaves as a perfectly plastic material.

However, it is worth mentioning that the compressive meridian of failure surface is comparable to the loading path of passively confined concrete, as the principal stresses in the lateral direction are equal to each. If the confining stiffness in the x and the y direction is not identical and the principal stresses in the lateral direction are not equal, it is not certain if the loading path of passively confined concrete will still be on the failure surface. Hence, more experimental tests are needed to rigorously validate the proposed hypothesis. The same applies to unequal strain distribution, such as arising in non-circular section.

The proposed material model uses the yield surface function proposed by Lee & Fenves (1998), which consists of two hardening parameters. Only one of the hardening parameter, which governs the concrete compressive mechanical behaviour, is defined. The identification of another hardening parameter is necessary for the numerical simulation, when concrete is subjected to tensile stress. Since Mac^{2T} could apply compressive stress only, split tests on the rubberised concrete cylinder are needed to investigate rubberised concrete tensile behaviour.

Reference

- ASTM, C., 2002. 469, Standard test method for static modulus of elasticity and Poisson's ratio of concrete in compression. Annual book of ASTM standards, 4.
- ASTM, C., 2005. 33, Standard specification for concrete aggregates. *Annual Book of ASTM Standards*, West Conshohocken, USA
- Becque, J., Patnaik, A.K. and Rizkalla, S.H., 2003. Analytical models for concrete confined with FRP tubes. *Journal of Composites for Construction*, 7(1), pp.31-38.
- Bertacchi, P. and Bellotti, R., 1973. Experimental research on deformation and failure of concrete under triaxial loads. In *The deformation and the rupture of solids subjected to multiaxial stresses*.
- Berthet, J.F., Ferrier, E. and Hamelin, P., 2005. Compressive behavior of concrete externally confined by composite jackets. Part A: experimental study. *Construction and Building Materials*, 19(3), pp.223-232.
- Binici, B., 2005. An analytical model for stress–strain behavior of confined concrete. *Engineering structures*, 27(7), pp.1040-1051.
- Bompa, D.V., Elghazouli, A.Y., Xu, B., Stafford, P.J. and Ruiz-Teran, A.M., 2017. Experimental assessment and constitutive modelling of rubberised concrete materials. *Construction and Building Materials*, 137, pp.246-260.
- Burke Jr, M.P., 2009. *Integral and semi-integral bridges*. John Wiley & Sons.
- Chen, W.F., Yamaguchi, E., Kotsovos, M.D. and Pan, A.D., 1993, February. Constitutive models. In *Finite Element Analysis of Reinforced Concrete Structures II* (pp. 36-117). ASCE.
- Chen, W.F., 1994. *Constitutive equations for engineering materials, Vol. 2: Plasticity and modeling*, Amsterdam: Elsevier.
- Doran, B., Koksai, H.O. and Turgay, T., 2009. Nonlinear finite element modeling of rectangular/square concrete columns confined with FRP. *Materials & Design*, 30(8), pp.3066-3075.

Garcia, R., Hajirasouliha, I. and Pilakoutas, K., 2010. Seismic behaviour of deficient RC frames strengthened with CFRP composites. *Engineering Structures*, 32(10), pp.3075-3085.

Garcia, R., 2014. *Pilot Study on Confined Rubberised Concrete and its constitutive relationships*. Internal Report No. D1.3, Anagennisi Project, Dept. of Civil and Structural Engineering, The University of Sheffield, UK.

Gerstle, K.H., Linse, D.L. and Bertacchi, P., 1978. Strength of concrete under multiaxial stress states. *Special Publication*, 55, pp.103-132.

Gerstle, K.B., Zimmerman, R.M., Winkler, H., Traina, L.A., Taylor, M.A., Schickert, G., Rossi, P., Newman, J.B., Linse, D., Ko, H.Y. and Kotsovos, M.D., 1980, Behavior of Concrete under Multiaxial Stress States. *Journal of the Engineering Mechanics Division*, 106(6), pp.1383-1403.

Gerstle, K.H., 1981, September. Simple formulation of triaxial concrete behavior. In *Journal Proceedings* (Vol. 78, No. 5, pp. 382-387).

Han, D.J. and Chen, W.F., 1985. A nonuniform hardening plasticity model for concrete materials. *Mechanics of materials*, 4(3-4), pp.283-302.

Hinton, E., Wood, R.D., Bićanić, N., White, P.S. and Hellen, T.K., 2010. *Introduction to nonlinear finite element analysis*. Nafems.

Imran, I. and Pantazopoulou, S.J., 1996. Experimental study of plain concrete under triaxial stress. *ACI Materials Journal-American Concrete Institute*, 93(6), pp.589-601.

Jiang, T. and Teng, J.G., 2007. Analysis-oriented stress–strain models for FRP–confined concrete. *Engineering Structures*, 29(11), pp.2968-2986.

Jiang, J.F. and Wu, Y.F., 2012. Identification of material parameters for Drucker–Prager plasticity model for FRP confined circular concrete columns. *International Journal of Solids and Structures*, 49(3-4), pp.445-456.

Karsan, I.D. and Jirsa, J.O., 1969. Behavior of concrete under compressive loadings. *Journal of the Structural Division*.

- Khatib, Z.K. and Bayomy, F.M., 1999. Rubberized Portland cement concrete. *Journal of materials in civil engineering*, 11(3), pp.206-213.
- Ko, H.Y. and Sture, S., 1974. Three-dimensional mechanical characterization of anisotropic composites. *Journal of Composite Materials*, 8(2), pp.178-190.
- Kotsovos, M.D. and Newman, J.B., 1977, September. Behavior of concrete under multiaxial stress. In *Journal Proceedings* (Vol. 74, No. 9, pp. 443-446).
- Kupfer, H., Hilsdorf, H.K. & Rusch, H., 1969. Behavior of Concrete Under Biaxial Stresses. *ACI Journal Proceedings*, 66(8), pp.656–666.
- Lee, J. and Fenves, G.L., 1998. Plastic-damage model for cyclic loading of concrete structures. *Journal of engineering mechanics*, 124(8), pp.892-900.
- Lee, J. and Fenves, G.L., 2001. A return-mapping algorithm for plastic-damage models: 3-D and plane stress formulation. *International Journal for Numerical Methods in Engineering*, 50(2), pp.487-506.
- Li, G., 2006. Experimental study of FRP confined concrete cylinders. *Engineering structures*, 28(7), pp.1001-1008.
- Linse, D. and Aschl, H., 1976. Tests on the behavior of concrete under multiaxial stresses. *Technical university of munich, department of reinforced concrete report*.
- Lublinter, J., Oliver, J., Oller, S. and Onate, E., 1989. A plastic-damage model for concrete. *International Journal of solids and structures*, 25(3), pp.299-326.
- Mirmiran, A. and Shahawy, M., 1997. Behavior of concrete columns confined by fiber composites. *Journal of structural engineering*, 123(5), pp.583-590.
- Ohtani, Y.C. and Chen, W.F., 1987. Hypoelastic-perfectly plastic model for concrete materials. *Journal of engineering mechanics*, 113(12), pp.1840-1860.
- Oikonomou, N. and Mavridou, S., 2009. Improvement of chloride ion penetration resistance in cement mortars modified with rubber from worn automobile tires. *Cement and Concrete Composites*, 31(6), pp.403-407.

Pantazopoulou, S.J. and Mills, R.H., 1995. Microstructural aspects of the mechanical response of plain concrete. *Materials Journal*, 92(6), pp.605-616.

Papastergiou, Panagiotis. *A confinement model for concrete wrapped of pretensioned with frp*. PhD Thesis. The University of Sheffield, 2010.

Parvin, A. and Wang, W., 2001. Behavior of FRP jacketed concrete columns under eccentric loading. *Journal of Composites for construction*, 5(3), pp.146-152.

Petkovski, M., Crouch, R.S. and Waldron, P., 2006. Apparatus for testing concrete under multiaxial compression at elevated temperature (mac 2T). *Experimental mechanics*, 46(3), pp.387-398.

Presti, D.L., 2013. Recycled tyre rubber modified bitumens for road asphalt mixtures: A literature review. *Construction and Building Materials*, 49, pp.863-881.

Raffoul, S., 2014. *Pilot study on rubberised concrete*. Internal Report No. D1.1, Anagennisi Project, Dept. of Civil and Structural Engineering, The University of Sheffield, UK.

Raffoul, S., Garcia, R., Pilakoutas, K., Guadagnini, M. and Medina, N.F., 2016. Optimisation of rubberised concrete with high rubber content: an experimental investigation. *Construction and Building Materials*, 124, pp.391-404.

Raffoul, S., Garcia, R., Escolano-Margarit, D., Guadagnini, M., Hajirasouliha, I. and Pilakoutas, K., 2017. Behaviour of unconfined and FRP-confined rubberised concrete in axial compression. *Construction and Building Materials*, 147, pp.388-397.

Reda Taha, M.M., El-Dieb, A.S., Abd El-Wahab, M.A. and Abdel-Hameed, M.E., 2008. Mechanical, fracture, and microstructural investigations of rubber concrete. *Journal of materials in civil engineering*, 20(10), pp.640-649.

Rochette, P. and Labossiere, P., 1996, August. A plasticity approach for concrete columns confined with composite materials. In *Second International Conference on Advanced Composite Materials in Bridges and Structures, Montreal*.

Rousakis, T. and Tepfers, R., 2001. Experimental investigation of concrete cylinders confined by carbon FRP sheets, under monotonic and cyclic axial compressive load. *Research Rep*, 1(2).

Schickert, G. and Winkler, H., 1977. Results of test concerning strength and strain of concrete subjected to multi-axial compressive stress.

Shahawy, M., Mirmiran, A. and Beitelman, T., 2000. Tests and modeling of carbon-wrapped concrete columns. *Composites Part B: Engineering*, 31(6-7), pp.471-480.

Simo, J.C. and Hughes, T.J., 2006. *Computational inelasticity* (Vol. 7). Springer Science & Business Media.

Spoelstra, M.R. and Monti, G., 1999. FRP-confined concrete model. *Journal of composites for construction*, 3(3), pp.143-150.

Systemes, D., 2014. Abaqus Theory Guide. *Dassault Systemes Simulia Corp. Providence, RI, USA*.

Teng, J.G. and Lam, L., 2004. Behavior and modeling of fiber reinforced polymer-confined concrete. *Journal of structural engineering*, 130(11), pp.1713-1723.

Toutanji, H.A., 1996. The use of rubber tire particles in concrete to replace mineral aggregates. *Cement and Concrete Composites*, 18(2), pp.135-139.

Wong, H.H. and Kwan, A.K., 2008. Packing density of cementitious materials: part 1—measurement using a wet packing method. *Materials and structures*, 41(4), pp.689-701.

Van Mier, J.G.M., 1984. *Strain-softening of concrete under multiaxial loading conditions* (pp. 32-39). Technische Hogeschool Eindhoven.

Youssif, O., ElGawady, M.A., Mills, J.E. and Ma, X., 2014. Finite element modelling and dilation of FRP-confined concrete columns. *Engineering Structures*, 79, pp.70-85.

Yu, T., Teng, J.G., Wong, Y.L. and Dong, S.L., 2010. Finite element modeling of confined concrete-II: Plastic-damage model. *Engineering structures*, 32(3), pp.680-691.

Zhao, J.J. and Tonia, D.E., 2012. Bridge engineering: design, rehabilitation, and maintenance of modern highway bridges.